Peter Petrik

Characterization of polysilicon thin films using *in situ* and *ex situ* spectroscopic ellipsometry

DISSERTATION
for the degree of
Doctor of Philosophy
in
Physics

Department of Experimental Physics of the
Technical University of Budapest
&
Research Institute for Technical Physics
and Materials Science of the
Hungarian Academy of Sciences

Budapest, 1999

Acknowledgments

This thesis could not exist without the help of many colleagues at the Research Institute for Technical Physics and Materials Science (MTA-MFA), at the Chair of Electron Devices of the Friedrich-Alexander University Erlangen-Nuremberg (LEB) and at the Fraunhofer Institute for Integrated Circuits (FhG-IIS-B) in Erlangen, Germany. Most of the sample preparations and measurements were made at the LEB and FhG-IIS-B. Financial support of the Soros Foundation and the DAAD (Deutscher Akademischer Austauschdienst) is gratefully appreciated.

I thank

- Prof. József Gyulai, my advisor, for orienting me to a fruitful cooperation with colleagues in Erlangen, and for his constant support during my work,
- Prof. Dr.-Ing. H. Ryssel for the opportunity to contribute to developments and to perform measurements and sample preparations at the LEB and FhG-IIS-B,
- Dr. Tivadar Lohner and Dr. Miklós Fried for good ideas, advices, discussions, and continuous support,
- Dr. Claus Schneider, Wolfgang Lehnert, Dr. Rudolf Berger for the lot of help and support during my stays in Erlangen,
- Dr. László Péter Biró and Dr. Nguyen Quoc Khánh for fruitful discussions and their contribution to the measurements,
- Olivér Polgár for the software for ellipsometric data evaluation, Annette Daurer for TEM measurements, and the numerous colleagues at the MTA-MFA, LEB, and FhG-IIS-B for their support.

Special thanks to Dr. Teréz Kormány, who helped me to join a wonderful research group, and Dr. János Müller, my teacher at secondary school, who gave me the basic knowledge and the first kick to the direction of natural sciences.

I thank my family, especially my wife Éva, who had to miss me during my lengthy absences, for the constant support.

Preface

Spectroscopic ellipsometry (SE) and polysilicon: a key measurement technique and a key material in today's microelectronics. Ellipsometry is an optical method, which measures the complex reflectance ratio of the sample. The words "optical" and "complex" are very important. "Optical" means that it is non-destructive and capable of *in situ* measurements. "Complex" means that not only intensity differences are obtained, as in case of spectrophotometers, but also phase information, allowing sub-monolayer precision. The trend toward smaller device dimensions in the semiconductor industry increased the importance of *in situ* capability and sub-monolayer precision. Taking CMOS technology as an example, the feature size is currently 250 nm with a gate oxide thickness of 4-5 nm. Feature size and gate oxide thickness are expected to shrink to 70 nm and 1.5 nm, respectively, in 2009 [Cof98]. The recently emerging concept of "single wafer processing", as well as new techniques to provide optical access to processed wafers will increase the importance of the *in situ* measurement including SE and other optical methods. The extended analytic capabilities of spectroscopic instruments lead them to be applied to increasingly complex samples like multilayer coatings, ion implanted materials or other microscopically inhomogeneous materials. Some material and structural properties, which can be measured by SE involve the determination of refractive index (n and k from one measurement), layer thickness (also multilayer stacks), interface quality, microstructure, contamination, surface properties, or profiles in layers with continously varying refractive index. Using photodiode array detectors a data acquisition time of 12 ms per measurement can be achieved, which makes SE especially attractive for real time applications. Although the principles of ellipsometry date back to the late 19th century, based on Drude's investigations [Dru89a, Dru89b, Dru90], this technique was not used until the beginning of 1960s. The reason is that an ellipsometric measurement entails the solution of complicated complex non-linear equations which can be solved analytically only in special cases and require numerical approaches in most instances. The computers of rapidly increasing performance and decreasing prices were the sufficient tools for the data processing.

Understanding and utilizing the advantages of polysilicon was one of the most important fundamental developments in the history of integrated circuits. Polysilicon is widely used because it forms an adherent oxide, adsorbs and re-emits dopants, has good step coverage if deposited by chemical vapor deposition (CVD), matches the mechanical properties of Si single-crystal, has a high melting point, has a compatible work function for MOS devices, absorbs heavy metals (gettering), forms high conductivity silicides, and is compatible with HF. Its compatibility with IC processing and its good step coverage provided by CVD offers many advantages in bipolar, MOS, and BiCMOS circuits, because it provides low MOS threshold voltage, fills trenches, permits SAliciding, provides long gate oxide wearout times, provides a wide range of resistivities, permits oxide reflow process temperatures, simplifies processing, can be selectively deposited, permits shallow, high quality junctions, and forms silicide thin film resistors. Polysilicon will have applications in semiconductor devices far into the future because it plays major role in the fabrication of all manner of devices.

In the present work *ex situ* and *in situ* measurement of polysilicon thin films was performed using spectroscopic ellipsometry. I could take advantage of the high amount of information contained in the measured spectra which has been used for a wide range of investigations targeting polycrystalline silicon.

First, optical models were developed in order to provide a good description of the multi-layer structures used in the study. As the properties of polysilicon depend strongly on the preparation conditions, there is no way of using a single reference dielectric function data for the polysilicon layers. Therefore, the polysilicon structure was modeled as a mixture of different phases like single-crystalline silicon, amorphous silicon and voids utilizing the advantages of the Bruggeman effective-medium approximation used widely for polysilicon in the literature. I have shown that using these three components does not provide a good description for all deposition conditions. Using also fine-grained polycrystalline silicon as reference data in the effective medium model results in a better fit of the experimental data and provides an insight of the structural change as a function of deposition temperature or layer thickness.

Using effective medium models surface roughness can be measured quantitatively. Comparison with results from independent measurement techniques like atomic force microscopy or transmission electron microscopy justifies the reliability of the optical models and the precision of the optical method. An important output of the investigations was that in spite of the good agreement between ellipsometry and atomic force microscopy, care must be taken on the interpretation of the measurement results (explanations in the literature are rather confusing in many cases).

This method can be used even in the very complex cases of ion-implanted single- and polycrystalline silicon. In this case the multilayer models are extended to take into account the damage depth profile as a compositional change in the effective medium model. The reliability of the method has been proven by cross-checking measurements with Rutherford backscattering spectrometry and transmission electron microscopy.

Application of the optical models were demonstrated by *in situ* measurement in a vertical furnace during annealing of amorphous silicon. At the Fraunhofer Institute for Integrated Circuits in Erlangen, a spectroscopic ellipsometer was integrated in a vertical furnace using a novel beam guiding system. I had the opportunity to take part of the development by realizing a method of the correction for the phase shift of the beam-guiding prisms, and performing measurements in the vertical furnace in order to determine the high temperature reference data and – using these results together with the optical models developed during the *ex situ* investigations – to monitor the crystallization of amorphous silicon during annealing. We showed that in spite of the rather long beam path and the complicated beam-guiding system the equipment is capable for *in situ* monitoring of high temperature processes inside a vertical furnace. The novel method for the integration allows a cheap and fast integration into industrial equipment with minor modification of the chamber itself.

Contents

Chapter 1

Theory

1.1 Basics of ellipsometry

1.1.1 Physics

Ellipsometry measures the change on the state of polarization caused by the reflection on the sample. If polarized light will be reflected on the boundary of two media (see Fig. 1.1), the state of polarization of the reflected beam will be elliptic, circular, or linear depending on the properties of the sample.

The state of polarization can be described by dividing the light beam into two components that are parallel ($\overline{E}_p$) and perpendicular ($\overline{E}_s$) to the plane of incidence (the over-line denotes complex values). Both components are plane waves described by [Bor68]

$$\overline{E} = \overline{E}_0 e^{i(\omega t+\delta)} e^{-i\omega \frac{\overline{n}}{c} r}, \tag{1.1}$$

where ω is the frequency, δ is the phase, $\overline{n} = n - ik$ is the complex refractive index, and c is the speed of the light in vacuum. The state of polarization of a plane wave is defined by

$$\overline{\chi} = \frac{\overline{E}_p}{\overline{E}_s}. \tag{1.2}$$

where p and s denote the components parallel and perpendicular to the plane of incidence respectively, and χ is called the polarization coefficient. An ellipsometric measurement provides the ratio of the polarization coefficients of the reflected ($\overline{\chi}_r$) and incident ($\overline{\chi}_i$) light:

$$\overline{\rho} = \frac{\overline{\chi}_r}{\overline{\chi}_i}. \tag{1.3}$$

In the late 19th century Drude [Dru89a, Dru89b] introduced the following terminology:

$$\overline{\rho} = \frac{\overline{\chi}_r}{\overline{\chi}_i} = \frac{|\overline{\chi}_r|}{|\overline{\chi}_i|} e^{i(\delta_r - \delta_i)} = \tan \Psi e^{i\Delta}. \tag{1.4}$$

The ratio of the polarization coefficients is equivalent with the ratio of the Fresnel-reflection coefficients $\overline{r}_p$ and $\overline{r}_s$:

$$\frac{\overline{\chi}_r}{\overline{\chi}_i} = \frac{\dfrac{\overline{E}_{r,p}}{\overline{E}_{r,s}}}{\dfrac{\overline{E}_{i,p}}{\overline{E}_{i,s}}} = \frac{\dfrac{\overline{E}_{r,p}}{\overline{E}_{i,p}}}{\dfrac{\overline{E}_{r,s}}{\overline{E}_{i,s}}} = \frac{\overline{r}_p}{\overline{r}_s}, \tag{1.5}$$

consequently, $\overline{\rho}$ is called the complex reflectance ratio.

TanΨ and Δ can be written as

$$\tan\Psi = \frac{|\overline{\chi}_r|}{|\overline{\chi}_i|} = \frac{|\overline{r}_p|}{|\overline{r}_s|}, \tag{1.6}$$

and

$$\Delta = \delta_r - \delta_i = (\delta_{r,p} - \delta_{r,s}) - (\delta_{i,p} - \delta_{i,s}) = (\delta_{r,p} - \delta_{i,p}) - (\delta_{r,s} - \delta_{i,s}) = \Delta_p - \Delta_s, \tag{1.7}$$

where δ denotes the phase of the components (i: incident, r: reflected, p: parallel, s: perpendicular). TanΨ is the ratio of the absolute values of the reflected and incident polarization components, or equivalently, the ratio of the absolute values of the p and s components of the Fresnel-reflection coefficients. The values Ψ and Δ are called the ellipsometric angles.

Using the photometric method, cosΔ is directly obtained from the line shape analysis (see Section 1.1.4, page 14). For spectroscopic ellipsometry, the convention of plotting the tanΨ and cosΔ values is used, rather than plotting the Ψ and Δ values as in the case of single wavelength ellipsometry. The reason is, that most of the spectroscopic ellipsometers use the photometric method.

1.1.2 Optical model

The determination of the physical parameters (layer thickness, refractive index, microstructure, etc.) of the sample from the measured values (tanΨ–cosΔ or Ψ–Δ) depends on three factors [Asp82]:

- accurate spectroscopic data for the sample and its possible constituents,
- an appropriate model for the complex reflectances $\overline{r}_p$ and $\overline{r}_s$ expressed in terms of the sample microstructure,
- the systematic, objective determination of the values and confidence limits of the wavelength-independent parameters of the model with linear regression analysis.

Surprisingly, the first requirement is not trivial. Not because of instrumentation limitations, but because optical measurements, particularly ellipsometric measurements, are extremely sensitive to surface conditions. To lowest order everyone takes accurate data, but the extent to which these data accurately represent the intrinsic properties of a sample depends on how well the model assumptions are realized in practice. For example, the accuracy of dielectric function data for a homogeneous material with a nominally bare surface depends on how completely unwanted over-layer material can be removed.

The second requirement demands some physical insight into the possible structure of the sample, i. e. whether intrinsic over-layers such as density-deficient outer regions

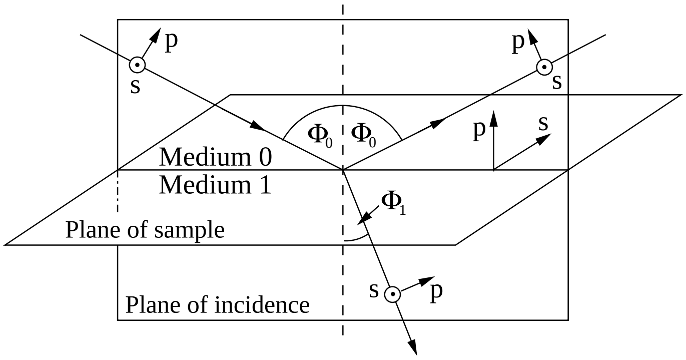

Figure 1.1. Reflexion of polarized light

are likely to be present, whether the heterogeneity is macroscopically isotropic, etc. If a microstructurally heterogeneous material consists of regions large enough to possess their own dielectric identity, the samples can be described in terms of multilayer models and effective-medium theory (see Section 1.1.3). These models allow the response of the sample to be described by a few wavelength-independent parameters such as compositions, thicknesses, or densities, which contain the microstructural information about the sample. These are analogous to the frequency-independent lumped-circuit resistance, capacitance, and inductance parameters of circuit theory.

The third requirement deals with the determination of these parameters by linear regression analysis (LRA). While the principal purpose of LRA is to provide least-squares values, an equally important function is to provide confidence limits on the values themselves. The confidence limits not only give some insight as to how well a particular model fits the data, but they also provide information as to whether the data are really determining parameter values, or whether too many parameters have been used. Too many parameters, or correlated parameters, result in drastic increase in the confidence limits. They thereby provide a natural check against the tendency to add parameters indiscriminately simply for the sake of reducing the mean-square deviation.

Most optical models use flat semi-infinite substrates with one or more laminar adherent layers of uniform thickness on the surface. The mathematical description of the interaction between light and material is given by Maxwell's equations. Based on these equations, the Fresnel-reflection coefficients can be calculated. The simplest case is the reflection and transmission at the planar interface between two isotropic media (see Fig. 1.1).

In this case, the Fresnel-reflection coefficients can be written as [Azz87]

$$\frac{\overline{E}_{r,p}}{\overline{E}_{i,p}} = \overline{r}_p = \frac{\overline{n}_1 \cos\Phi_0 - \overline{n}_0 \cos\Phi_1}{\overline{n}_1 \cos\Phi_0 + \overline{n}_0 \cos\Phi_1}, \tag{1.8}$$

$$\frac{\overline{E}_{r,s}}{\overline{E}_{i,s}} = \overline{r}_s = \frac{\overline{n}_0 \cos\Phi_0 - \overline{n}_1 \cos\Phi_1}{\overline{n}_0 \cos\Phi_0 + \overline{n}_1 \cos\Phi_1}, \tag{1.9}$$

where $\overline{n}_0$ is the refractive index of Medium 0 (see Fig. 1.1), $\overline{n}_1$ is the refractive index of Medium 1, Φ_0 is the angle of incidence, and Φ_1 is the angle of refraction. Φ_1 can be obtained using

$$\overline{n}_0 \sin\Phi_0 = \overline{n}_1 \sin\Phi_1, \tag{1.10}$$

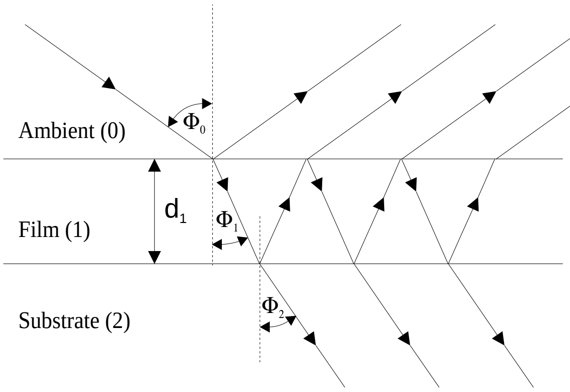

Figure 1.2. Multiple reflexion in a three-phase system

which is Snell's law.

Thus $\overline{\rho}$ can be expressed by the refractive indices and the angle of incidence:

$$\overline{\rho} = \frac{\overline{r}_p}{\overline{r}_s} = \overline{\rho}(\overline{n}_0, \overline{n}_1, \Phi_0). \tag{1.11}$$

$\overline{n}_1$ can be calculated, because Φ_0 and $\overline{n}_0$ are known ($\overline{n}_0 = 1$ if Medium 0 is air).

A case of considerable importance in ellipsometry is that in which polarized light is reflected from, or transmitted by a substrate covered by a single film (see Fig. 1.2).

A plane wave incident in Medium 0 (at an angle Φ_0) will give rise to a resultant reflected wave in the same medium and to a resultant transmitted wave (at the angle Φ_2) in Medium 2 (the substrate). Our objective is to relate the complex amplitudes of the resultant reflected and transmitted waves to the amplitude of the incident wave, when the latter is linearly polarized parallel (p) and perpendicular (s) to the plane of incidence. Addition of the partial waves leads to an infinite geometric series for the total reflected amplitude R

$$\overline{R}^j = \frac{\overline{r}_{01}^j + \overline{r}_{12}^j e^{-i\beta}}{1 + \overline{r}_{01}^j \overline{r}_{12}^j e^{-i\beta}}, \; j = p, s, \tag{1.12}$$

where $\overline{r}_{01}$ and $\overline{r}_{12}$ are the reflection coefficients at the $0|1$ ($1|0$) and $1|2$ interfaces. In terms of the free-space wavelength λ, the film thickness d_1, the film complex index of refraction n_1 and the angle of refraction in the film Φ_1, the phase angle β (film phase thickness, i. e. the phase change that the multiply-reflected wave inside the film experiences as it traverses the film once from one boundary to the other) is given by

$$\beta = 2\pi(\frac{d_1}{\lambda})\overline{n}_1 \cos\Phi_1, \tag{1.13}$$

or

$$\beta = 2\pi(\frac{d_1}{\lambda})\overline{n}_1 \sqrt{\overline{n}_1^2 - \overline{n}_0^2 \sin\Phi_0}, \tag{1.14}$$

if Snell's law (eqn. 1.10) is applied, where Φ_0 is the angle of incidence in Medium 0.

The method of addition of multiple reflections becomes impractical when considering the reflection and transmission of polarized light at oblique incidence by a multilayer film between semi-infinite ambient and substrate media. A more elegant

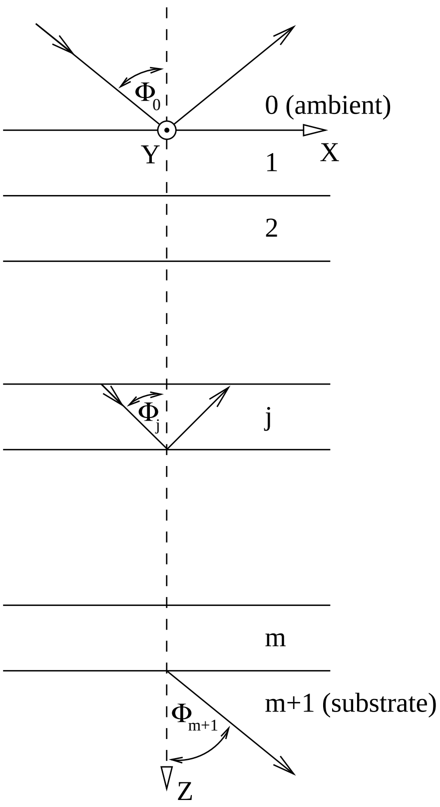

Figure 1.3. Reflection and transmission of a plane wave by a multi-film structure (films 1, 2, $\cdots$, m) sandwiched between semi-infinite ambient (0) and substrate (m+1) media. Φ_0 is the angle of incidence, Φ_j and Φ_{m+1} are the angles of refraction in the jth film and substrate, respectively.

approach is to employ 2 × 2 matrices [Azz87]. This method is based on the fact that the equations that govern the propagation of light are linear and that the continuity of the tangential fields across an interface between two isotropic media can be regarded as a 2 × 2 – linear-matrix transformation.

Consider a stratified structure that consists of a stack of $1, 2, 3, \cdots, j, \cdots, m$ parallel layers sandwiched between semi-infinite ambient (0) and substrate (m+1) media (Fig. 1.3). Let all media be linear homogeneous and isotropic, and let the complex index of refraction of the jth layer be $\overline{n}_j$ and its thickness d_j. $\overline{n}_0$ and $\overline{n}_{m+1}$ represents the complex indices of refraction of the ambient and substrate media, respectively. An incident monochromatic plane wave in Medium 0 (the ambient) generates a resultant reflected plane wave in the same medium and a resultant transmitted plane wave in medium m+1 (the substrate). The total field inside the jth layer consists of a forward- and a backward-traveling plane wave denoted by "+" and "−", respectively.

Let $\overline{E}^+(z)$ and $\overline{E}^-(z)$ denote the complex amplitudes of the forward- and backward-traveling plane waves at an arbitrary plane z. The total field at z can be described by a 2 × 1 column vector

$$\overline{E}(z) = \begin{bmatrix} \overline{E}^+(z) \\ \overline{E}^-(z) \end{bmatrix}. \tag{1.15}$$

If we consider the fields at two different planes z' and z'' parallel to the layer boundaries then, by virtue of system linearity, $\overline{E}(z'')$ and $\overline{E}(z')$ must be related by a

2×2-matrix transformation

$$\begin{bmatrix} \overline{E}^{+}(z') \\ \overline{E}^{-}(z') \end{bmatrix} = \begin{bmatrix} \overline{S}_{11} & \overline{S}_{12} \\ \overline{S}_{21} & \overline{S}_{22} \end{bmatrix} \begin{bmatrix} \overline{E}^{+}(z'') \\ \overline{E}^{-}(z'') \end{bmatrix}, \tag{1.16}$$

or more concisely,

$$\overline{E}(z') = \overline{S}\; \overline{E}(z''), \tag{1.17}$$

where

$$\overline{S} = \begin{bmatrix} \overline{S}_{11} & \overline{S}_{12} \\ \overline{S}_{21} & \overline{S}_{22} \end{bmatrix}. \tag{1.18}$$

By choosing z' and z'' to lie immediately on opposite sides of the $(j-1)|j$ interface, located at z_j between layers $j-1$ and j, equation 1.17 becomes

$$\overline{E}(z_j - 0) = \overline{I}_{(j-1)j}\overline{E}(z_j + 0), \tag{1.19}$$

where $\overline{I}_{(j-1)j}$ is a 2×2 matrix characteristic of the $(j-1)|j$ interface alone. On the other hand, if z' and z'' are chosen inside the jth layer at its boundaries, eqn. 1.17 becomes

$$\overline{E}(z_j + 0) = \overline{L}_j\overline{E}(z_j + d_j - 0), \tag{1.20}$$

where $\overline{L}_j$ is a 2×2 matrix characteristic of the jth layer alone whose thickness is d_j. Only the reflected wave in the ambient medium and the transmitted wave in the substrate are accessible for measurement, so that it is necessary to relate their fields to those of the incident wave. By taking the planes z' and z'' to lie in the ambient and substrate media, immediately adjacent to the $0|1$ and $m|(m+1)$ interfaces respectively, eqn. 1.17 will read

$$\overline{E}(z_1 - 0) = \overline{S}\; \overline{E}(z_{m+1} + 0). \tag{1.21}$$

Equation 1.21 defines a scattering matrix $\overline{S}$ which represents the overall reflection and transmission properties of the stratified structure. $\overline{S}$ can be expressed as a product of the interface and layer matrices $\overline{I}$ and $\overline{L}$ that describe the effects of the individual interfaces and layers of the entire stratified structure, taken in proper order, as follows:

$$\overline{S} = \overline{I}_{01}\overline{L}_1\overline{I}_{12}\overline{L}_2 \cdots \overline{I}_{(j-1)j}\overline{L}_j \cdots \overline{L}_m\overline{I}_{m(m+1)}. \tag{1.22}$$

Equation 1.22 may be proved readily by repeated application of eqn. 1.17 to the successive interfaces and layers of the stratified structure, starting with the ambient-first film $(0|1)$ interface and ending by the last film-substrate interface $[m|(m+0)]$.

As an example, consider the case of a single film (1) sandwiched between semi-infinite ambient (0) and substrate (2) media (Fig. 1.2). From eqn. 1.22 the scattering matrix $\overline{S}$ in this case is given by

$$\overline{S} = \overline{I}_{01}\overline{L}_1\overline{I}_{12}, \tag{1.23}$$

which upon substitution of $\overline{I}_{01}$, $\overline{L}_1$ and $\overline{I}_{12}$ [Azz87] becomes

$$\overline{S} = (\frac{1}{t_{01}t_{12}}) \begin{bmatrix} 1 & r_{01} \\ r_{01} & 1 \end{bmatrix} \begin{bmatrix} e^{j\beta} & 0 \\ 0 & e^{-j\beta} \end{bmatrix} \begin{bmatrix} 1 & r_{12} \\ r_{12} & 1 \end{bmatrix}. \tag{1.24}$$

In case of a two film system, eqs. 1.23 and 1.24 only have to be extended as

$$\overline{S} = \overline{I}_{01}\overline{L}_1\overline{I}_{12}\overline{L}_2\overline{I}_{23}, \tag{1.25}$$

and

$$\overline{S} = (\frac{1}{t_{01}t_{12}})\begin{bmatrix} 1 & r_{01} \\ r_{01} & 1 \end{bmatrix}\begin{bmatrix} e^{j\beta_1} & 0 \\ 0 & e^{-j\beta_1} \end{bmatrix}\begin{bmatrix} 1 & r_{12} \\ r_{12} & 1 \end{bmatrix}\begin{bmatrix} e^{j\beta_2} & 0 \\ 0 & e^{-j\beta_2} \end{bmatrix}\begin{bmatrix} 1 & r_{23} \\ r_{23} & 1 \end{bmatrix}. \tag{1.26}$$

If we consider the overall system as a two-phase (ambient-substrate) structure, then eqn. 1.16 can be rewritten as

$$\begin{bmatrix} \overline{E}_a^+ \\ \overline{E}_a^- \end{bmatrix} = \begin{bmatrix} \overline{S}_{11} & \overline{S}_{12} \\ \overline{S}_{21} & \overline{S}_{22} \end{bmatrix}\begin{bmatrix} \overline{E}_s^+ \\ 0 \end{bmatrix}, \tag{1.27}$$

where the subscripts a and s refer to the ambient and substrate media, respectively, and $\overline{E}_s^- = 0$. Further expansion of eqn. 1.27 yields the overall reflection and transmission coefficients of the stratified structures as

$$\overline{R} = \frac{\overline{E}_a^-}{\overline{E}_a^+} = \frac{\overline{S}_{21}}{\overline{S}_{11}}, \tag{1.28}$$

$$\overline{T} = \frac{\overline{E}_s^+}{\overline{E}_a^+} = \frac{1}{\overline{S}_{11}}, \tag{1.29}$$

respectively. From eqs. 1.28 and 1.29 it is clear that only elements of the first column of scattering matrix $\overline{S}$ determine the overall reflection and transmission coefficients.

Then $\overline{\rho}$ can be expressed by the overall (effective) reflection coefficients ($\overline{R}_p$ and $\overline{R}_s$):

$$\overline{\rho} = \frac{\overline{R}_p}{\overline{R}_s}. \tag{1.30}$$

The number of the parameters is much higher than for a two phase system:

$$\overline{\rho} = \overline{\rho}(\overline{n}_0, \overline{n}_1, \cdots, \overline{n}_m, d_1, d_2, \cdots, d_k, \Phi_0, \lambda). \tag{1.31}$$

To determine the unknown parameters one has to increase the amount of independent information. There are several possibilities, e. g. multiple angles of incidence, different ambients, and different layer thickness of the same material. The most important is the multi-wavelength approach (spectroscopic ellipsometry or SE).

The complex non-linear function standing on the right-hand side of eqn. 1.31 can be inverted only in special cases. A general solution is provided by using the LRA technique to minimize the differences between the calculated and experimental data by adjusting the model parameters, and finally to obtain the results in terms of best-fit model parameters and their 95% confidence limits as well as the unbiased estimator σ of the mean square deviation,

$$\sigma = \sqrt{\frac{1}{(N-P-1)}\sum_{j=1}^{n}\{(\cos\Delta_j^{meas} - \cos\Delta_j^{calc})^2 + (\tan\Psi_j^{meas} - \tan\Psi_j^{calc})^2\}}, \tag{1.32}$$

where N is the number of independent readings corresponding to the different wavelengths at which SE measurements are made, P is the number of unknown model parameters, and $\tan\Psi$ and $\cos\Delta$ are the measured ("*meas*") or calculated ("*calc*") ellipsometric values.

1.1.3 Effective medium theory

The objective of effective medium theory is to determine the dielectric function of macroscopically homogeneous and microscopically heterogeneous or composite materials. Examples of composite materials include metal films, which can be described as a heterogeneous mixture of materials and voids owing to the inability of forming grain boundaries in closely packed systems without some loss of material. Other examples include polycrystalline films, amorphous materials and glasses. A microscopically rough surface can also be considered as a heterogeneous medium, being a mixture of bulk and ambient on a microscopic scale. The material can be considered as macroscopically homogeneous, if the dimensions of the phases are smaller than the wavelength of the measuring light.

The dielectric function of a heterogeneous material and the limits to the amount of microstructural information that can be drawn from it are easily understood if we recall that electrodynamics deals with macroscopic observables that are basically averages of their microscopic counterparts. Therefore, the solution involves two distinct steps: first, the electrostatic problem is solved exactly for a given microstructure to obtain the local electric field $\vec{e}(\vec{r})$ and dipole moment $\vec{p}(\vec{r})$ per unit volume at every point in space; secondly, these microscopic solutions are averaged to obtain their macroscopic counterparts $\vec{E}$ and $\vec{P}$ [Asp82]. The dielectric function $\overline{\epsilon}$ of a material is defined as

$$\vec{D} = \overline{\epsilon}\vec{E} = \vec{E} + 4\pi\vec{P}, \tag{1.33}$$

where $\vec{D}$, $\vec{E}$, and $\vec{P}$ are the macroscopic (average or observable) displacement field, electric field, and dipole moment per unit volume, respectively.

To calculate the local electric field, a simple approach is the exactly solvable configuration where a simple cubic lattice of points with lattice constants a and polarizability α (the Clausius-Mosotti model) is considered. This is the prototypical inhomogeneous material, being a mixture of polarizable points and empty space. If a uniform field $\vec{E}_i$ is applied, the points polarize as $\vec{p} = \alpha\vec{E}_{loc}$, where $\vec{E}_{loc} = \vec{e}(\vec{R}_n)$ is the local field at a lattice site $\vec{R}_n$. The microscopic field $\vec{e}(\vec{r})$ is the superposition of $\vec{E}_i$ and the dipole fields from $\vec{p}$ and can be written

$$\vec{e}(\vec{r}) = \vec{E}_i + \sum_{R_n} \vec{E}_{dip}(\vec{r} - \vec{R}_n), \tag{1.34}$$

where

$$\vec{E}_{dip}(\vec{r}) = \frac{3(\vec{p}\vec{r})\vec{r} - \vec{p}\,r^2}{r^5}. \tag{1.35}$$

Because dipoles occur only on lattice sites and all $\vec{e}(\vec{R}_n)$ are equal:

$$\vec{p}(\vec{r}) = \sum_{R_n} \alpha\vec{e}(0)\delta(\vec{r} - \vec{R}_n). \tag{1.36}$$

If eqs. 1.34 and 1.35 are valid everywhere, they are certainly valid at $\vec{r} = 0$, so

$$\vec{e}(0) = \vec{E}_i + \sum_{R_n \neq 0} \vec{E}_{dip}(\vec{R}_n). \tag{1.37}$$

Equation 1.37 is a self-consistency relation between $\vec{e}(0) = \vec{E}_{loc}$ and $\vec{E}_i$. For full cubic symmetry the sum over $\vec{R}_n$ vanishes and we have simply $\vec{E}_i = \vec{E}_{loc}$. However, this is not generally true for systems of lower symmetry, such as molecules adsorbed on a surface.

We now have an exact microscopic solution and can proceed to the second step, i. e. averaging the microscopic solutions to obtain their macroscopic counterpart. Eqn. 1.36 can be averaged to

$$\vec{P} = \frac{N}{V}\alpha\vec{E}_{loc} = n\alpha\vec{E}_{loc}, \tag{1.38}$$

where V is the volume of the sample and $n = a^{-3}$ is the volume density of points. The volume average of $\vec{e}(\vec{r})$ is slightly more complicated because the volume integral of a dipole field is not zero, but $-\frac{4\pi}{3}$. Using this result, we find from eqn. 1.34 the average or macroscopic field to be

$$\vec{E} = \vec{E}_{loc}(1 - \frac{4\pi}{3}n\alpha). \tag{1.39}$$

Therefore the uniform microscopic field $\vec{E}_i = \vec{E}_{loc}$ that was actually applied is larger than the uniform macroscopic field $\vec{E}$ that was apparently applied because the induced dipoles oppose on the average the applied field. After some algebra, all fields can be eliminated from eqs. 1.33, 1.38, and 1.39 and we obtain the Clausius-Mosotti result

$$\frac{\overline{\epsilon} - 1}{\overline{\epsilon} + 2} = \frac{4\pi}{3}n\alpha. \tag{1.40}$$

This model shows the connections among microstructure and microscopic and macroscopic fields and polarizations.

The dielectric function of a heterogeneous medium can be calculated when the points in the preceeding example are assigned different polarizabilities. The simplest case is the random mixture of two materials with polarizabilities α_a and α_b:

$$\frac{\overline{\epsilon} - 1}{\overline{\epsilon} + 2} = \frac{4\pi}{3}(\overline{n}_a\alpha_a + \overline{n}_b\alpha_b), \tag{1.41}$$

where $\overline{\epsilon}$ is now the effective dielectric function of the composite. This form involves microstructural parameters that are not measured directly. But if the dielectric functions $\overline{\epsilon}_a$ and $\overline{\epsilon}_b$ of phases a and b are available, we can use eqn. 1.40 to rewrite eqn. 1.41 as

$$\frac{\overline{\epsilon} - 1}{\overline{\epsilon} + 2} = f_a\frac{\overline{\epsilon}_a - 1}{\overline{\epsilon}_a + 2} + f_b\frac{\overline{\epsilon}_b - 1}{\overline{\epsilon}_b + 2}, \tag{1.42}$$

where $f_a = \overline{n}_a/(\overline{n}_a + \overline{n}_b)$ and $f_b = \overline{n}_b/(\overline{n}_a + \overline{n}_b)$ are the volume fractions of the phases a and b. This is the Lorentz-Lorenz effective medium expression [Lor80, Lor16].

Let us suppose next that the separate phases a and b are not mixed on an atomic scale but rather consist of regions large enough to possess their own dielectric identity. Then the assumption of vacuum ($\overline{\epsilon} = 1$) as the host medium in which to embed points is not good. If we suppose that the host dielectric function is $\overline{\epsilon}_h$, then eqn. 1.42 becomes

$$\frac{\overline{\epsilon} - \overline{\epsilon}_h}{\overline{\epsilon} + 2\overline{\epsilon}_h} = f_a \frac{\overline{\epsilon}_a - \overline{\epsilon}_h}{\overline{\epsilon}_a + 2\overline{\epsilon}_h} + f_b \frac{\overline{\epsilon}_b - \overline{\epsilon}_h}{\overline{\epsilon}_b + 2\overline{\epsilon}_h}. \tag{1.43}$$

Specifically, if b represents the dilute phase then we should choose $\overline{\epsilon}_h = \overline{\epsilon}_a$, in which case

$$\frac{\overline{\epsilon} - \overline{\epsilon}_a}{\overline{\epsilon} + 2\overline{\epsilon}_a} = f_b \frac{\overline{\epsilon}_b - \overline{\epsilon}_a}{\overline{\epsilon}_b + 2\overline{\epsilon}_a}. \tag{1.44}$$

Equation 1.44 and the alternative equation obtained with $\overline{\epsilon}_h = \overline{\epsilon}_b$ are the Maxwell-Garnett effective medium expressions [MG04].

In cases where f_a and f_b are comparable, it may not be clear whether a or b is the host medium. One alternative is simply to make the self-consistent choice $\overline{\epsilon}_h = \overline{\epsilon}$, in which case eqn. 1.43 reduces to

$$0 = f_a \frac{\overline{\epsilon}_a - \overline{\epsilon}}{\overline{\epsilon}_a + 2\overline{\epsilon}} + f_b \frac{\overline{\epsilon}_b - \overline{\epsilon}}{\overline{\epsilon}_b + 2\overline{\epsilon}}. \tag{1.45}$$

This is the Bruggeman expression, commonly called the Bruggeman effective-medium approximation (B-EMA) [Bru35]. Although they are related, eqn. 1.44 actually describes a coated-sphere microstructure where a is completely surrounded by b, while eqn. 1.45 refers to the aggregate or random-mixture microstructure where a and b are inserted into the effective medium itself.

What happens if the microstructure is not point like (spherically symmetric) as assumed previously? Let us suppose that all internal boundaries are parallel to the applied field, as in a laminar sample with the field applied parallel to the layers. The boundary condition on tangential $\vec{E}$ shows that the field is uniform everywhere. The polarization is then simply proportional to $\overline{\epsilon}_a$ or $\overline{\epsilon}_b$, according to whether $\vec{r}$ is located in a or b. Averaging everything leads to

$$\overline{\epsilon} = f_a \overline{\epsilon}_a + f_b \overline{\epsilon}_b, \tag{1.46}$$

a simple volume average equivalent to capacitors connected in parallel. If $\vec{E}$ is applied perpendicular to the layers, then $\vec{D}$ is uniform throughout and averaging now leads to

$$\frac{1}{\overline{\epsilon}} = \frac{f_a}{\overline{\epsilon}_a} + \frac{f_b}{\overline{\epsilon}_b}, \tag{1.47}$$

equivalent to capacitors connected in series.

Equations 1.46 and 1.47 are the Wiener absolute bounds to $\overline{\epsilon}$. They are absolute because no matter what the microstructure there can never be less screening than no screening (all boundaries parallel to the field, eqn. 1.46) nor more screening than maximum screening (all boundaries perpendicular to the field, eqn. 1.47). For any composition and microstructure, $\overline{\epsilon}$ must lie on or within the region in the complex $\overline{\epsilon}$ plane enclosed by eqs. 1.46 and 1.47 as long as the microstructural dimensions remain small compared with the wavelength of light. The Wiener bounds are easy to construct since eqn. 1.46 is a straight line between $\bar{\epsilon}_a$ and $\bar{\epsilon}_b$ while eqn. 1.47 is a circle passing through $\bar{\epsilon}_a$, $\bar{\epsilon}_b$, and 0.

Screening is taken into account if eqn. 1.43 is modified to

$$\frac{\bar{\epsilon} - \bar{\epsilon}_h}{\bar{\epsilon} + y\bar{\epsilon}_h} = f_a \frac{\bar{\epsilon}_a - \bar{\epsilon}_h}{\bar{\epsilon}_a + y\bar{\epsilon}_h} + f_b \frac{\bar{\epsilon}_b - \bar{\epsilon}_h}{\bar{\epsilon}_b + y\bar{\epsilon}_h}, \tag{1.48}$$

where $y = (1/l) - 1$, $0 \leq l \leq 1$, l is the screening parameter. Eqn. 1.48 reduces to eqn. 1.46 or 1.47 for $l = 0$ (no screening) or $l = 1$ (maximum screening), respectively. The Lorentz-Lorenz (LL), Maxwell-Garnett (a) (MGa) and Maxwell-Garnett (b) (MGb) effective medium expressions for two phase mixtures are obtained with $y = 2$ and $\bar{\epsilon}_h = 1$, $\bar{\epsilon}_h = \bar{\epsilon}_a$, and $\bar{\epsilon}_h = \bar{\epsilon}_b$, respectively. The B-EMA is obtained with $y = 2$ and $\bar{\epsilon}_h = \bar{\epsilon}$. The choice $l = 1/3$ applies to spherical inclusions appropriate to a heterogeneous system that is macroscopically isotropic in three dimensions. This is equivalent to eqn. 1.43. The equivalent choice for two dimensions is $l = 1/2$ (cylindrical screening) for the transverse component of the dielectric tensor and $l = 0$ (no screening) for the normal component.

Let us consider the "amorphous silicon-void" system as shown in Fig. 1.4, and denote the volume fractions of amorphous silicon and voids as f_α and f_v, respectively. The Wiener absolute bounds are defined by the screening parameter $l = 0$ and $l = 1$ for $0 \geq f_\alpha \geq 1$, i. e. a straight line between $\bar{\epsilon}_v$ and $\bar{\epsilon}_\alpha$ (eqn. 1.46 for no screening) and a circular arc passing through $\bar{\epsilon}_v$ and $\bar{\epsilon}_\alpha$ (eqn. 1.47 for maximum screening) enclosing the largest dashed region in Fig. 1.4, where $\bar{\epsilon}_\alpha$ and $\bar{\epsilon}_v$ denote the dielectric function of amorphous silicon and voids, respectively. The values $\bar{\epsilon} = \bar{\epsilon}_{||}$ and $\bar{\epsilon} = \bar{\epsilon}_\perp$ corresponding to the known value of $f_\alpha = 1 - f_v$ can be calculated for no screening (eqn. 1.46) and for maximum screening (eqn. 1.47), respectively. $\bar{\epsilon}_{||}$ lies on the straight line between $\bar{\epsilon}_\alpha$ and $\bar{\epsilon}_v$ and $\bar{\epsilon}_\perp$ lies on the circular arc between $\bar{\epsilon}_\alpha$ and $\bar{\epsilon}_v$.

If the composition $f_a = 1 - f_v$ is fixed, the Maxwell-Garnett expression (eqn. 1.44) provides further absolute limits substituting $\bar{\epsilon}_h = \bar{\epsilon}_\alpha$ and $\bar{\epsilon}_h = \bar{\epsilon}_v$ in eqn. 1.43 for $0 \geq l \geq 1$. In this case, regardless of the shapes of the constituent regions (i. e. the value of the screening parameter l) $\bar{\epsilon}$ must lie within the smaller range defined by the circular arcs passing through $\bar{\epsilon}_\perp$ and $\bar{\epsilon}_{||}$ and either $\bar{\epsilon}_\alpha$ or $\bar{\epsilon}_v$.

For a known composition and two-dimensional ($l = 1/2$) or three dimensional ($l = 1/3$) macroscopic isotropy the smallest dashed range is defined by the so called Bergman-Milton limits through lines $\bar{\epsilon}_h = x\bar{\epsilon}_\alpha + (1-x)\bar{\epsilon}_v$ and $\bar{\epsilon}_h^{-1} = x\bar{\epsilon}_\alpha^{-1} + (1-x)\bar{\epsilon}_v^{-1}$ for $0 \geq x \geq 1$, passing through the Maxwell-Garnett points $\bar{\epsilon}_{MG_\alpha}$ and $\bar{\epsilon}_{MG_v}$ and either $\bar{\epsilon}_\perp$ or $\bar{\epsilon}_{||}$. $\bar{\epsilon}_{MG_\alpha}$ and $\bar{\epsilon}_{MG_v}$ lie on the straight line and on the circular arc, respectively, between $\bar{\epsilon}_\perp$ and $\bar{\epsilon}_{||}$.

If $\bar{\epsilon}_a$ and $\bar{\epsilon}_b$ are nearly equal (see the straight line and the circular arc between $\bar{\epsilon}_\alpha$ and $\bar{\epsilon}_c$ as shown in Fig. 1.4), the allowed ranges are smaller than in the case of a very different dielectric function. If the allowed ranges are small, then the shape distributions are much less important than the composition. In general, shape distribution effects are more important when the constituent dielectric functions are widely different, while composition is more important if they are similar. The relative importance of composition and shape distribution may change with wavelength.

The LL theory ($\bar{\epsilon}_h$) is a poor choice for condensed-matter applications where space is filled completely and the assumption of a vacuum host is obviously artificial. The

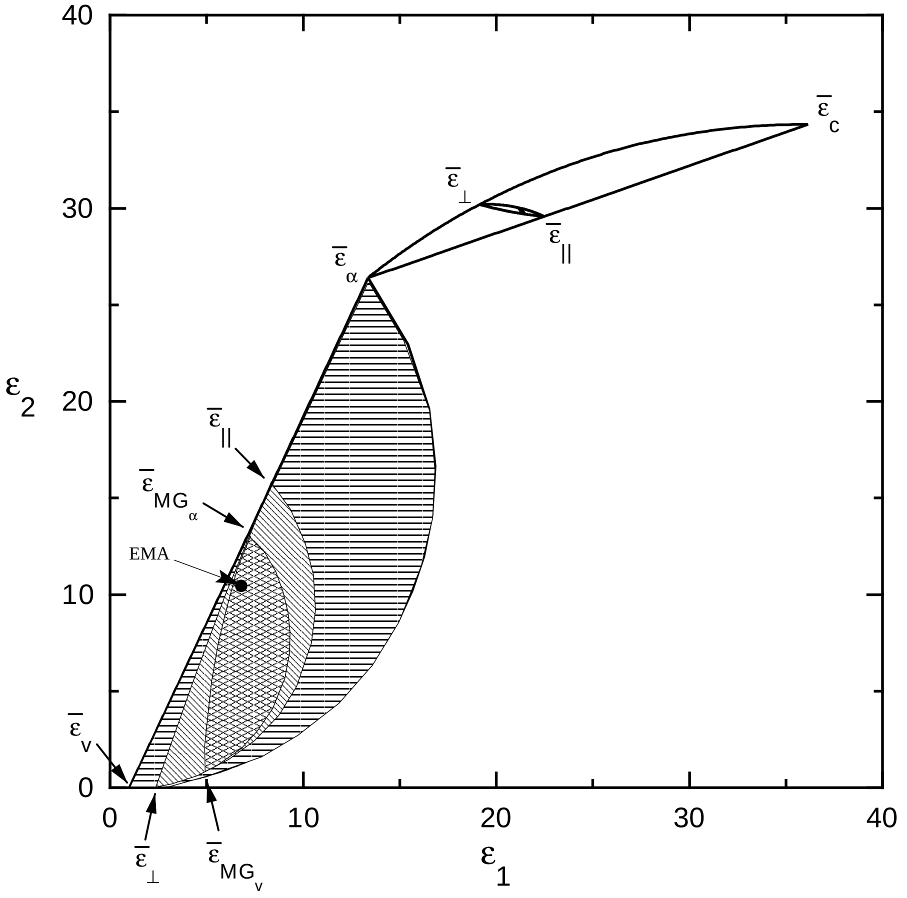

Figure 1.4. Limits on the allowed range of $\bar{\epsilon}$ for composites with two components: $\bar{\epsilon}_\alpha$-$\bar{\epsilon}_v$ and $\bar{\epsilon}_\alpha$-$\bar{\epsilon}_c$, where $\bar{\epsilon}_\alpha$, $\bar{\epsilon}_v$ and $\bar{\epsilon}_c$ denote the dielectric function of LP-CVD deposited amorphous silicon, voids and single-crystalline silicon evaluated at the Hg-arc UV line of $\lambda = 365$ nm, where $\bar{\epsilon}_c = 36.14 + i34.34$ and $\bar{\epsilon}_\alpha = 13.36 + i26.40$ (taken from Ref. [Asp81]). The Wiener absolute bounds for the $\bar{\epsilon}_\alpha$-$\bar{\epsilon}_v$ composites at arbitrary composition and microstructure (i. e. for screening parameters between 0 and 1 and compositions of $0 \geq f_\alpha \geq 1$, where $f_\alpha = 1 - f_v$) are defined by the largest dashed region enclosed by the line and circular arc between $\bar{\epsilon}_\alpha$ and $\bar{\epsilon}_v$. The Maxwell-Garnett expression (eqn. 1.44) provides further absolute limits substituting $\bar{\epsilon}_h = \bar{\epsilon}_\alpha$ and $\bar{\epsilon}_h = \bar{\epsilon}_v$ in eqn. 1.43 for $0 \geq l \geq 1$ enclosed by the circular arcs passing through $\bar{\epsilon}_\perp$ and $\bar{\epsilon}_{||}$ and either $\bar{\epsilon}_\alpha$ or $\bar{\epsilon}_v$. For a known composition and two-dimensional ($l = 1/2$) or three dimensional ($l = 1/3$) macroscopic isotropy the smallest dashed range is defined by the so called Bergman-Milton limits through lines $\bar{\epsilon}_h = x\bar{\epsilon}_\alpha + (1-x)\bar{\epsilon}_v$ and $\bar{\epsilon}_h^{-1} = x\bar{\epsilon}_\alpha^{-1} + (1-x)\bar{\epsilon}_v^{-1}$ for $0 \geq x \geq 1$, passing through the Maxwell-Garnett points $\bar{\epsilon}_{MG_\alpha}$ and $\bar{\epsilon}_{MG_v}$ and either $\bar{\epsilon}_\perp$ or $\bar{\epsilon}_{||}$. The dielectric function calculated using the Bruggeman effective-medium approximation (denoted as EMA in the figure) for the composition of $f_\alpha = 0.6$ is also shown in the plot ($\bar{\epsilon} = 6.62 + i10.66$). The same boundaries are also plot for the $\bar{\epsilon}_\alpha$-$\bar{\epsilon}_c$ system, but the allowed ranges are so small that only the region for the Bergman-Milton limits (the lines between $\bar{\epsilon}_\perp$ and $\bar{\epsilon}_{||}$) are visible in the applied scale.

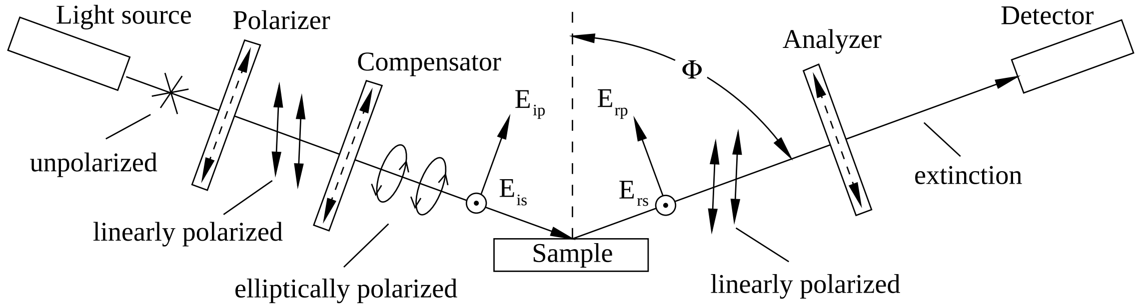

Figure 1.5. Principle of a polarizer-compensator-sample-analyzer (PCSA) null ellipsometer.

choice of host dielectric function indicates that the MG models are best suited to describing configurations where the inclusions are completely surrounded by the host material. The EMA most accurately represents the aggregate structure, where an inclusion may come in contact with different materials, including material of its own type. The EMA and MG models become equivalent in the limit of dilute mixtures where the probability of an inclusion contacting another of the same type is small. EMA is favored in the absence of any independent information about microstructure because it reduces to the appropriate MG limit in either case and treats all constituents on an equal basis.

1.1.4 Instrumentation

Null ellipsometry

The ellipsometer is basically an optical instrument that consists of two arms, whose axes lie in one plane. Fig. 1.5 shows the principle of a polarizer-compensator-sample-analyzer (PCSA) null ellipsometer. Here, the entrance optics consist of a polarizer and compensator, or quarter-wave plate, and the exit optics consist of a second polarizer, or analyzer. The polarizer-compensator combination operates as a general elliptical polarizer. To perform a measurement, the azimuth angles for the polarizer (P), compensator (C), and analyzer(A) have to be found such that the light flux falling on the photodetector is extinguished. Or more visually, the ellipticity of the incident beam is adjusted with the polarizer and compensator so that it is exactly canceled by reflection, i. e. the reflected beam is linearly polarized. This linearly polarized beam can then be extinguished by rotating the analyzer properly. (The null ellipsometer is the optical analogue of the AC impedance bridge.) Besides the three azimuth angles P, C, and A, the relative retardation δ_c of the compensator is a fourth parameter that can be adjusted in search for the null condition, if a variable-retardation compensator is used. Reading the azimuthal angles P, C, and A at the null condition, $\overline{\rho}$ can be calculated using [Azz87]

$$\overline{\rho}_s = \tan A \frac{\tan C + \overline{\rho}_c \tan(P - C)}{\overline{\rho}_c \tan C \tan(P - C) - 1}, \tag{1.49}$$

where

$$\overline{\rho}_c = T_c e^{j\delta_c}. \tag{1.50}$$

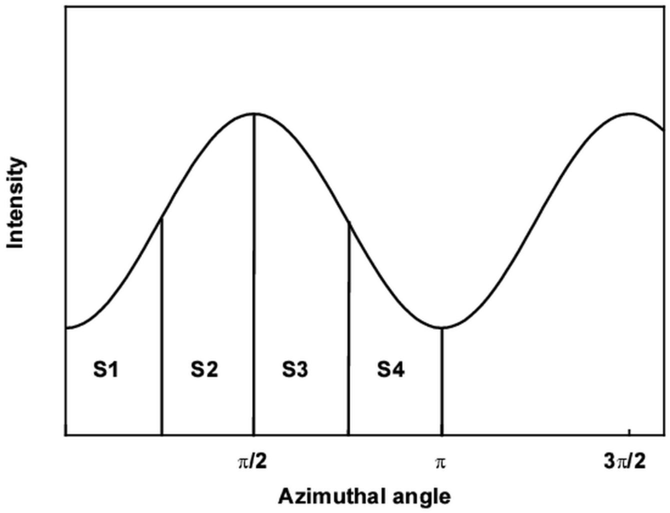

Figure 1.6. Detector signal at a rotating analyzer or a rotating polarizer ellipsometer as a function of the azimuthal angle of the rotating component.

If the compensator acts as an ideal quarter-wave retarder, then $\delta_c = -\frac{1}{2}\pi$ and $T_c = 1$, so in this case $\overline{\rho}_c = -j$.

Photometric ellipsometry

In null ellipsometry information about the optical system under measurement is contained in those values of the azimuthal settings (P, C, A) of the optical elements, the relative phase retardation of the compensator (δ_c) and, in case of measurements on surfaces, the angle of incidence (Φ) that reduce the detected light flux to zero. Photometric ellipsometry, on the other hand, is based on utilization of the variation of the detected light flux as a function of one or more of the above parameters (azimuth angle, phase retardation, or angle of incidence). The raw data from a photometric ellipsometer includes intensity signals that are obtained at prescribed conditions.

Only a few of the many photometric designs have been considered sufficiently practical. The simplest of these are the rotating-analyzer ellipsometer (RAE), and its complement, the rotating-polarizer ellipsometer (RPE). The latter configuration is used in the present study (SOPRA ES4G and SOPRA MOSS-OMA ellipsometers, see Section 2.1). In these configurations the entrance and exit optics consist of single polarizing elements. One of these is rotated mechanically, while the other is held fixed. The advantages are the simplicity and the absence of a compensator. The only wavelength-dependent element is the sample itself. A second advantage is, that the transmitted intensity has a very simple Fourier spectrum consisting of a single AC component on a DC background. The detector signal as a function of the azimuthal angle of the rotating component is shown in Fig. 1.6. Disadvantages include the requirement of either a rigorously unpolarized source for an RPE or a rigorously polarization-insensitive detector for an RAE. In addition, as with all photometric systems, the detector must be rigorously linear or has to be calibrated for non-linearity. Finally, these configurations cannot distinguish between circularly polarized light or unpolarized light or between the right and left handedness of circularly polarized light.

In the case of a rotating-analyzer ellipsometer the detector signal takes the form of

$$I = I_0(\alpha(A)\cos 2P + \beta(A)\sin 2P + 1), \tag{1.51}$$

where A and P are the azimuth angles of the analyzer and polarizer, respectively. α and β are the Fourier components.

This equation shows that the zeroth and second harmonics in the Fourier-transform of the signal I contain all the information needed for the determination of the complex reflectance ratio $\overline{\rho}$. The first harmonics can be used to adjust the beam path. If the first harmonics are low, then the signal is not distorted by undesirable internal reflections at the optical components. The Fourier-components can be calculated using the Fourier-analysis of the detector signal, but the most frequently used method is the Hadamard-transformation. Using the sums (see Fig. 1.6)

$$S_1 = \int\limits_0^{\frac{\pi}{4}} I(P)dP, \tag{1.52}$$

$$S_2 = \int\limits_{\frac{\pi}{4}}^{\frac{\pi}{2}} I(P)dP, \tag{1.53}$$

$$S_3 = \int\limits_{\frac{\pi}{2}}^{\frac{3\pi}{4}} I(P)dP, \tag{1.54}$$

$$S_4 = \int\limits_{\frac{3\pi}{4}}^{\pi} I(P)dP, \tag{1.55}$$

the Fourier-components α and β, as well as I_0 can be written as

$$\alpha = \frac{S_1 - S_2 - S_3 + S_4}{2I_0}, \tag{1.56}$$

$$\beta = \frac{S_1 + S_2 - S_3 - S_4}{2I_0}, \tag{1.57}$$

$$I_0 = \frac{S_1 + S_2 + S_3 + S_4}{\pi}. \tag{1.58}$$

In order to express the ellipsometric angles $\tan\Psi$ and $\cos\Delta$ using α and β, one has to write the detector signal I as a function of the azimuthal angles of the analyzer and the polarizer, and as a function of the reflexion coefficients ($\overline{r}_p$ and $\overline{r}_s$) of the sample. The electric field components ($\overline{E}_{d,p}$ and $\overline{E}_{d,s}$) at the detector can be written as

$$\underset{\textit{Detector}}{\begin{bmatrix} E_{d,p} \\ E_{d,s} \end{bmatrix}} = \underset{\textit{Analyzer}}{\begin{bmatrix} 1 & 0 \\ 0 & 0 \end{bmatrix}} \underset{\textit{Rotation}}{\begin{bmatrix} \cos A & \sin A \\ -\sin A & \cos A \end{bmatrix}} \underset{\textit{Sample}}{\begin{bmatrix} \overline{r}_p & 0 \\ 0 & \overline{r}_s \end{bmatrix}} \underset{\textit{Rotation}}{\begin{bmatrix} \cos P & -\sin P \\ \sin P & \cos P \end{bmatrix}} \underset{\textit{Polarizer}}{\begin{bmatrix} 1 & 0 \\ 0 & 0 \end{bmatrix}} \underset{\textit{Source}}{\begin{bmatrix} E_p \\ E_s \end{bmatrix}}. \tag{1.59}$$

The product of the multiplication of the matrices is

$$\begin{aligned} I = |\overline{E}_d|^2 &= (|\overline{r}_p|^2 \cos^2 A \ \cos^2 P + |\overline{r}_s|^2 \sin^2 A \ \sin^2 P \\ &+ (\overline{r}_p \overline{r}_s^* + \overline{r}_p^* \overline{r}_s) \cos A \ \sin A \ \cos P \ \sin P)|E_0|^2. \end{aligned} \tag{1.60}$$

$\overline{r}_p$ and $\overline{r}_s$ are the reflection coefficients defined in eqn. 1.5 of Section 1.1.1. After linearization and comparison with eqn. 1.51, α and β can be calculated:

$$\alpha = \frac{\tan^2\Psi - \tan^2 A}{\tan^2\Psi + \tan^2 A}, \tag{1.61}$$

$$\beta = 2\cos\Delta\frac{\tan\Psi\ \tan A}{\tan^2\Psi + \tan^2 A}. \tag{1.62}$$

From these equations tanΨ and cosΔ can be expressed as

$$\tan\Psi = |\tan A|\sqrt{\frac{1+\alpha}{1-\alpha}}, \tag{1.63}$$

$$\cos\Delta = sign(\tan A)\frac{\beta}{\sqrt{1-\alpha^2}}. \tag{1.64}$$

Calibration

Sources of measurement errors and the calibration of ellipsometers are extensively studied in the literature [Azz87, Rie87, Asp74, Bau96, Hol86, dN89]. In the following the calibration method of the ellipsometers (SOPRA ES4G and SOPRA MOSS-OMA) used in this work is described (see also [sop]).

In the practice, the mechanical null-position of the rotating elements of the ellipsometer (analyzer, polarizer, compensator) doesn't coincide with the true optical null-position, i. e. with the plane of incidence. Furthermore, the optical null-position can change by changing the sample, or moving the arms of the ellipsometer. Consequently, every time the sample or the optical alignment is changed, a calibration for the azimuth angle of the rotating elements has to be made. When using an autocollimation telescope, the sample alignment can be verified, so that the calibration after sample change can be avoided.

In the absence of errors the irradiance at the detector exhibits the form of eqn. 1.51. In a real system for a rotating polarizer ellipsometer eqn. 1.51 takes the form [Hol86]

$$\begin{aligned} I_d &= I_0\eta[\alpha(A_s+A_0)\cos(2\omega t+2P_0+\Phi)+\beta(A_s+A_0)\sin(2\omega t+2P_0+\Phi)] \\ &= 1+\alpha'(A_0,P_0,\Phi)\cos(2\omega t)+\beta'(A_0,P_0,\Phi)\sin(2\omega t). \end{aligned} \tag{1.65}$$

Φ describes the delay caused by the detector, and η stands for the reduction of the second harmonics in the Fourier-transform of the signal caused by the non-linearity of the detector. A_s is the azimuth of the analyzer, A_0 and P_0 stand for the offset values. The components α' and β' contain the parameters that describe the non-ideality of the system:

$$\begin{bmatrix} \alpha' \\ \beta' \end{bmatrix} = \begin{bmatrix} \cos(2P_0+\Phi) & \sin(2P_0+\Phi) \\ -\sin(2P_0+\Phi) & \sin(2P_0+\Phi) \end{bmatrix} \begin{bmatrix} \alpha(A_s+A_0) \\ \beta(A_s+A_0) \end{bmatrix}. \tag{1.66}$$

The idea for the determination of A_0 is to find a function of A_0 that has a special property at the optical null-position. Such a function is the so called residuum function, which takes the form

$$R = 1-(\alpha'^2+\beta'^2) = 1-\eta^2[\alpha^2(A_s+A_0)+\beta^2(A_s+A_0)]. \tag{1.67}$$

Substituting α and β determined in equations 1.61 and 1.62 into eqn. 1.67, R can be expressed by the parameters η, $\overline{r}$, Δ, A_s, and A_0:

$$R = 1 - \eta^2 + \left[\frac{\eta \sin[2(A_s + A_0)]|\overline{r}_p||\overline{r}_s| \sin\Delta}{\cos^2(A_s + A_0)|\overline{r}_p|^2 + \sin^2(A_s + A_0)|\overline{r}_s|^2}\right]^2. \tag{1.68}$$

In most cases

$$|\overline{r}_p||\overline{r}_s| \sin\Delta \neq 0, \tag{1.69}$$

thus the minimum of eqn. 1.68 is at

$$A_s + A_0 = m\frac{\pi}{2}. \tag{1.70}$$

In the case of $A_s = A_0$ determined by the minimum of eqn. 1.68, the analyzer is located at the optical null-position. This is the calibrated offset. The calibration of a rotating analyzer ellipsometer can be performed using the above equations by exchanging the analyzer angle (A) and the polarizer angle (P).

α' and β' measured at this position of the analyzer are the calibrated values α_c and β_c. Then the ideal values α and β can be calculated from the measured α' and β' values using a matrix of the calibration values α_c and β_c:

$$\begin{bmatrix} \alpha \\ \beta \end{bmatrix} = \frac{1}{\alpha_c^2 + \beta_c^2} \begin{bmatrix} \alpha_c & \beta_c \\ -\beta_c & \alpha_c \end{bmatrix} \begin{bmatrix} \alpha' \\ \beta' \end{bmatrix}. \tag{1.71}$$

Furthermore, the procedure is extended for the cases, when Δ has a value close to 180°. Then eqn. 1.68 cannot be used, because eqn. 1.69 doesn't apply. In this case the following function provides a better possibility for calibration [Hol86, dN89]:

$$\tan(\gamma_2 - \gamma_1) = \frac{-\sin 4\Psi \ \cos\Delta \ \sin[2(A_{s1} + A_0)]}{\sin^2[2(A_{s1} + A_0)] \ \sin^2 2\Psi \ \cos^2(\Delta - 1)}, \tag{1.72}$$

where

$$\gamma_1 = \arctan\frac{\beta'}{\alpha'} \quad \text{for} \quad A_{s1}, \tag{1.73}$$

and

$$\gamma_2 = \arctan\frac{\beta'}{\alpha'} \quad \text{for} \quad A_{s1} + \frac{\pi}{2}. \tag{1.74}$$

Compared to eqn. 1.68, the calculation in eqn. 1.72 is made by using cosΔ in spite of sinΔ. Consequently, the minimum can be determined at $\Delta = 180°$.

1.2 Applications of ellipsometry

Although the principles of ellipsometry date back to the late 19th century, this technique was not widely used until the beginning of 1960s. The evaluation of ellipsometric measurements entails the solution of relatively complicated complex non-linear equations (see eqn. 1.31 on page 7) which can be solved analytically only in a few special cases but require numerical approaches in most instances. An ellipsometric analysis was, therefore, not practical prior to the availability of sufficiently powerful data processing equipment. Only gradually, ellipsometry was introduced into an industrial area like microelectronics technology, first, with nomographs for the measurement evaluation which had been generated by the instruments' manufacturers on a mainframe computer. For example, a book has been published that contains tables and curves showing the dependence of Ψ and Δ on two parameters: the thickness and refractive index of the oxide film for the air-SiO_2-Si system at selected mercury and He-Ne laser spectral lines [Ger71]. By the end of the 1970s, self-contained units were introduced on the market which featured, in general, an automated measurement and internal data processing, based on a microcomputer. However, most of these instruments, and the computer programs supplied with them for measurement evaluation, are tailored to large-scale standard applications like the measurement of the thicknesses and refractive indices of homogeneous thin dielectric films which were deposited directly on a semiconductor substrate with known optical properties.

Ellipsometry provides a lot of possibilities for the user in the analytics, structural studies, product development, or quality control. In contrast to the 1980s, when industrial ellipsometry still sacrificed flexibility and, to a certain degree, accuracy for the ease of operation [Rie87], today ellipsometry is a powerful tool in the industrial applications because of its high speed, high flexibility, high accuracy and friendly user interface. A wide spectrum of wavelengths is covered by using spectroscopic ellipsometry, assuring that almost every application can find a suitable spectral range. The ever growing amount of reference data and experience led to an increased number of applications. New developments of industrial ellipsometers are being made in two directions: ellipsometers are being improved either (i) to occupy new fields of applications or (ii) to provide an easier operation [Neu95]. The number of *in situ* or on-line instruments increases rapidly in the clean rooms. *In situ* during-process ellipsometry offers great promise for monitoring and control of a wide variety of microelectronics processes. The speed of the measurement and the non-invasive character of ellipsometry appear to be very elegant and reliable in this field. In 1995 there were 250 spectroscopic ellipsometers in use worldwide [Neu95]. 40 from that was installed in Germany, one half of them after 1992. The increasing importance of spectroscopic ellipsometry is evident alone from these numbers.

Table 1.1 shows the major process steps in silicon microelectronics together with the material properties that can be measured by SE [Ire93].

Up to now, the film growth processes have received most of the attention from ellipsometry. Typically, film properties such as thickness and refractive index are measured *ex situ* using routine automatic ellipsometers with significant component and angle of incidence errors often greater than 0.1°. However, with the employment of thin films the realization of the crucial nature of interfaces, and the need for process monitoring and control, it is now clear that the era of "low end" ellipsometry use is over.

Generally, SE can be applied in the following cases [Fri97]:

- Determination of the refractive index as a function of the wavelength for mirror polished substrates. The calculated n and k values can be used as references for the evaluation of measurement of more complex structures.
- Accurate determination of n versus the wavelength and the thickness of a transparent film on a known substrate.

Table 1.1. Major process steps in silicon microelectronics together with the material properties that can be measured by SE (after [Ire93]).

Silicon process step	Property by ellipsometry
Crystal growth	Solidification
Wafering	Surface quality
Oxidation	Film thickness and index
Chemical vapor deposition	Film thickness, index, structure, composition, roughness, density, crystallinity
Cleaning	Surface quality
Etching	Film thickness and damage
Metalization	Morphology
Lithography	Resist thickness

- Computation of $\overline{n} = n - ik$ versus the wavelength for a layer of known thickness [Fri92a, Ger88].

- Comparison of simulated and measured parameters of ideal multi-layers based on a proposed structural model (incident angle, layer thicknesses and materials) [Fri91, Van92].

- Computation of the multilayer thicknesses through linear regression by minimizing the differences between the calculated and recorded spectra. Problem: reference files for refractive indices and the limited number of layers (up to 10) [Van92].

- Introduction and determination of composition of mixed layers, to some extent, by the application of effective medium models (Section 1.1.3) [Pet98b].

- Study of surface and interface roughness, both of which can be replaced by mixed layer [Asp79, Pet98a].

- Determination of profiles in layers with a continously varying refractive index, for example, ion implantation damage and deposited layers [Loh94c, Fri92b, Ved85, McM86, Van91, Pet98c, Pet99b].

In the past few years, the concept of “single wafer processing” has been proposed for microelectronics manufacturing. This concept will prompt a renaissance for ellipsometry in microelectronics. The single wafer processing concept is the use of vacuum processes in sequence. Many of the vacuum processes – the plasma and ion beam processes of deposition, etching and cleaning among others – were developed in basic research laboratories where careful and skilled experimentation, and not manufacturing, takes place. In order to effectively utilize single wafer processing, competent process monitoring and control must exist. One cannot wait until a process step ends to perform diagnostics and make process improvements. These requirements translate into real time measurements with sensitivity and accuracy. Ellipsometry has been shown to have the necessary competence.

In the fields of semiconductors, optics, or microelectronics reference samples are often prepared for comparison or calibration of the measurement tools. The physical parameters of the reference samples have to be made with high accuracy, because this results are taken as calibration values. Such kind of information are the reference data for refractive index used by optical measurements. To be able to measure the thickness of the silicon oxide, one has to know the refractive index of the silicon substrate with high precision. The precision of the measurement of the silicon oxide depends on the accuracy of the reference data of the silicon substrate. Ellipsometry is used very often for such reference measurements. Using spectroscopic ellipsometry, the refractive index can be measured in a wide spectral range. For these measurements the step between the several wavelength values is chosed to be small, in order to be able to follow the little changes. This is especially important at the critical points where the refractive index changes rapidly with the wavelength. There is a need of a measurement at multiple angles of incidence, if the sample is not homogeneous or if a surface layer is present, which increases the number of the unknown parameters above 2 (supposed that the refractive index of the layer or the substrate is known, and the values to be determined are the layer thickness and $\overline{n}$ for the other). Surface quality is a crucial factor at the measurement of refractive index reference data. Surface non-ideality has to be minimized, or involved in the calculation.

Quality control and device development require extremely good repeatability. Very often, a relatively narrow spectral range with fixed angle of incidence is enough for the measurement of the needed parameters with the required accuracy and speed.

In some cases there is a demand to be able to measure in a small spot, or in many points, automatically, with high speed (for example to check the inhomogeneity). Using advanced softwares, automatic ellipsometers are in use for the fast and precise calculation of inhomogeneity.

Reducing the spot size is a more serious problem for spectroscopic ellipsometry than for single-wavelength ellipsometry. Since in the latter case lasers are used as light sources, the spot size can be shrinked down to 10 μm. For spectroscopic ellipsometry the most frequently used light source is the xenon-lamp. In this case, a possible method for the reduction of the spot size is the use of an aperture, which reduces the intensity. Using this method, a spot size of 0.5 mm can be achieved. Further reduction is possible by focusing the beam (micro-spot). For micro-spot, lenses are used which also lower the intensity by some percent, but more important is that the incident beam won't be collimated, resulting in an error of the angle of incidence. This error is particularly important when determining the refractive index. The micro-spot method can be used in the production control, or on-line quality control as long as the measured values are layer thicknesses. There are special ellipsometers in the quality control, which focus the beam on a 80 μm×150 μm spot using optics optimized for a given angle of incidence. These ellipsometers (for example SOPRA MLM) are able to measure up to 10 points per minute or 30 samples per hour.

An ellipsometer can be used as a reflectometer without changing the configuration. The reflexion coefficient can be calculated from the ellipsometric angles $\tan\Psi$ and $\cos\Delta$. In the widely used configurations using a rotating analyzer or a rotating polarizer cosΔ is measured directly (see eqn. 1.64 in page 16). Consequently, we don't know the sign of Δ, only its absolute value. The structure of the measured sample can be characterized or the refractive index can be measured without knowing the sign of Δ. However, the knowledge of the sign is important in cases like *in situ* layer thickness monitoring using a beam guiding system (see Chapter 5).

1.2.1 Precision

Random measurement errors are the limiting factor in determining small parameter changes in a measurement. The ability to measure small parameter changes with a high degree of confidence is refered to as the resolution, or precision [Hau73, Coo63]. I will use precision in this sense and differentiate it from accuracy, which is the ability of the measurement to closely determine the true value of the measured parameter in the presence of systematic errors. The precision of the measurements made by spectroscopic ellipsometry is typically approx. 10^{-3} for both tanΨ and cosΔ (this is the precision of the SOPRA ES4G spectroscopic ellipsometer which I use in the following study together with a SOPRA MOSS-OMA *in situ* ellipsometer having a lower precision). This means that n and k can be determined with a precision of 5×10^{-4} for a homogeneous bulk material. Obviously, this result depends on the material of the substrate, the angle of incidence, and the wavelength of the measuring light. When calculating n and k using dispersion equations, the precision can be multipled by 3 or 5. In this case the parameters of the dispersion equation and the angle of incidence are varied using linear regression to minimize the difference between the measured and calculated spectra. The precision increases because of the decrease of the number of unknown parameters.

Ellipsometry is very sensitive to the surface or surface layer properties. Fig. 1.7 shows the effect of little changes of the surface on the measured ellipsometry spectra. Note that while tanΨ is not sensitive to these little changes, there is a significant difference in the cosΔ spectra for the different surface structures. This means that the ratio of the absolute values of the parallel and perpendicular components of the polarized light incident on the surface doesn't change, but there is a significant change in the phase shift of the components between 300 nm (≈4.1 eV) and 370 nm (≈3.4 eV). The borders of this range are determined by the E_1 (3.4 eV) and the E_2 (4.2 eV) inter-band transitions of the single-crystalline silicon. A 1 nm and a 0.5 nm surface oxide layer causes a shift of 0.03 and 0.015, respectively, in cosΔ at a wavelength of approx. 300 nm (see the insert in Fig. 1.7). These changes are still an order of magnitude higher than the measurement sensitivity of 0.001 for cosΔ (for a SOPRA ES4G spectroscopic ellipsometer).

The ability of the measurement of the phase makes ellipsometry extremely powerful. When compared with reflectometry, where accurate measurements generally require double-beam methods, ellipsometry is a double-beam method in which one polarization component serves as amplitude and phase reference for the other. This makes ellipsometry capable for obtaining phase information and, as a result, being very sensitive to the surface conditions.

Considering the above example, the surface oxide layer with a thickness of 0.5 nm, which means approximately one atomic layer, causes a change in the measured value of cosΔ which is one order of magnitude higher than the measurement sensitivity.

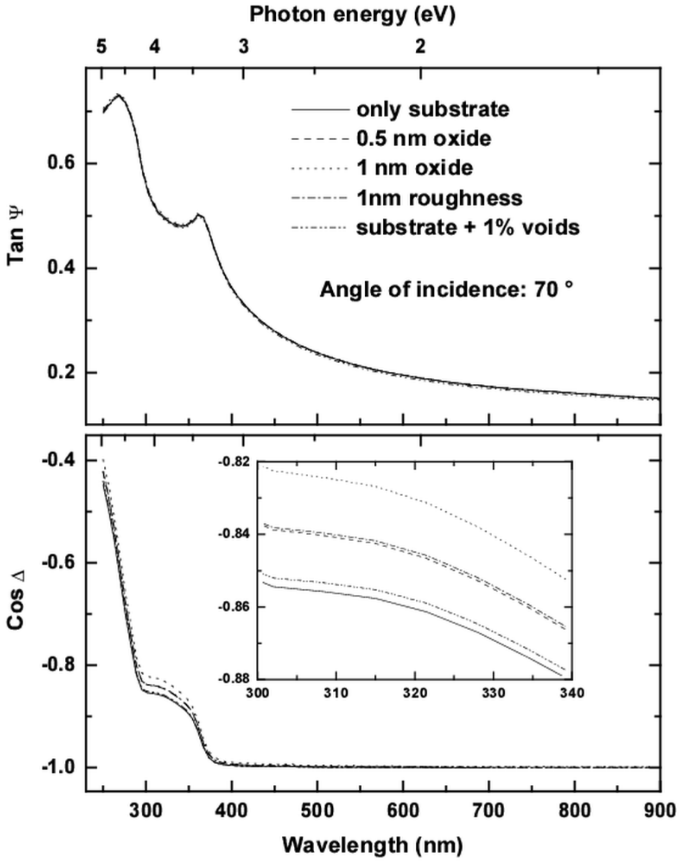

Figure 1.7. Simulated spectra demonstrating the effect of little changes of the surface and substrate properties on tanΨ–cosΔ spectra.

Consequently, using *in situ* ellipsometry, layer growth can be monitored monolayer by monolayer. (A good example is a study of Fujiwara et al. [Fuj97], in that real time spectroscopic ellipsometry was applied to characterize compositionally graded structures of PECVD a-$Si_{1-x}C_x$:H in structures of thickness ranging from 50 to 130 Å. In the depth profiles of the graded structures, an apparent resolution of ≈10 Å is obtained with a composition uncertainty of ±0.004.)

The surface roughness layer in Fig. 1.7 was simulated with a density deficient over-layer by mixing 70% single-crystalline silicon with 30% voids (i. e. the dielectric function of the ambient) using the B-EMA (Section 1.1.3). The B-EMA describes microscopic roughness if the characteristic dimensions of the microstructure are small compared with the wavelength of the measuring light. In this case the corresponding distortions of the wavefront required to satisfy the boundary conditions will not be important. Then the material can be described as a composite medium. This has been shown to be a good approximation for rough silicon film over a wide spectral range [Asp79]. The change of cosΔ caused by the 1 nm surface roughness (Fig. 1.7) is equivalent with the change caused by a 0.5 nm surface oxide layer. This roughness is below the resolution level of a scanning electron microscope and has only a small effect on light scattering, so it would be very difficult to detect by other means. Atomic force microscopy is a possible method for comparison having a sensitivity limit of approx. 0.09 nm (see Chapter 3). The sensitivity of ellipsometry makes it possible to

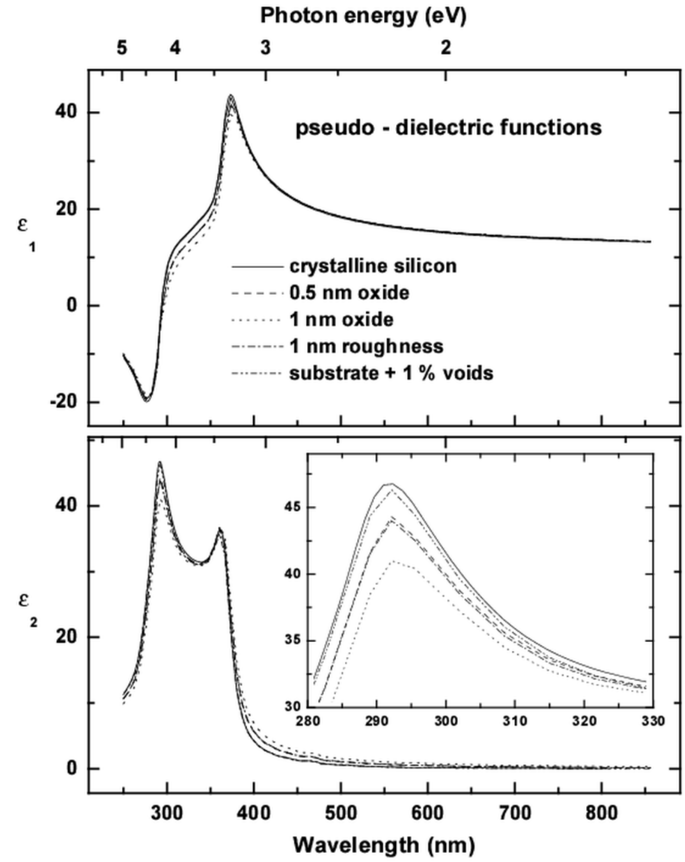

Figure 1.8. Demonstration of the effect of little changes of the surface and substrate properties on the pseudo-dielectric function. The simulated tanΨ and cosΔ spectra for the same models are shown in Fig. 1.7.

decide, whether the surface is atomically smooth or not.

It is also shown in Fig. 1.7 that the density deficit of 1% of the substrate simulated by the model having a mixture of 99% single-crystalline silicon and 1% voids causes also a measurable change in cosΔ.

Fig. 1.8 shows the pseudo-dielectric functions $\langle\overline{\epsilon}\rangle$ corresponding to the models of Fig. 1.7.

Similarly to the spectra shown in Fig. 1.7, the most significant change occurs in the spectral range between the E_1 and E_2 inter-band transitions determined by the two peaks of $\overline{\epsilon}_2$. The insert shows the region close to the E_1 inter-band transition. Even a 1 nm surface roughness layer has a significant effect on the measured dielectric function ($\overline{\epsilon}_2$ decreases from 47 to 43). The 1 nm oxide causes a decrease by 7 in $\overline{\epsilon}_2$ at E_1.

The above results showed the change in the tanΨ–cosΔ spectra caused by a thin surface layer or a density deficit in the substrate. Furthermore, they showed how these changes affected the pseudo-dielectric function. The precision of the determination of the thickness of thin surface layers depends not only on the accuracy of the spectroscopic data, but also on the optical model, the angle of incidence, the wavelength range, the number of the measurement points, the measured material, the homogeneity, and, as shown above, on the surface quality. The precision and the repeatability

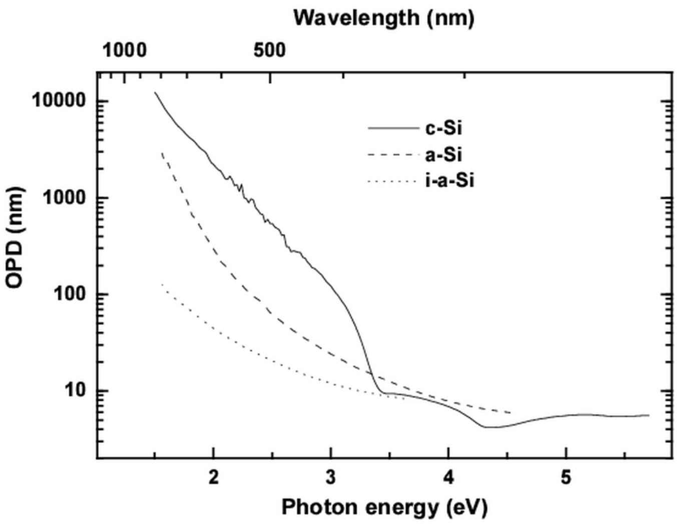

Figure 1.9. Optical penetration depth (OPD) for single-crystalline silicon (c-si) [Asp85], LPCVD deposited amorphous silicon (a-Si) [Jel93] and implanted amorphous silicon (i-a-Si) [Fri92b].

of the layer thickness determination for a single surface layer is approx. 0.1 nm and 0.01 nm, respectively. For layer thicknesses between 100 nm and 2 μm the confidence limit is typically 0.1% which means that, with 95% probability, the deviation of the real layer thickness from the measured one is not more than ±0.1% of the measured thickness. Thicker layers, up to 20 μm, can be measured in the near-infra red range. The spectral range of the commonly used ellipsometers is in the range between 200 nm (quartz limit) and 900 nm. This contains the whole visible range while the lower end is still in the UV range. The UV range is especially advantageous for measuring thin surface layers or surface properties, because the sensitivity is very high in this range (see Figs. 1.7 and 1.8). The penetration depth at the wavelength of 300 nm in the single-crystalline silicon is 5.7 nm. It shows that this wavelength cannot be used for thick layers. Fig. 1.9 shows the optical penetration depth (OPD) for single-crystalline silicon (c-Si) [Asp85], LPCVD deposited amorphous silicon (a-Si) [Jel93] and implanted amorphous silicon (i-a-Si) [Fri92b]. The values are also shown in Table 1.2 for some wavelengths.

The optical penetration depth is defined as $\frac{\lambda}{4\pi k}$. The information depth is roughly 3 times the OPD (obtained from model calculations). The fact that OPD is wavelength-dependent can be exploited as a depth-scan in SE. For the longer wavelength, the penetration depth for amorphous silicon can be less by even one or two orders of magnitude than that of the single-crystalline silicon. The information depth for the implanted amorphous silicon is not more than 600 nm even at the wavelength of 800 nm. The investigation of deeper structures requires the high wavelength region especially if the material has a high absorption like amorphous silicon. There are ellipsometers which can use a wavelength range from 200 nm to 2700 nm. The wavelength range of the Fourier-transform infra red ellipsometers begins at 1600 nm and goes up to 50 μm. The most frequently used range is that between 250 nm and 1700 nm.

Table 1.2. Optical penetration depth (OPD) for single-crystalline silicon (c-si) [Asp85], LPCVD deposited amorphous silicon (a-Si) [Jel93] and implanted amorphous silicon (i-a-Si) [Fri92b].

Wavelength	Penetration depth (nm)		
(nm)	c-Si	a-Si	i-a-Si
210	5.6		
300	5.7	7.2	7.2
350	9.3	11.9	8.7
400	82.2	19.8	12.1
450	255.3	36.8	15.3
500	545.3	64.3	21.1
550	1175	118.1	28.8
600	1768	222.4	38.9
650	3173	457.1	55.1
700	4570	921.7	73.9
750	6610	1801.9	94.7
800	10000	2992.6	219.6

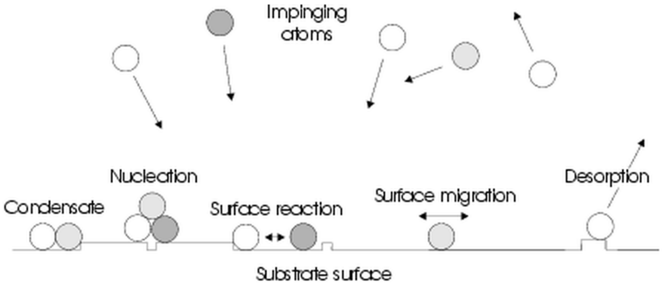

Figure 1.10. Events that occur around the substrate during deposition.

1.3 Chemical vapor deposition

Chemical vapor deposition (CVD) is a technique for synthesizing materials in which chemical components in vapor phase react to form a solid film at the surface of the sample. CVD is a sequential process which starts from the initial vapor phase, progresses through a series of quasi steady-state subprocesses, and culminates in the formation of a solid film in its final microstructure. This sequence consists of five basic steps [Lac85] (Fig. 1.10):

- diffusion of gaseous reactants to the surface,
- adsorption of the reacting species onto surface sites, often after some migration on the surface,
- surface chemical reaction between the reactants, usually catalyzed by the surface,

- desorption of the reaction by-products,
- diffusion of the by-products away from the surface.

By operating at low pressure it is possible to eliminate the diffusion process as the controlling step. Therefore, one of several possible reactions on the surface must be considered, which include adsorption, direct reaction or partial reaction with the surface or with an absorbed species on the surface, diffusion along the surface with possible partial reaction at energy traps, and finally a terminating reaction at a growth site. When two or more species are involved, each species may be undergoing different reactions simultaneously. In the study of such systems, it is necessary to determine the species responsible for process control before a clear understanding can be gained. In some processes, for example low pressure low temperature oxidation (LPLTO), it was necessary to deduce from practical design the process steps responsible for control of the process. Nevertheless, in all cases it was found that the more understood about a process, the easier it was to further its development, whether for optimization or for scale-up.

The basic parameters that control all CVD processes are

- the rate of mass transfer of reactant gases from the ambient gas stream to the wafer surface,
- the rate of reaction of the gases at the wafer surface.

The observed deposition rate G is [Sch86]:

$$G = A\frac{1}{\frac{1}{F}+\frac{1}{R}}, \tag{1.75}$$

where A is a geometric constant, F is the mass transfer rate and R is the surface reaction rate. Under the conditions of atmospheric pressure CVD (APCVD), these two rates are approximately equal. Therefore, in order to obtain uniform deposition, it is necessary to assure both rate conditions are met. The rate of surface reaction is dependent upon reactant gas concentration and temperature, while the rate of mass transfer is also dependent upon the reactant gas concentration as well as upon the gas diffusion across a boundary layer. The common requirement to maintain a uniform reactant gas concentration over the surface of the wafer has been accomplished in APCVD through reactor design and appropriate flow velocity. Reactors for APCVD are designed so that the main gas stream flows over the surface of the wafer. With this design, maintaining good thickness uniformities is difficult, and does not allow a very large throughput.

In contrast, LPCVD processing depends on a surface reaction-controlled process. The surface reaction rate at a given temperature is

$$R = k_1 C_s, \tag{1.76}$$

where k_1 is the chemical reaction constant and C_s is the concentration of the reactant at the surface. C_s is proportional to the partial pressure of the reactant gas and is minimally affected by low-pressure processing, because the partial pressure of the reactant gas is similar in both APCVD and LPCVD. Thus, surface reaction rates or deposition rates are generally not strongly changed by processing at low pressure.

Mass transfer rates are strongly affected by a change in the total pressure. The mass transfer rate is

$$F = \frac{D}{d}\Delta C, \tag{1.77}$$

where D is gaseous diffusivity, d is the boundary layer thickness and ΔC is the reactant gas concentration gradient between the surface of the wafer and the ambient gas stream. The diffusivity is inversely proportional to the total pressure, P:

$$D = \frac{k_2}{P}, \tag{1.78}$$

where k_2 is a constant. The boundary layer thickness can be described by

$$d = k_3 \frac{1}{\sqrt{k_4 v P}}, \tag{1.79}$$

where k_3 and k_4 are constants and v is the gas flow velocity. Typical LPCVD process pressures are less than 10^{-3} atmosphere, therefore diffusivity is increased by a factor of 10^3 relative to APCVD processing. At low pressure, gas velocities are generally 10 to 100 times greater than in atmospheric processes; therefore, d (eqn. 1.79) is 3 to 10 times larger in low-pressure processing. Thus the mass transfer rate, F (eqn. 1.78), is increased more than 10^2 compared to atmospheric processing with all other parameters remaining nearly constant. In the resulting expression for deposition rate, G (eqn. 1.75), the term containing the mass transfer rate becomes small and ineffective, and deposition rate is solely dependent upon surface reaction rates.

Reactors for LPCVD processing can be divided into four basic categories. The first, and most widely used is the horizontal tube reactor. The second type is the vertical tube reactor which operates in much the same manner as the horizontal tube reactor. The third type uses a bell jar, and the fourth type is the single wafer reactor. The features of each type is given in Table 1.3.

Table 1.3. LPCVD reactor characteristics [Sch86]. Recently, the wafer size of 300 mm is being introduced in the microelectronics industry.

Reactor type	Throughput (wafers/hr.)	Maximum wafer size (mm)	Uniformity (%)
Horizontal tube	100	150	± 2-6
Vertical tube	100	200	± 2-6
Bell jar	50-100	150	± 3-6
Single wafer	70-80	200-250	± 1-3

The heart of a horizontal reactor is a quartz tube that provides a concentric cross-section to densely spaced wafers standing on edge that allows as many as 200 wafers to be processed at one time. The tube is concentrically heated with a multiple zone heater (up to 5 zones) that allows precise temperature control. The precision of the temperature control is typically ±1°C or less.

The vertical tube reactor differs from the horizontal reactor basically only in the orientation of the reaction chamber. A major advantage of this reactor is a significant reduction in the clean room footprint. Usually, the wafers are loaded in a horizontal position on a quartz-loading cassette that is raised into the furnace by an elevator mechanism. Gas flow patterns are the same as for the horizontal tube reactor so that there exists no limitations on the processes that can be performed in this reactor type. This kind of CVD reactor has been used for polysilicon deposition also in this study (see Section 2.1).

The single-wafer reactor represents not only a novel design, but also a unique production concept [Sch86]. This is the newest approach to LPCVD processing, and was developed simultaneously by several manufacturers. Besides single wafer operation, these reactors have in common such features as cassette-to-cassette loading, no quartzware, high deposition rates, and exceptionally high uniformity. Although batch site is but a single wafer, these reactors are definitely a production tool with throughputs of 70-80 wafers per hour. Additional features are cold-wall operation that should allow these reactors to deposit refractory metals. Although the throughput decreases as wafer size increases, the advantage normally gained by larger wafers is not totally lost. Whereas not all manufacturers claim a full spectrum of standard processes (all can deposit low temperature oxides and doped glasses), there appears to be no technical inhibitor to prevent development of all processes on these reactors. Acceptance of these reactors in production facilities would represent a significant change in wafer processing.

The low pressure single-wafer reactor offers increased gas phase diffusion, lower gas flows, and often better wafer-to-wafer process control. This reactor type suffers the disadvantage of reduced wafer throughput, often compensated by having multiple reaction chambers [Siv95].

1.4 Preparation and applications of polycrystalline silicon

A wide range of deposition techniques for poly-Si have been investigated. In the early stages of development (1963-1970), physical vapor deposition (PVD) techniques were used; however, unwanted impurities, non-uniform step coverage (±5-10% thickness variations), and low productivity per capital cost prevented widespread use of these methods. In the early manufacturing period (1970-1976), cold wall, atmospheric pressure “epitaxy” reactors were used for poly-Si deposition. Such reactors offered thickness variations of ±5-10% and low productivity per capital cost. The H_2/SiH_4 process at 910°C provided a large grain size after deposition. The N_2/SiH_4 process at 650°C offered smaller grain size, but much worse uniformity. Even with these limitations, Si gate PMOS and NMOS ICs became a major factor in the semiconductor device market in the early 1970s.

The LPCVD process, first introduced commercially in 1976, revolutionized poly-Si deposition and set the stage for MOS ICs to become the dominant device type. This diffusion furnace process reduced deposition costs more than 90%, improved uniformities to ±1-2%, and provided the optimum grain structure for good post-deposition doping control. As a result, yield of MOS ICs was markedly improved, while production costs were reduced. This LPCVD process, with minor variations in reactor geometry, has been the primary means of poly-Si deposition for ICs during the last 14 years, and it shows every indication of continuing this dominance for many years to come.

The overall reaction

$$SiH_4 \;\rightarrow\; Si + 2H_2 \tag{1.80}$$

is still the common method of polysilicon deposition. There is no difference in the deposition mechanism between low and atmospheric pressure processing, and no difference between silane and chlorosilane. The temperature regime used is 600-900°C. Growth rate in this regime is exponentially dependent on the temperature. Using the LPCVD method at a silane pressure of 0.26 mbar and a gas flow of 100 sccm, a transition temperature between amorphous and polycrystalline deposits exists for deposition temperatures close to 580°C ([Kam78], Chapter 2). Under this temperature the deposited layer is amorphous.

Under subatmospheric pressures and temperatures in the regime 600-800°C, the following sequence of reactions is thought to lead to the deposition of polysilicon [Siv95]:

$$\begin{aligned} SiH_4 + 2^* &\rightarrow SiH_2^* + H_2^* \\ SiH_2^* + {}^* &\rightarrow \;Si^* \;+ H_2^* \end{aligned} \tag{1.81}$$

where the *s represent surface adsorption sites. The sites that occur at kinks and ledges on the surface are more favorable for the adsorption of the gas phase silane species. The growth reaction is strongly controlled by adsorption of the reactants at higher temperatures and desorption of adsorbed hydrogen at lower temperatures. Competition for the surface adsorption sites drastically lowers the growth rate.

The deposition of doped films involves the addition of dopant-bearing gases, such as PH_3 or B_2H_6, to the gas stream. Both phosphorus and boron additions modify the growth process: phosphorus lowers the growth rate while boron increases the growth rate.

Experience has revealed that when the process is run at a constant temperature along the length of the process tube, the deposition on wafers in a downstream position was always thinner than those in an upstream position. Moreover, the severity of this non-uniformity became greater as temperature increased. This behavior is the consequence of depletion of silane along the length of the tube. At lower deposition temperatures (near 620°C), where deposition rate is relatively slow, the depletion effect can be overridden with high flow rates and high partial pressure of silane.

The success of the polysilicon deposition process at constant temperature is dependent on the rapid transfer of reaction gases down the reaction tube. Essential to this high gas velocity is a vacuum pumping system with sufficient capacity to provide high gas throughput. Vacuum pumps have long reached a level of technological maturity and very few changes have been made except for the trend toward larger pumps as wafer size has increased [Sch86]. Vane pumps are used almost exclusively and are constructed from materials resistant to chemical attack, primarily acids. The precision to which the temperature is maintained has direct bearing on the precision in thickness uniformity from front to rear along the load. Because of the relatively high activation energy, a temperature deviation of 1°C will create a 2.5% difference in thickness. However, this difference is often much greater. For example, if there should be a +1°C temperature deviation in an upstream position, there will be not only a 2.5% increase in thickness at that position, but it will create a 2.5% decrease in thickness downstream as a consequence of relative depletion. Therefore, in order to assure acceptable wafer-to-wafer thickness uniformity, it is necessary to maintain a ±0.5°C from constant temperature at all points along the load. Many equipment manufacturers have found that this requirement was very difficult with large wafer sizes when 3-zone furnace heaters were used, and many are now using 5-zone heaters for this process in order to gain better control along the length of the reaction tube.

Understanding and utilizing the advantages offered by poly-Si was one of the most important fundamental developments in the history of integrated circuits [Ham90]. Poly-Si is so useful, because it

- forms an adherent oxide,
- adsorbs and re-emits dopants,
- has good step coverage if deposited by CVD,
- matches mechanical properties of Si single crystal,
- has a high melting point,
- has a compatible work function for MOS devices,
- absorbs heavy metals (gettering),
- forms high conductivity silicides,
- is compatible with HF.

These properties make poly-Si uniquely suited to be a primary local interconnect material, and its ability to form silicides extends that application to longer interconnect lines. Its compatibility with IC processing and its good step coverage provided by CVD offers many advantages in bipolar, MOS, and BiCMOS circuits, because it

- provides low MOS threshold voltage,
- fills trenches,
- permits SAliciding,
- provides long gate oxide wear-out times,
- provides a wide range of resistivities,
- permits oxide reflow process temperatures,
- simplifies processing,
- can be selectively deposited,

- permits shallow, high quality junctions,
- forms silicide thin film resistors.

These advantages have resulted in many device applications, including

- self-aligned MOS gates,
- source/drain contacts,
- multilayer interconnects,
- dielectric isolation,
- 3-D structures,
- non-volatile floating gates,
- fusible links,
- emitter & base contacts,
- thin film devices,
- emitter diffusion source.

New device applications for poly-Si include

- poly-Si contacts that
  - eliminate Al alloy spiking,
  - provide high quality, extremely shallow junctions,
  - permit high gain emitters in bipolar devices;
- selective deposition for
  - local interconnect straps,
  - via and contact plugs,
  - 3-dimensional structures;
- trench fill;
- stacked capacitors;
- self-aligning silicide;
- thin film devices, such as
  - thin film diodes and transistors for displays,
  - thin film transistors for active connectors in 3-dimensional ICs,
  - solar cells;
- microcircuit transducers, such as

  - pressure sensors,
  - strain gauges,
  - vapor sensors,
  - mechanical components.

Poly-Si will have applications in semiconductor devices far into the future because it plays a major role in the fabrication of all manner of devices:

- MOS,
- BiCMOS,
- transducers,
- dielectric isolation,
- 3-dimensional ICs,
- CMOS,
- bipolar,
- displays,
- solar cells,
- thin film devices.

The challenges for LPCVD are

- native oxide removal (where required),
- grain structure and doping control,
- enhanced conductivity,
- integrated conductivity,
- integrated multilayer processing,
- larger diameter (250-300 mm) wafers.

Poly-Si will, indeed, be a most important material for semiconductor devices well into the 21st century.

Chapter 2

Optical models for polycrystalline silicon

Structural properties of polysilicon have been studied by many authors. The temperature and pressure dependence of the mode of growth [Mea87], structure, texture, and stability [Kam78], layer properties as a function of the deposition temperature [Kam80, Ibo93], are some of the important topics. Spectroscopic ellipsometry has proven to be very effective for the characterization of thin surface layers because it is fast, sensitive, precise, non-destructive, and can be used for an *in situ* measurement [An91, Col93, Leh98a].

Polysilicon is a material that has been studied intensively also by spectroscopic ellipsometry. As ellipsometry is usually limited rather by the interpretation of the experimental data than by experimental sensitivity, errors arising from the surface roughness are ones of the main problems of spectroscopic measurements [Fen69, Bru72, Asp79]. A new approach to obtain more information on the surface roughness is the comparison of the ellipsometric results with that obtained by atomic force microscopy (AFM) [Fan96, Flu96b, Pet98a].

One approach of determining the properties of polysilicon is to investigate its dielectric function in terms of the line-shapes and fine structures in the vicinity of the critical points of the inter-band transitions. Changes in the dielectric function can be related among others to heavy doping [Asp84], surface roughness or grain boundary effects [Log89, Log88].

To measure the layer thickness, surface roughness or microstructure of polysilicon using ellipsometry, *apriori* knowledge of the thin film optical functions, or a technique to calculate these values, is needed. Optical properties of polycrystalline silicon vary considerably depending on its microstructure. To circumvent the influence of microstructure, the B-EMA (see Section 1.1.3) is used to calculate the dielectric function of the layer using a mixture of materials having dielectric functions determined independently [Asp82]. This method allows to characterize multi-layer structures [Fri89, Loh92, Van89], and to obtain all layer thicknesses and compositions from a single measurement [Ved85, Xio90]. Even layer inhomogeneity can be taken into account [Asi93, Loh93, Fri92a].

Historically, LPCVD deposited polysilicon layers have been modeled using the B-EMA by describing them as a mixture of single-crystalline silicon, LPCVD deposited amorphous silicon and voids [Bag81, Sny92, Flu96a]. In contrast, Jellison et al. have

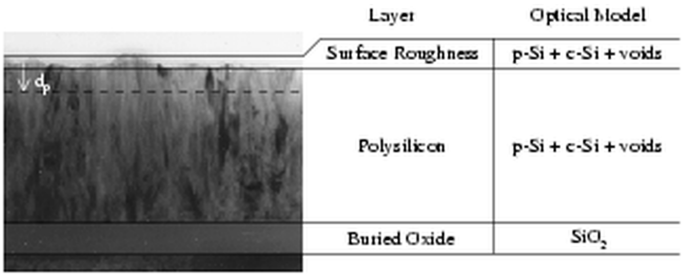

Figure 2.1. TEM picture of a polysilicon sample deposited at 620°C having a polysilicon layer thickness of 520 nm and a buried oxide thickness of 104 nm together with the best optical model used in the calculations. d_p denotes the optical penetration depth into single-crystalline silicon at the wavelength of 400 nm.

shown that this standard technique for simulating the optical functions of fine-grained polycrystalline silicon does not fit the ellipsometry data [Jel93]. We have justified this statement earlier showing that using fine-grain polycrystalline silicon reference data in the optical model gives better fit results and additional information on the layer structure [Pet98b].

In this chapter the structure of polysilicon layers with different layer thicknesses prepared at different deposition temperatures are characterized. The microstructural information obtained from the B-EMA are correlated with the layer thickness and the deposition temperature.

2.1 Experimental details

Single crystal, (111) oriented, 15-20 Ωcm, p-type silicon wafers with ≈100 nm thermal oxide were used as substrates for polysilicon deposition. Polysilicon layers were prepared using LPCVD at a pressure of 0.27 mbar and a gas flow of 100 sccm. The deposition temperatures were 600°C, 620°C, and 640°C. Samples were also prepared at a pressure of 0.33 mbar, 50 sccm gas flow at temperatures of 560°C and 580°C. This process results in a layer structure shown in Fig. 2.1. The dark grey region at the bottom of the picture is a 100 nm buried silicon dioxide layer on the single-crystalline substrate. On this oxide layer polysilicon was deposited using different deposition temperatures and deposition times to investigate material properties as functions of layer structure and layer thickness. The polysilicon layers have surface roughness of a wide range, depending on the deposition conditions. A significant surface roughness can be observed also on the polysilicon layer shown in Fig. 2.1 deposited at 620°C. Root mean square (RMS) roughness of the samples investigated in this study have values over the range of 4 nm to 20 nm. The structure can be described with a multi-layer optical model representing the buried oxide, the polysilicon and the surface roughness as shown in Fig. 2.1.

SE measurements were carried out over the spectral range of 250 nm to 840 nm in 5 nm steps using a SOPRA ES4G spectroscopic ellipsometer choosing an angle of incidence of 75°. The precise value of the angle of incidence was measured separately, using a SiO_2 sample, and was not used in the fitting procedure.

Surface roughness, layer thickness and density deficit measured by SE was cross-checked by AFM, transmission electron microscopy (TEM) and Rutherford backscattering spectrometry (RBS), respectively. The analyzing beam was a 1.5 MeV ^{4}He$^+$. The detector was placed to detect ions scattered through Θ=165°. To evaluate the spectra, we used the RBX code written by Kótai [Kót94].

2.2 Optical models

The dielectric function of the polysilicon layer can be calculated using effective medium theory (Section 1.1.3), if the polysilicon layer can be considered as a microscopically heterogeneous but macroscopically homogeneous material which consists of a random mixture of separate phases. Furthermore, the phases have to be large enough, to preserve their individual dielectric function but smaller than the wavelength of the measurement light. The relative compositions (volume fractions) of the separate regions are the obvious parameters describing such a material, but the shape distributions are also important. As shown in Section 1.1.3, shape distribution effects are important when the constituent dielectric functions are widely different, while composition is important if they are similar. In our case the composition is more important, because the constituent dielectric functions (single-crystalline silicon, amorphous silicon and fine-grained polycrystalline silicon) are not widely different. The dielectric function of void, which will also be used in the optical models, is more different but the volume fraction of this component is always very low.

Then the dielectric function $\overline{\epsilon}$ of the polysilicon layer can be expressed as

$$\frac{\overline{\epsilon}-\overline{\epsilon}_h}{\overline{\epsilon}+y\overline{\epsilon}_h} = f_a\frac{\overline{\epsilon}_a-\overline{\epsilon}_h}{\overline{\epsilon}_a+y\overline{\epsilon}_h} + f_b\frac{\overline{\epsilon}_b-\overline{\epsilon}_h}{\overline{\epsilon}_b+y\overline{\epsilon}_h} + \cdots \ , \tag{2.1}$$

where $\overline{\epsilon}_h$ is the dielectric function of the host material, f_a and f_b are the volume fractions of the constituents ($f_a + f_b = 1$, if two components are present), $\overline{\epsilon}_a$ and $\overline{\epsilon}_b$ are the dielectric functions of components "a" and "b", and y is the screening parameter ($y = (1/l) - 1$, $0 \leq l \leq 1$). The Lorentz-Lorenz, Maxwell-Garnett (a), and Maxwell-Garnett (b) effective medium expressions for two phase mixtures are obtained with $y = 2$ and $\overline{\epsilon}_h = 1$, $\overline{\epsilon}_h = \overline{\epsilon}_a$, and $\overline{\epsilon}_h = \overline{\epsilon}_b$, respectively. The B-EMA is obtained with $y = 2$ and $\overline{\epsilon}_h = \overline{\epsilon}$. The B-EMA is proved to be the best effective medium model for the calculation of the dielectric function of polycrystalline silicon [Asp79]. The choice of $y = 2$ applies to spherical inclusions appropriate to a heterogeneous system that is macroscopically isotropic in three dimensions.

Historically, the dielectric function of LPCVD deposited polysilicon is modeled by the B-EMA using a mixture of single-crystalline silicon (c-Si [Asp85]), LPCVD amorphous silicon (a-Si [Jel93]) and voids. The c-Si and a-Si dielectric function data can be taken from the literature representing a reference for the different phases assumed in the polysilicon layer (see Section 1.1.3). These data are supplied by most of the ellipsometer manufacturers, and are widely used in effective medium calculations. Voids mean the wavelength-independent dielectric function of 1, i. e. that of vacuum, which describes density deficit. In polycrystalline silicon it can be regarded as micro-voids at the grain boundaries or other kinds of defects that decrease the density of the material. The dielectric functions of the reference data c-Si and a-Si are shown in Fig. 2.2. In the visible-near UV range the dominant contribution to

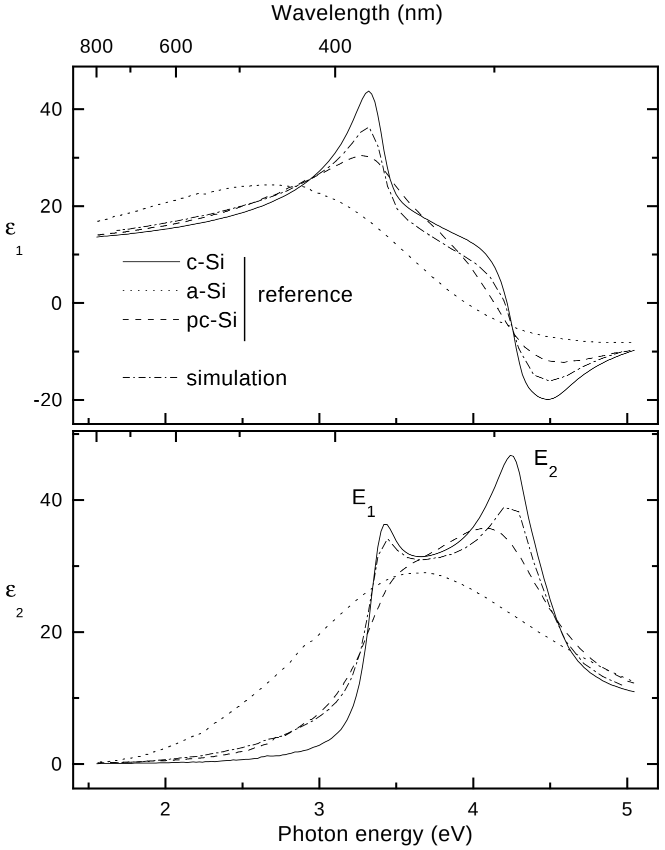

Figure 2.2. Dielectric functions used as references in the calculations (c-Si [Asp85], a-Si [Jel93], and pc-Si [Jel93] denote single-crystalline, amorphous and fine-grained polycrystalline silicon, respectively) together with the simulated spectra of the pc-Si reference data using a mixture of c-Si, a-Si, and voids (denoted as "simulation").

$\overline{\epsilon}$ comes from the electronic polarizability, which is determined by the kinds of atoms present, their bonding configurations, their density, and the presence or absence of long-range order. The amorphous silicon do not have long-range order and show only a single broad peak near 3.4 eV in the $\overline{\epsilon}_2$ spectrum.

In contrast, the crystalline silicon has long-range order and shows two sharp peaks near 3.4 eV (E_1 transition) and 4.2 eV (E_2 transition) in the $\overline{\epsilon}_2$ spectrum. Long-range order has a significant influence on both line-shape and magnitude of $\overline{\epsilon}_2$. The c-Si and a-Si materials have no microstructure, that is, they are homogeneous on the scale of 1 nm - 1 μm. The polycrystalline silicon possesses inhomogeneity in this scale.

Reference data of fine-grained polycrystalline silicon denoted by pc-Si deposited by LPCVD are also shown in Fig. 2.2. The data were taken from the literature (Ref. [Jel93]) and are supplied as a part of the reference data library of the SOPRA ES4G ellipsometer. Although the deposition condition are not detailed in Ref. [Jel93], our investigations showed that grain structure is closest to our sample deposited at 600°C at a pressure of 0.27 mbar and a gas flow of 100 sccm. These samples have a grain size typically smaller than 50 nm.

When comparing the line-shape of pc-Si to that of c-Si, the following features can be observed: there is a significant decrease in the amplitude of the E_1 and E_2

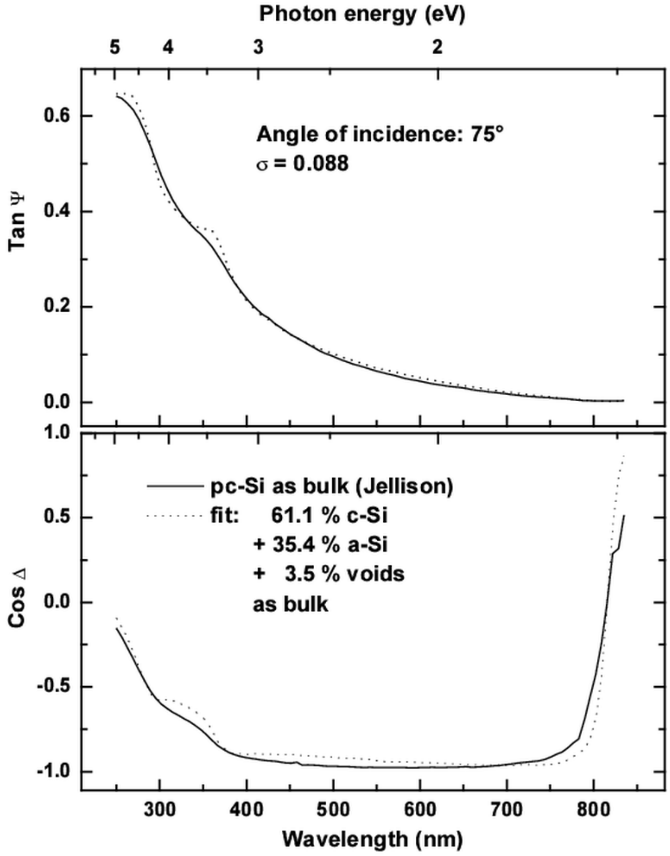

Figure 2.3. Ellipsometric spectra of a fine-grained polycrystalline silicon (pc-Si) [Jel93] together with the fitted curves. The fit was made using an optical model, where the polycrystalline silicon was simulated by the combination of c-Si, a-Si, and voids.

peaks, and there is a shifting of the E_2 peak to lower energies. The spectra in Fig. 2.2 denoted as “simulation” show the result of a simulation, where the pc-Si reference spectra, regarded as a bulk sample, were fitted using the mixture of c-Si, a-Si, and voids. The measured and fitted curves are shown in Fig. 2.3. The fit quality is bad ($\sigma = 0.088$), especially near the inter-band transition energies. The LRA resulted in a mixture of 61.1% c-Si, 35.4% a-Si, and 3.5% voids. The low energy tail in Fig. 2.2 (below E_1) of pc-Si and the simulation agree well but there is a significant difference at E_1 and E_2. This result shows, that the fine-grained polycrystalline silicon reference data cannot be well described by the mixture of c-Si, a-Si, and voids [Jel93] widely used in the literature. A possible explanation is that the a-Si component may arise not from true amorphous inclusions but as a result of the model attempting to simulate the effect of grain boundaries in reducing the electron mean free path and broadening the peak structures. Furthermore, size effects may also play an important role, i. e. the crystalline inclusions are not large enough to preserve their own dielectric functions, or there is an increased number of grain boundaries, which cannot be described with the B-EMA mixture of “c-Si + a-Si + voids”.

The microscopic roughness can be modeled with a density deficient over-layer. In their article Aspnes, Theeten and Hottier [Asp79] deal with effective medium models of microscopic surface roughness for CVD deposited amorphous silicon. They investigated different optical models with increasing complexity, in order to find the best model for the description of the surface roughness and the native surface oxide. The authors found that "a single SiO_2 layer on an a-Si substrate does not provide a good fit even with an unrealistically large oxide thickness". The reason was that – according to the fitted curves – "the thickness variable is used to adjust the phase, Δ, of the model calculation to give reasonably good approximation to the measured phase spectrum, but the model amplitude spectrum $\tan\Psi = |\rho|$ cannot be brought into agreement with the measured amplitude spectrum because the dielectric function of SiO_2 is too low". They conclude that "the fact that in every case models with an effective medium over-layer fit the data significantly better than equivalent models with an SiO_2 over-layer shows that the major contributor to the outer-layer effective dielectric function is roughness". In the case of samples with higher surface roughness the conclusion is similar: "it is clear that better representation of the rough sample are obtained by not using SiO_2 as the outer layer".

In our case, a similar series of model calculations were made in order of increasingly better fit as shown in Table 2.1. Model 1 takes into account a surface oxide layer with no roughness. Fitting the model parameters provides a thickness of the surface oxide

Table 2.1. Best fit model parameters and their 95% confidence limits for the polysilicon sample deposited at 600°C, listed in increasing goodness of fit. σ denotes the standard deviation, i. e. the quality of the fit.

Model No.	Layer 1 (buried oxide)	Layer 2 (polysilicon)	Layer 3 (surface oxide or roughness)	Layer 4 (surface oxide)	σ (10^{-2})
1	d=118±9 nm SiO_2	d=423±5 nm pc-Si(82%) c-Si(5±6%) voids(13±1%)	d=6.2±4.9 nm SiO_2,	-	5.2
2	d=112±7 nm SiO_2	d=398±6 nm pc-Si(86%) c-Si(7±5%) voids(7±2)	d=8.5±0.8 nm pc-Si(63±2%) SiO_2(37±2%)	-	4.12
3	d=112±6 nm SiO_2	d=403±5 nm pc-Si(85%) c-Si(7±4%) voids(8±1)	d=7.7±0.7 nm pc-Si(61±2%) voids(39±2%)	-	3.55
4	d=112±0.6 SiO_2	d=399±6 nm pc-Si(85%) c-Si(7±4%) voids(8±2%)	d=9.2±1.4 nm pc-Si(77±2%) voids(23±2%)	d=3.2 nm SiO_2	3.54
5	d=112±2 SiO_2	d=404±5 nm pc-Si(83%) c-Si(8±4%) voids(9±2%)	d=7.4±0.8 nm pc-Si(60) SiO_2(-11±18%) voids(51±20)		3.52

layer of 6.2 nm with a relatively high uncertainty of 4.9 nm and σ value of 0.052. In Model 3 of Table 2.1 the surface roughness is modeled using a density deficient overlayer as suggested by Aspnes, Theeten and Hottier in [Asp79]. The surface roughness layer has a thickness of 7.7±0.7 nm and contains two components: 61±2% pc-Si and 39±2% voids. Note the low uncertainties for not only the layer thickness (±0.7), but also for the components (±2%). Model 2 shows the case when the component "voids" in Model 3 is replaced with SiO_2. σ for the latter case is much higher showing a worse fit. This means – in accordance with Ref. [Asp79] – that using component "voids" is a better choice for a second component in the effective medium layer for surface roughness. When using both voids and SiO_2 in the roughness layer beside the pc-Si component (as shown by Model 5), then although a slightly better fit is obtained than for Model 3, the volume fraction for SiO_2 results in -11 with a high uncertainty for both SiO_2 and voids. This shows that using voids is more reasonable. Model 4 in Table 2.1 uses an additional surface layer to describe the thin native oxide, which covers the hills and valleys of the surface structures. Comparison with Model 3 shows that in spite of the more complex model, the improvement of the fit quality is negligible (0.0001). The thickness of the additional thin oxide layer was fixed to a physically reasonable value of 3.2 nm. When this parameter was not fixed, the surface oxide thickness resulted in 1.8 nm with a high uncertainty of ±1.6 nm, which correlates with the void fraction of the roughness layer having an uncertainty of ±9%. This result is in good agreement with that obtained in Ref. [Asp79] showing (as mentioned above) that the major contributor to the outer-layer effective dielectric function is roughness. As a result, in the following we will use Model 3 assuming that the effect of the native oxide layer can be neglected in our case.

2.3 Model parameters vs. deposition temperature

The polysilicon-on-oxide structure can be described by three-layer optical models, as shown in Fig. 2.4. Model A is used for the amorphous silicon obtained at the deposition temperature of 560°C. Model B and C are used for polysilicon layers deposited from 600°C to 640°C. Model B shows the conventional method of modeling polysilicon layers. In this study, the dielectric function of polycrystalline silicon was described by the mixture of fine-grained polycrystalline silicon (pc-Si), c-Si, and voids (Model C in Fig. 2.4).

Figure 2.5 shows measured and calculated spectra over the entire spectral range (from 250 nm to 840 nm) for the samples deposited at 560°C, 600°C, 620°C, and 640°C. The model parameters resulted from the LRA are shown in Table 2.2. The low σ values (under 0.043), and the low confidence limits prove the suitability of the optical model. The agreement between the measured and fitted spectra in Fig. 2.5 is good over the whole spectral range.

The model components for the sample deposited at 560°C are the following: a 1.2 nm thick SiO_2 layer on the surface, a 480 nm thick amorphous silicon layer described by c-Si, a-Si, and voids, and a buried SiO_2 layer having a thickness of 112 nm. The agreement between the measured and fitted spectra is very good, which is also expressed by the low confidence limits. The thickness of the 1.2 nm surface oxide and the 480 nm polysilicon layer can be measured with a precision of ±0.2 nm and ±3

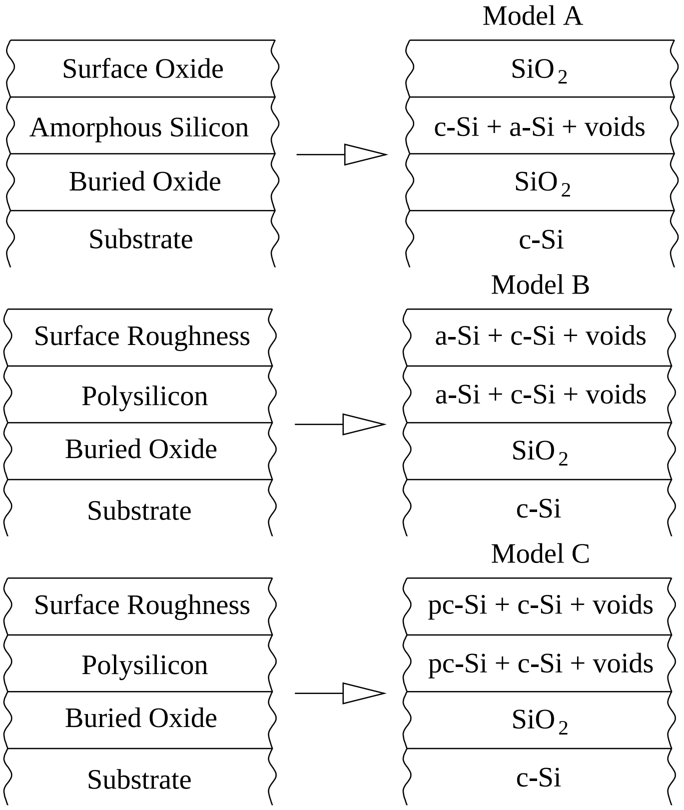

Figure 2.4. Optical models for polysilicon-on-oxide structures. Model A can be used for samples deposited at 560°C. Model B and Model C are used for deposition temperatures of 600°C - 640°C. Model B is the conventional method for describing polysilicon-on-oxide samples. In our case better results were obtained using Model C.

nm, respectively. Even the thickness of the buried oxide, which lies under the 480 nm thick polysilicon layer can be measured with a precision of ±5 nm. The buried oxide layer is visible only for the higher wavelengths near the IR end of the spectrum. This wavelength range can be easily determined from the measured data (Fig. 2.5): it is the part of the spectrum, where it oscillates. Comparing the cosΔ spectra of the samples deposited at 560°C and 620°C, it is obvious that the oscillation begins at higher wavelengths for the 560°C sample (between 550 and 600 nm), as for the 620°C sample (between 450 and 500 nm), although the layer thicknesses for the two samples are very similar (480 nm and 511 nm). This difference can be attributed to the different penetration depth in the amorphous silicon and polysilicon. If one takes three times the optical penetration depth values of Table 1.2 (page 25) as information depth obtained for LPCVD deposited amorphous silicon (a-Si) at 550 nm (3×118 nm = 354 nm) and 600 nm (3×222 nm = 666 nm), then the layer thickness of 480 nm obtained for the amorphous polysilicon sample is really between these values. The fitted parameters of the optical model show quantitatively that this layer can be described by a mixture of 2.2% c-Si, 97.8% a-Si, and 0.09% voids, i. e. is almost totally amorphous. The void fraction being almost zero shows that the density of our amorphous layer is very much like that of the a-Si reference data.

The model for samples deposited at 600°C or above consists of three layers: a density deficient over-layer describing the surface roughness, a polysilicon layer, and a

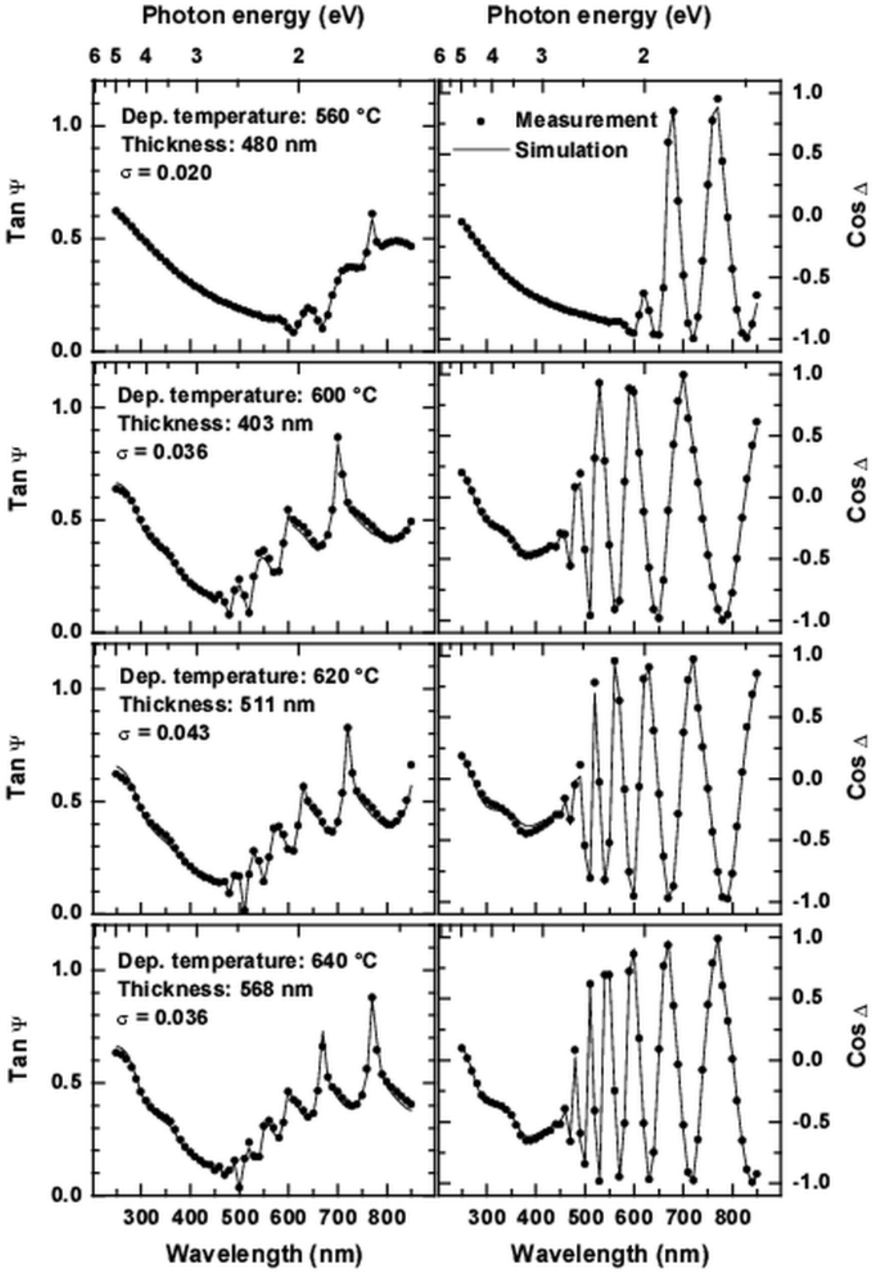

Figure 2.5. Measured and calculated spectra over the entire spectral range (from 250 nm to 840 nm) for the samples deposited at 560°C, 600°C, 620°C, and 640°C. The best fit model parameters are shown in Table 2.2.

buried oxide layer. In contrast to the conventional method of using single-crystalline silicon, LPCVD amorphous silicon, and voids in the B-EMA calculations, in this work the reference data of the fine-grained polycrystalline silicon was included in the optical model, as shown in Fig. 2.4 (Model C). The fitted curves in Fig. 2.5 with the low σ values show the suitability of this model. Fig. 2.6 shows a comparison of σ values obtained with our model (Model C) and the conventionally used model (Model B). The σ values for Model B are twice as much as in case of Model C for all deposition temperatures. This results shows, that in this range of deposition temperatures (from

Table 2.2. Best fit model parameters used for the samples deposited at 560°C, 600°C, 620°C, and 640°C. The measured and simulated spectra are shown in Fig. 2.5.

T (°C)	σ (10^{-2})	Oxide Thickness (nm)	Polysilicon layer Thickness (nm)	Polysilicon layer Composition (%)	Roughness layer Thickness (nm)	Roughness layer Composition (%)
560	2.0	112±5	480±3	c-Si(2.2) a-Si(97.8±1.3) voids(0.09±0.9)	1.2±0.2	SiO_2
600	3.6	112±6	403±5	c-Si(8±4) pc-Si(84) voids(8±1)	7.7±0.7	pc-Si(61±2) voids(39±2)
620	4.3	104±7	511±3	c-Si(23±5) pc-Si(71) voids(6±1)	10.8±0.6	pc-Si(67±2) voids(33±2)
640	3.6	104±5	568±5	c-Si(35±4) pc-Si(57) voids(8±1)	8.9±1.2	c-Si(19) pc-Si(54±3) voids(27±3)

600°C to 640°C) the fine-grained structure of the samples cannot be well modeled using the B-EMA composition of c-Si, a-Si, and voids.

In Figure 2.5 the quality of the fit for the samples deposited at 600°C and above is somewhat worse than that deposited at 560°C (σ=0.036 for 600°C, while σ=0.020 for 560°C). The reason for this difference is that the polysilicon layer deposited at 600°C can be described with a more complex model than that deposited at 560°C. In the latter case the layer is almost totally amorphous. Its optical model contains only two components: a-Si and c-Si. The fact that the volume fraction of a-Si is almost 100% shows that the dielectric function of this layer is very close to that of the reference function of a-Si measured by Jellison et al. [Jel93]. The optical models used for the samples deposited at 600°C and above have to describe a material which is microscopically heterogeneous. The second reason for the worse fit is that for deposition temperatures of 600°C and above the polysilicon layer has a significant surface roughness (in the range from 5 nm to 20 nm), while the RMS roughness of the sample deposited at 560°C was measured by AFM to be 0.09 nm, which is at the limit of the sensitivity of AFM. The best optical model for the sample deposited at 600°C contains pc-Si, and voids for the top layer modeling the surface roughness, and c-Si, pc-Si, and voids for the polysilicon layer (see Table 2.2). For layers deposited at 600°C and 620°C the roughness layers contain only the components pc-Si and voids, because when using also c-Si in this layer, the LRA results 0 for its volume fraction. The 95% confidence limits of the model parameters have reasonably low values also for the deposition temperatures of 620°C and 640°C.

Figure 2.7 shows the pc-Si and c-Si fractions of the thickest polysilicon layers as a function of the deposition temperature. At 560°C the layer is almost totally

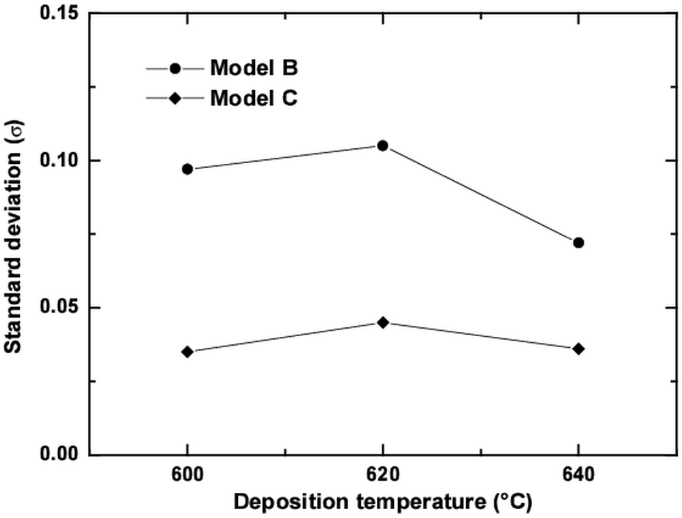

Figure 2.6. Standard deviation (σ) values showing the fit quality for the samples deposited at 600°C, 620°C, and 640°C using Model B and Model C.

amorphous having 2% c-Si. The question mark shows that 580°C is a transition temperature, at which our model could not be used. There was no reasonable fit result obtained for the sample deposited at 580°C (σ was 0.313 using Model "C"). There is a linear increase in the c-Si fraction with increasing temperature from 600°C to 640°C with a simultaneous decrease of the pc-Si fraction over the same range. It shows that the structure of the polysilicon layer deposited at lower temperature is closer to the fine-grained structure of the pc-Si reference data. The sharp decrease of the pc-Si fraction with increasing deposition temperature can be attributed to the changing structure. It has been shown by other authors that the pc-Si reference data can be well applied for the modeling of different porous silicon structures [Fri98, Loh98, Bár94]. The similarity of porous silicon and polysilicon is that both have small regions of single-crystalline silicon embedded in voids (porous silicon) or in an amorphous matrix (polysilicon). pc-Si can be used in both cases because it well describes the effect of the phase boundaries of small inclusions of single-crystalline regions on the dielectric function. The systematic decrease of the pc-Si fraction in the polysilicon layer for increasing deposition temperature can be attributed to the smaller amount of grain boundaries, i. e. to an increase of grain sizes.

For samples deposited at 600°C, 620°C, and 640°C the optical models can be improved by taking into account an additional thin transition layer between the buried oxide and the polysilicon layer describing the initial, nucleation phase of layer growth. The parameters of this four-layer model are shown in Table 2.3 as the results of LRA.

The significant improvement of the fit quality is shown in the third column of the table ($\Delta\sigma$). The thickness of the transition layer is between 27 nm and 30 nm for all samples having 29-30% voids and 64-71% pc-Si. This result is obtained even if the initial parameters of the fitting procedure are set far from these values, showing that this is not a local minimum in the fitting procedure, and proves the existence of this thin transition layer. Furthermore, it shows, that the structure of this transition layer, which represents the initial phase of growth, is very similar at different deposition

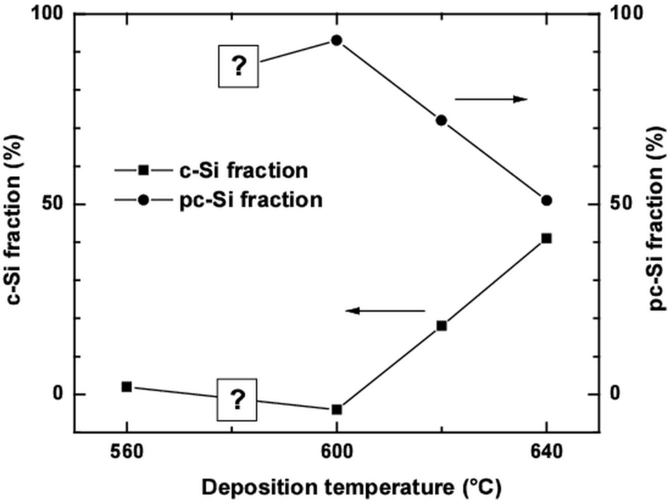

Figure 2.7. c-Si and pc-Si fractions in the thickest polysilicon layers as functions of the deposition temperature. The question mark shows that polysilicon deposited at 580°C could not be modeled.

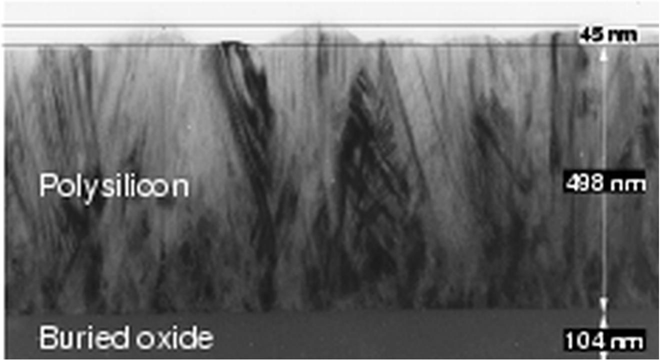

Figure 2.8. TEM picture of a polysilicon sample deposited at 620°C.

temperatures. Note that although there are a lot of fit parameters (there are ten parameters: four layer thicknesses and the fraction of two components for all the three layers $[4 + 3 \times 2]$) the confidence limits are reasonably low, showing that there are no cross-correlations between the model parameters.

Comparison of the layer thicknesses obtained by SE, TEM, and AFM is shown in Table 2.4. In the case of TEM (see Fig. 2.8), the measured thickness of the polysilicon layer was 498±8 nm, with a surface roughness of 45±15 nm (peak to peak). The thickness of the polysilicon layer is defined as a thickness measured from the boundary between the polysilicon layer and the buried oxide layer to the boundary between the polysilicon layer and the roughness layer. In the case of TEM the boundary between the polysilicon layer and the roughness layer cannot be determined precisely. Taking into account this uncertainty, the SE and TEM values are in reasonable agreement. For the thickness of the buried oxide, where the boundaries between the oxide and

Table 2.3. Parameters of the four-layer model for polysilicon with a transition layer; “VFR” denotes the volume fractions of the components.

T (°C)	σ (10^{-2})	$\Delta\sigma$ (10^{-2})	Oxide Thickness (nm)	Tr. layer Thickness VFR (%)	PolySi layer Thickness VFR (%)	Rough. layer Thickness VFR (%)
600	2.9	-0.6	113 ± 9.6	27±3.0 nm pc-Si(71 ± 12) voids(29 ± 12)	380±7.2 nm pc-Si(68 ± 10) c-Si(25 ± 9) voids(7 ± 1)	8.4±1 nm pc-Si(62 ± 2) voids(38 ± 2)
620	3.4	-1.1	108 ± 11	29.5 ± 4.2 nm pc-Si(70 ± 12) voids(30 ± 12)	501 ± 5.3 nm pc-Si(58 ± 10) c-Si(34 ± 9 voids(8 ± 1)	8.4 ± 1 nm pc-Si(65 ± 2) voids(35 ± 2)
640	3.1	-0.5	97 ± 10	28.2 ± 6.8 nm pc-Si(64 ± 13) voids(36 ± 13)	552 ± 8.6 nm pc-Si(43 ± 8) c-Si(50 ± 7) voids(7 ± 1)	9.0 ± 1 nm pc-Si(49 ± 12) c-Si(23 ± 10) voids(28 ± 2)

Table 2.4. Comparison of the thicknesses for sample deposited at 620°C obtained by SE, TEM (Fig. 2.8), and AFM.

Layer	SE	TEM	AFM
Buried oxide	104.6 ± 6.9 nm	104 ± 2 nm	-
Polysilicon	511.0 ± 2.7 nm	498 ± 8 nm	-
Roughness	10.8 ± 0.6 nm$^{(*)}$	45 ± 15 nm$^{(**)}$	10.6 nm$^{(***)}$

$^{(*)}$ Thickness of the top layer of the optical model
$^{(**)}$ Peak to peak
$^{(***)}$ RMS roughness (10×10 μm^2 window)

the substrate and between the oxide and the polysilicon are well defined, there is a very good agreement between SE and TEM. The surface roughness measured by SE cannot be compared directly to the peak to peak roughness measured by TEM. The RMS roughness measured by AFM in the 10×10 μm^2 window agree well with the SE result. It is not proven yet, whether the thickness of the roughness layer obtained by SE is directly correlated with the RMS roughness or with other characteristics of the surface. A more detailed study of surface roughness measured by SE and AFM is discussed in Chapter 3.

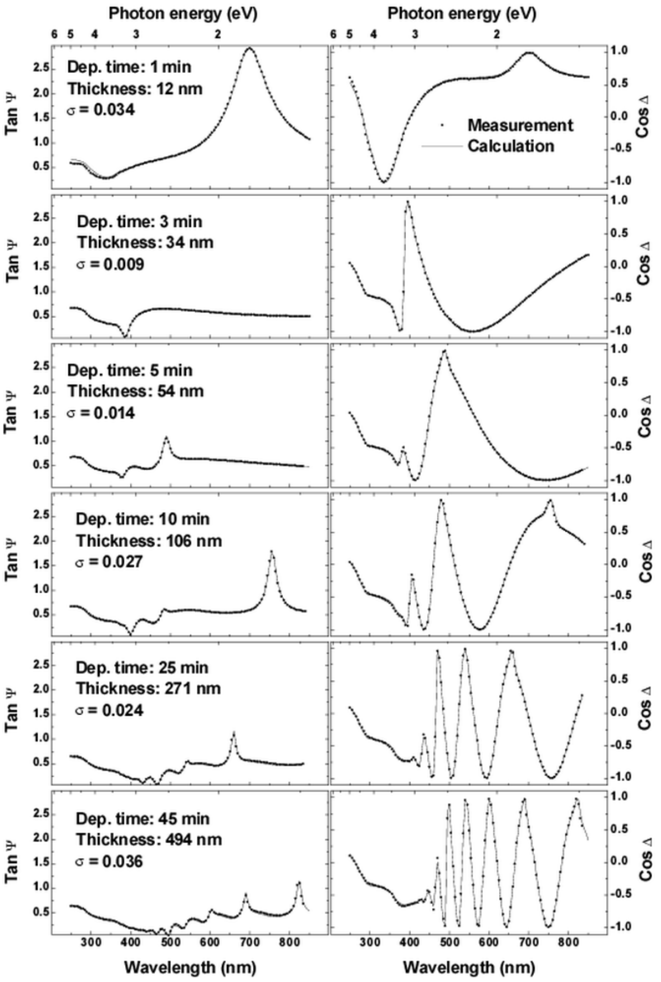

Figure 2.9. Measured and fitted ellipsometry spectra for polysilicon samples deposited at 640°C. The fitted model parameters are shown in Table 2.5

2.4 Model parameters vs. layer thickness

Figure 2.9 shows the measured and fitted ellipsometry spectra of polysilicon samples deposited at 640°C for different deposition times. The layer thickness of the samples ranges from 12 nm to 494 nm. The σ value is lower than 0.036 for all the samples, which means a very good fit quality. The interference oscillations of increasing frequency with increasing layer thickness are clearly seen on the cosΔ plot.

The parameters of the optical model obtained by the LRA for the samples deposited at 640°C are shown in Table 2.5. The optical model is the same as used in the previous section (Model C in Fig. 2.4). The microscopic roughness is modeled with a homogeneous density deficient over-layer, the polysilicon layer with a homogeneous layer having a dielectric function calculated by the combination of c-Si, pc-Si, and voids. The surface roughness changes from 3 nm to 8 nm, the thickness of the polysilicon layer from 12 nm to 494 nm, and the buried oxide layer is 115 nm with a confidence of ±3 nm. Note that the uncertainty of the measurement of the buried oxide thickness is typically ±3 nm or better even below a 494 nm polysilicon layer. Because the buried oxide was prepared in the same batch process for all samples in

Table 2.5. Optical model parameters used for the samples deposited at 640°C. The measured and fitted spectra are shown in Fig. 2.9

Dep. Time (min)	σ (10^{-2})	Oxide Thickness (nm)	Polysilicon layer Thickness (nm)	Polysilicon layer Composition (%)	Roughness layer Thickness (nm)	Roughness layer Composition (%)
1	3.4	115±1	12±0.3	pc-Si(40±1) a-Si(9±2) voids(51±0.5)		
3	0.9	113±1	34±0.3	c-Si(53±2) pc-Si(43) voids(4±0.3)	3.0±0.3	c-Si(38±7) pc-Si(25) voids(37±3)
5	1.4	116±2	54±0.6	c-Si(61±2) pc-Si(37) voids(2±0.7)	4.0±0.5	c-Si(36±9) pc-Si(35) voids(29±3)
10	2.7	114±9	106±1.0	c-Si(64±3) pc-Si(36) voids(0±1.0)	5.6±0.8	c-Si(40±10) pc-Si(35) voids(25±3)
25	2.4	114±3	271±2.0	c-Si(50±2) pc-Si(46) voids(4±1.0)	6.4±0.6	c-Si(26±8) pc-Si(45) voids(29±2)
45	3.6	114±3	494±4.0	c-Si(41±3) pc-Si(51) voids(8±1.0)	8.0±0.9	c-Si(22±9) pc-Si(49) voids(29±2)

Table 2.5, its thickness is expected to be very similar. Indeed, the difference between the thickness values for the buried oxide layers is less than 3 nm. This is a good verification of the reliability of the optical model. Furthermore, the reasonably low confidence limits show that the precision of the determination of the model parameters is good.

Figure 2.10 shows the surface roughness and the volume fractions of voids in the roughness layer and in the polysilicon layer as a function of the thickness of the polysilicon layers deposited at 600°C, 620°C, and 640°C. Model C of Fig. 2.4 was used for all samples in the calculation. The model parameters of the sample deposited at 640°C are shown in Table 2.5. The error bars on Fig. 2.10 represent the 95% confidence limits. For the thinnest layers, where the polysilicon was modeled with only one layer, this layer is regarded as the roughness layer.

The curves describing the thickness and the void fraction of the surface roughness layer can be divided into two different regions. The region below a layer thickness of ≈40 nm is characterized by a high surface roughness and high void fraction. Both of them decreases rapidly with increasing layer thickness up to a layer thickness of 40 nm. The high void fraction is consistent with previous result, which showed the existence of a transition layer (Section 2.3, Table 2.3).

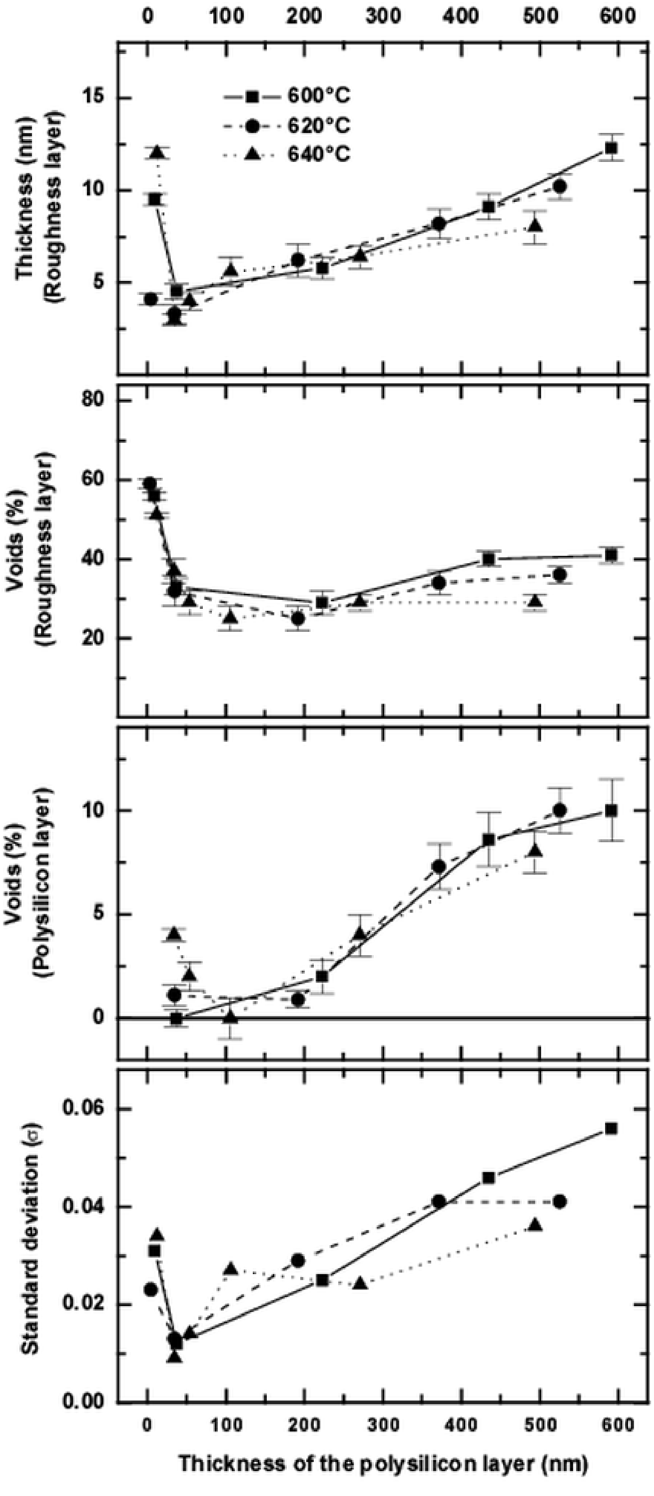

Figure 2.10. Model parameters as functions of the layer thickness for polysilicon samples deposited at different temperatures.

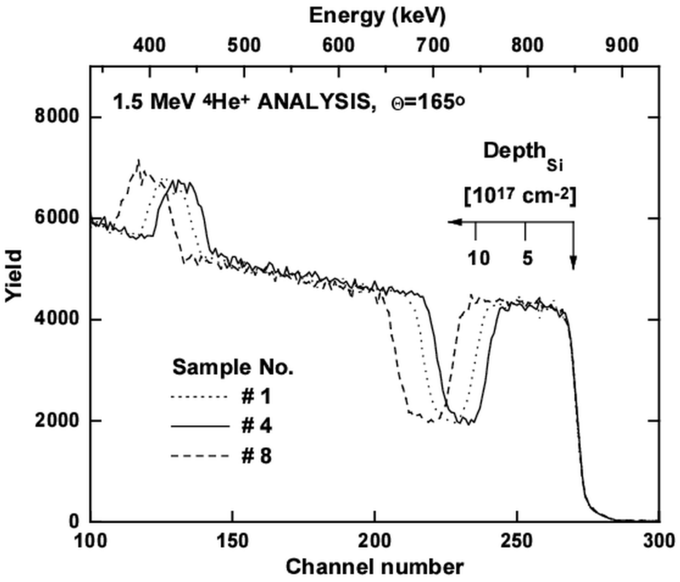

Figure 2.11. RBS spectrum of three different polysilicon samples. Details of the deposition conditions are given in Table 2.6.

The increase of the thickness of the roughness layer with increasing thickness of the polysilicon layer above a polysilicon layer thickness of 40 nm can be explained by the V-shaped grains having larger dimensions on the surface of thicker layers. The void fraction of the roughness layer slightly increases at higher thicknesses (>200 nm) which shows that there is a little change in the shape of the surface protrusions having less volume fraction of material in the effective layer describing the surface roughness.

It has to be emphasized that this layer thickness cannot be related directly to the RMS roughness, to the R_a roughness or to other single values, because surface roughness cannot be unambiguously characterized with one single number. There is a good correlation between the RMS roughness of polysilicon measured by AFM and the thickness of the surface roughness layer of the ellipsometric model, but the position of the correlation line depends on other parameters like tip shape or the scan window size of AFM, and the used optical model or inhomogeneities in the case of SE [Pet98a].

The void fraction in the polysilicon layer has a thickness dependence similar to that of the roughness layer. It has a minimum close to 100 nm. For layers thicker than 100 nm it increases, and reaches 10% at a layer thickness of 600 nm. This void fraction reflects the increasing density deficit with increasing thickness for layers thicker than 100 nm.

For cross-checking the SE results, the void fraction of polysilicon layers (i. e. the density deficit) was determined also by RBS (see Section 4.1.1). Fig. 2.11 shows the RBS spectra of three selected polysilicon samples. In each spectrum the region between the Si surface edge (channel #271) and the upper edge of the valley (channel #240, #236, and #228 in Fig. 2.11 for samples 4, 1, and 8, respectively) corresponds to the top polysilicon layer. The valley corresponds to silicon in the buried oxide, where the density of silicon decreases due to the presence of oxygen atoms. (The peaks below channel #140 correspond to the oxygen atoms.) The energy difference between helium ions scattered from the surface of the polysilicon layer and those scattered from the polysilicon-buried silicon dioxide interface is proportional to the number of silicon atoms in the polysilicon layer per square centimeter. The density (cm^{-3}) of the layer is easy to determine by combination of RBS and ellipsometry as shown in the case of buried, ion synthesized nitride [Khá88], since RBS gives the areal density (cm^{-2}) and ellipsometry provides the layer thickness.

Having calculated the density of the top polysilicon layer (ρ_{poly} in cm^{-3}), the void fraction was determined as $(\rho_{Si} - \rho_{poly})/\rho_{Si}$, where ρ_{Si} is the density of the single-crystalline silicon. ρ_{poly} was calculated using the layer thickness obtained by SE. Void fraction values measured by SE and RBS are shown in Table 2.6. Fig. 2.12 shows that there is a good correlation between the SE and RBS results.

Table 2.6. Comparison of the void fraction of polysilicon samples deposited varying the deposition temperature and the deposition time, extracted from SE measurements and from the combination of SE and RBS measurements.

Sample No.	Deposition time (min)	Deposition Temperature (°C)	Void fraction SE (%)	Void fraction RBS & SE (%)
1	42	600	2±0.8	5.8±2.5
2	75	600	8.6±1.3	10.4±1.9
3	100	600	10±1.5	11.4±1.8
4	25	620	0.9±0.6	3.2±3.1
5	45	620	7.3±1.1	8.6±1.9
6	60	620	10±1.1	11.0±1.7
7	10	640	0±1.0	1.8±2.9
8	25	640	4±1.0	5.6±2.2
9	45	640	8±1.0	9.4±1.6

The σ values in Fig. 2.10 have a minimum at ≈40 nm, which shows that our model fit best to the structure of the initial phase of the deposition. Above 40 nm σ slightly increases having the highest value of 0.056 for the thickest polysilicon layer deposited at 600°C.

The dependence of the model parameters on the deposition temperature has the following feature: the void fraction in the roughness layer is higher for the lower deposition temperatures in case of the thickest samples; similarly, there is a higher surface roughness for the lower deposition temperatures above a layer thickness of ≈250 nm. It is also clear that in order to be able to compare the effect of the deposition temperature on the surface properties, layers with the same thickness have to be used to separate the influence of the layer thickness from that of the deposition temperature.

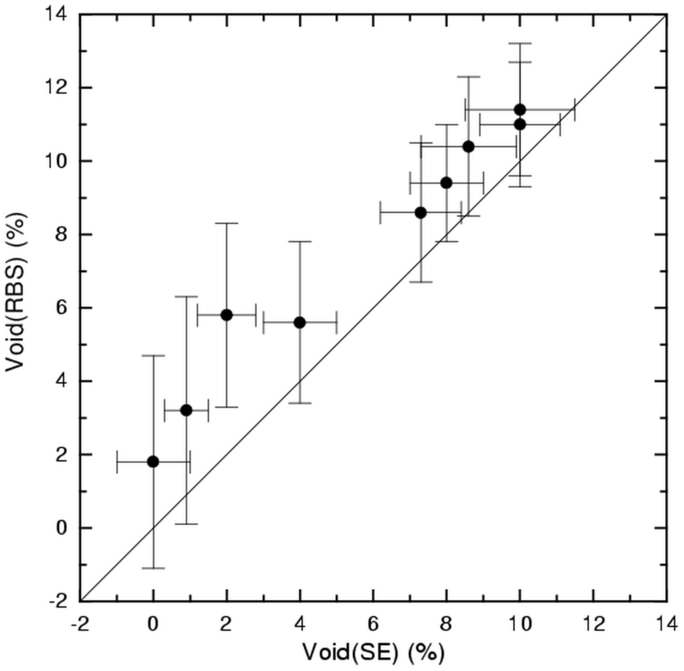

Figure 2.12. Correlation of the void fraction values measured by SE and RBS for polysilicon samples shown in Table 2.6.

Chapter 3

Microscopic Surface Roughness

Ellipsometry is usually limited by the interpretation of the experimental data rather than by experimental sensitivity. Errors arising from the surface roughness are one of the main problems of spectroscopic measurements [Fen69, Bru72]. The effect of the roughness on the measured dielectric function has been studied intensively [Log88, Bou92]. For an accurate determination of bulk dielectric functions surface roughness has to be taken into account. Effective medium models, which represent the rough surface equivalent to a homogeneous film with a given thickness for the reflection of the light, provide the possibility of obtaining quantitative information about the surface [Asp79]. As viewed in terms of ray optics, the reflection of light from a rough surface would be analyzed by considering light reflected from both the sides and the tops of the ridges. Then the multiply reflected beams would be combined to determine the total reflected light beam. However, if the dimensions of the roughness are less than the wavelength of the visible light, ray optics do not apply, and the light "sees" an average effective refractive index for the rough surface.

AFM was used by several research groups to confirm surface roughness values determined by SE [Spa94, Liu95]. Liu et al. [Liu94] studied the Si/SiO$_2$ interface using AFM and SE. The authors compared the results of the two fundamentally different measurement methods, with AFM being a local measurement and ellipsometry averaging the optical response of a relatively huge area. It is claimed that the root mean square (RMS) roughness is equal to 50% of the peak to valley height, which is in good agreement with the SE results being about 2 times as large, however, such a simplification is valid only in special cases. Other researchers [Suz94] regard it a "reasonable agreement", when RMS roughness obtained by AFM and by the B-EMA using SE have nearly the same value. A quantitative relationship between the roughness measured by AFM and the ellipsometric parameters has been reported by Fang et al. [Fan96]. The roughness was varied by exposing the silicon surface to various chemical treatments and oxidation/strip sequences. Differences in Δ were observed for surfaces with the same RMS roughness, but different roughness spectral densities. The larger the high-frequency components, the larger the effect on Δ, since if the spatial wavelength of the roughness is greater than the ellipsometric wavelength, the B-EMA fails and there is little effect on the ellipsometric parameters. This investigation shows that RMS roughness of AFM without roughness spectral density information does not determine the ellipsometry parameters unambiguously.

In this chapter, the effective medium approximation was applied to the ellipsometric measurement data to calculate surface roughness. Consequently, not the ellipsometric parameters, but rather the thickness of the top layer of the SE model describing the surface roughness was compared to the RMS and R_a roughness measured by AFM.

3.1 Experimental details

3.1.1 Brief description of atomic force microscopy

Scanning probe microscopy and scanning probe microscopes (SPMs) are the cutting edge in today's microscope field. SPMs come from the scanning tunneling microscope (STM) built first in 1982. The STM can only be used for conducting samples. The first AFM microscope, which can be used also for measuring insulators, was built four years later. The technology used in SPMs is so new that many of its terms are still being named by the industry.

By way of comparison with other forms of microscopy, SPM's strengths rapidly become apparent. SPM offers advantages over many types of microscopy, yet is unsuited for certain types of work; therefore, the selection of scanning probe microscopy is not always recommended. (For example, optical microscopes still reign supreme for low-magnification, wide-field work.) Microscopes may be compared using the following criteria: resolution, depth of field, sample preparation.

The term "magnification" is somewhat ambiguous with respect to SPM. Whereas optical microscopes utilize optical components to amplify visible light, SPMs derive an image entirely from electronic means. What is seen through the eyepiece of an optical microscope is in most ways an extention of the human eye. The SPM, on the other hand, renders an image from an electro-mechanical interaction with the sample, which is then translated electronically onto a computer screen. Although SPMs may theoretically image a specimen of any size, they are practically limited by

- probe size,
- scanning speed,
- memory requirements to store electronic data,
- the maximum travel of the scanner,
- the substrate used to hold the sample.

Clearly, it would be impractical to use an SPM for obtaining wide-field, multiple images of insects – its scan size and speed make it less practical than a conventional optical microscope. However, if the task is to image atomic lattices, the SPM's advantages quickly emerge. A comparison of microscope resolutions is shown in Table 3.1.

Depth of field refers to the viewable range of object distances – the extent to which features in both foreground and background may be imaged. In optical instruments, depth of field is directly related to the numerical aperture of the objective lens and its distance from the sample. In SPM, depth of field is limited by the travel limits of the scanning tube (about 0.0053 mm), which dictates the ability of the tip to profile the features it is imaging. Depth of field is also related to tip size and geometry: if a

Table 3.1. Comparison of microscope resolutions ([nan]).

Microscope	Maximum Resolution (nm)	Comments
Optical	180	oil immersion with 1,500X objective
Acoustic	15	
Electron (TEM)	0.11	imaging carbon atoms in diamond
SPM (STM)	0.08	imaging carbon atoms in graphite

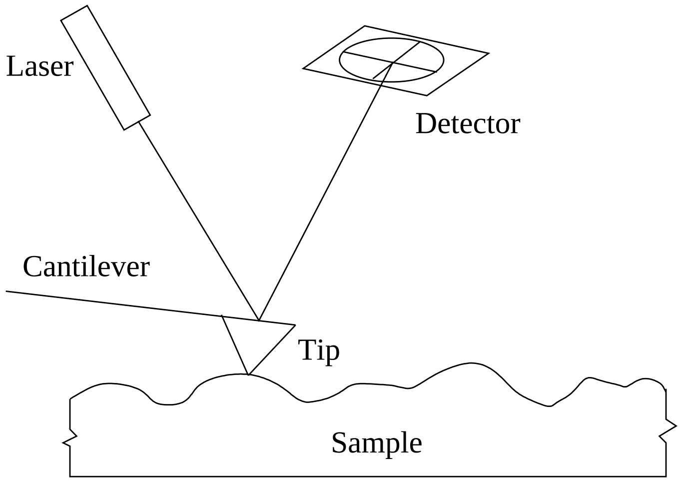

Figure 3.1. Principle of the AFM measurement.

tip is too thick to reach into a recess, it cannot image there, thus reducing depth of field. Generally, SPMs are best suited for imaging relatively flat samples.

Comparing sample preparation with other microscopes, SPMs are distinguished by their simplicity. For contact AFM and tapping mode operation, samples do not generally require any special preparation at all. SPMs utilizing STM and certain types of electric force microscopy (EFM) require that samples be conductive; however, the bulk of SPM work continues to be performed using Tapping Mode and contact AFM. Other than rigid sample mounting, most SPM requires little or no special preparation.

The term “tip” is used interchangeably by many SPM users with the term “probe” and “cantilever”, and is the element which interacts directly with the sample. Properly speaking, “tip”, “cantilever”, and “probe” mean three different things. In contact AFM, the tip – that part which directly interacts with the sample – is usually mounted on the end of a support (the cantilever) to create a unified probe. The cantilever provides a support for the tip and is deflected by pressure upon the tip. By monitoring how the cantilever is deflected, the tip’s travel over surface features is interpreted, then rendered into an electronic image.

The principle of the AFM measurement is shown in Fig. 3.1. The interaction between the sample and the tip can be defined by the deformation of the cantilever. This deformation is calculated by using a detector which measures the position of the light beam reflected from the cantilever.

Most contact AFM and Tapping Mode tips are fabricated from silicon-based materials, largely because micro-fabrication of silicon has been extensively developed in the microelectronics field. These tips are made in various lengths and thicknesses, depending upon a desired spring constant.

The quality of an SPM image is wholly dependent upon how precisely a tip-sample interaction can be monitored. Half of this interaction is dependent upon the scanner, the portion of the SPM moving the sample and/or tip. Scanners are so called because the usual path of travel consists of a raster-type, back and forth scan. There are two configurations: in the first, the probe is mounted stationary while the sample is scanned beneath it. This has the advantage of simpler construction and allows for very precise control of the tip-sample interaction. The other configuration is in which the sample is mounted stationary while the tip is scanned over it. This has the chief advantage of allowing much larger samples to be imaged. The scanners utilize piezo materials unified in a single tube; each tube consists of five or more independently operated piezo elements. Piezo materials can be made to contract and elongate proportionally to an applied voltage; whether they elongate or contract depends upon the polarity of the voltage applied.

In order to render the most accurate image possible, tip-sample interactions must be taken into account. These include

- fluid film damping,
- electrostatic forces,
- fluid surface tension,
- Van der Waals forces,
- coulombic forces.

Not only tip-sample interaction, but also tip-sample geometry affects the quality of an image. The actual “sharpness” of a tip directly influences its ability to resolve surface features. Moreover certain tip defects (e. g. double-pointed and cracked tips) produce predictable defects in images.

3.1.2 Sample preparation and measurements

Single-crystal, (111) oriented, 15-20 Ωcm p-type silicon wafers were thermally oxidized for 54 min. at 1100°C to grow approximately 100 nm of SiO_2. Polysilicon layers were prepared by chemical vapor deposition from SiH_4 using a gas flow of 50 sccm and a pressure of 0.33 mbar. The deposition temperatures were 560°C, 620°C, 660°C, and 700°C.

AFM measurements were made by a Digital Instruments NanoScope Scanning Probe Microscope in tapping mode using scan window sizes of 1×1 μm^2, 10×10 μm^2, and 50×50 μm^2. Si tips with a resonant frequency of the cantilever of 300 kHz have been used. Because the roughness values are influenced by tip, scan size, and scan conditions, the parameters of the measurements were kept identical from sample to sample. Images of 256×256 pixels were acquired at a scan rate of 3 Hz.

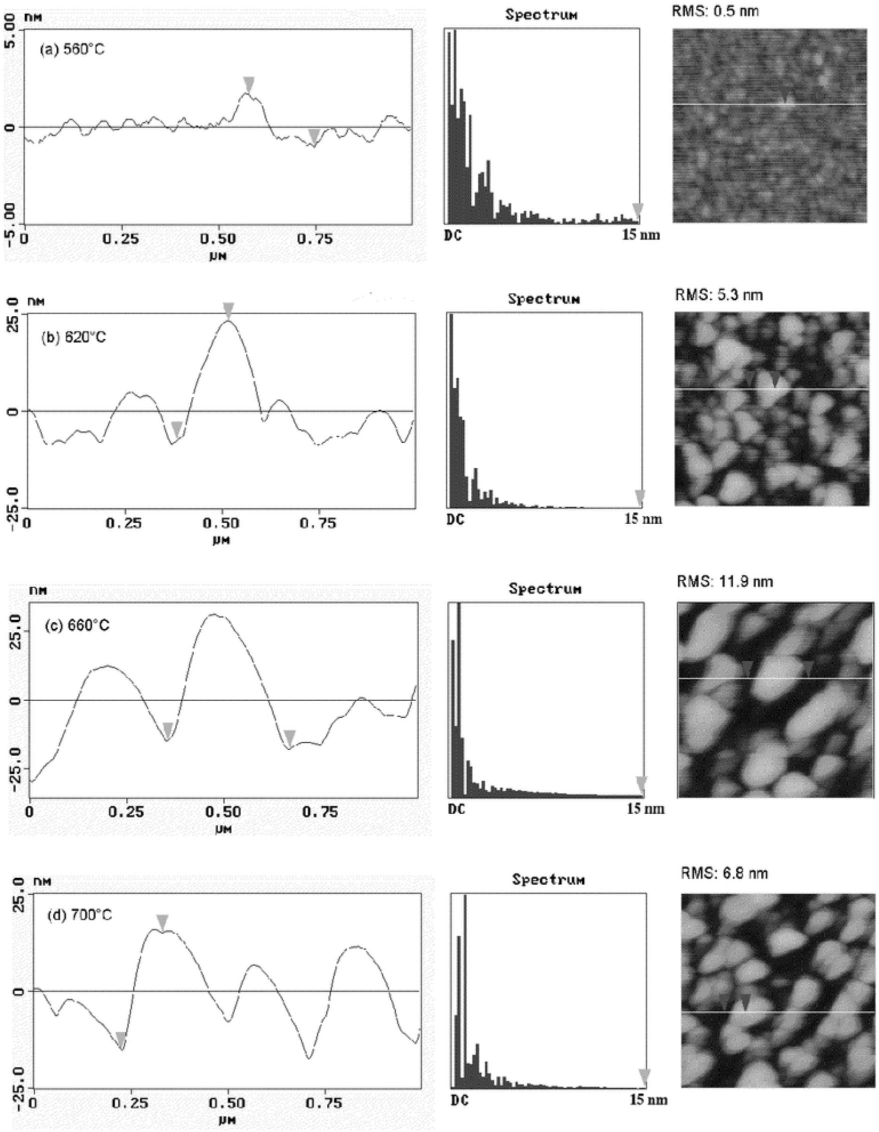

Figure 3.2. Cross-sectional AFM profiles along a reference line (left-hand side), FFT spectra (middle), and surface plots (right-hand side) for polysilicon samples deposited at 560°C (a), 620°C (b), 660°C (c), and 700°C (d) using 1×1 μm^2 scan window size.

A SOPRA ES4G rotating polarizer spectroscopic ellipsometer was used to obtain the ellipsometric angles in the spectral range of 250 nm to 800 nm in 55 spectral points with an angle of incidence set at 75°. The measured spectra were evaluated using LRA fitting the simulated spectra by varying the optical parameters of a three-layer model.

3.2 Results and discussion

3.2.1 AFM measurements

Figure 3.2 shows the cross-sectional AFM profiles (left-hand side), fast Fourier transformed (FFT) spectra (middle) and the surface topographies (right-hand side) for deposition temperatures of 560°C, 620°C, 660°C, and 700°C in a 1×1 μm^2 window.

The shape of the peaks in the cross-sectional profiles (i. e. the grains) such as the FFT spectra and the correlation length (approximately 200 nm) are similar for the different deposition temperatures.

RMS roughness values obtained using the 1×1 μm^2 scan window size were 0.5 nm, 5.3 nm, 11.9 nm, and 6.8 nm for temperatures of 560°C, 620°C, 660°C, and 700°C, respectively. R$_a$ values were also calculated defined as the absolute value of the surface relative to the center plane using

$$R_a = \frac{1}{L_x L_y} \sum_0^{L_y} \sum_0^{L_x} |f(x,y)| dx dy, \tag{3.1}$$

where $f(x,y)$ is the surface relative to the center plane and L_x and L_y are the dimensions of the surface. The R$_a$ values for deposition temperatures of 560°C, 620°C, 660°C, and 700°C were 0.3 nm, 4.2 nm, 9.6 nm, and 5.5 nm, respectively, having a parallel change with RMS roughness, but at smaller values. The maximum heights of the surface features show similar variation with deposition temperature with a maximum value of 85 nm at 660°C, and 17 nm, 44 nm, and 59 nm at 560°C, 620°C, and 700°C, respectively.

The non-monotonic change with deposition temperatures, having the largest grains at 660°C is shown by the surface plots, too. The grain sizes for deposition temperature of 620°C are the smallest, while no grains are observable at 560°C.

For surface features having curvature radii in the range of the curvature radius of the tip, the convolution of the tip geometry with the measured object cannot be neglected. The protrusions having a smaller radius of curvature than the tip will image the tip. Since samples were measured one after the other with the same tip, the same tip profile was added to all of them. Consequently, the results are comparable. Furthermore, it was obtained from AFM results measured in the 1×1 μm^2 window and also from TEM pictures, that the grains had a slope of max. 36°, which is much smaller than that of the tip (73°). The RMS roughness of blank silicon reference samples is in the range of 0.09 nm [Bir96].

3.2.2 Ellipsometry measurements

In order to extract information about the physical structure of the sample, an optical model has to be created describing the layer structure and composition (see Section 1.1.2). The measured ellipsometric spectra are compared to the calculated spectra using initial estimates of the model parameters. The values of the parameters are adjusted to minimize the difference between the measured and calculated spectra by linear regression (see equation 1.32 on page 7).

Effective medium models are used to calculate the dielectric response of a microscopically heterogeneous but macroscopically homogeneous material (Section 1.1.3). Numerous expressions have been proposed to describe the effective dielectric response $\overline{\epsilon}$ in terms of the microstructural parameters such as the Lorentz-Lorenz-, Maxwell-Garnett (a,b)-, or the B-EMA [Bru35]. The latter is used most frequently. Also in this study, since it accurately represents the aggregate structure where an inclusion may come into contact with different materials, including that of its own type.

Measured ellipsometric spectra of the polysilicon samples deposited at 620°C, 660°C, and 700°C together with the results obtained from a multi-parameter fit are

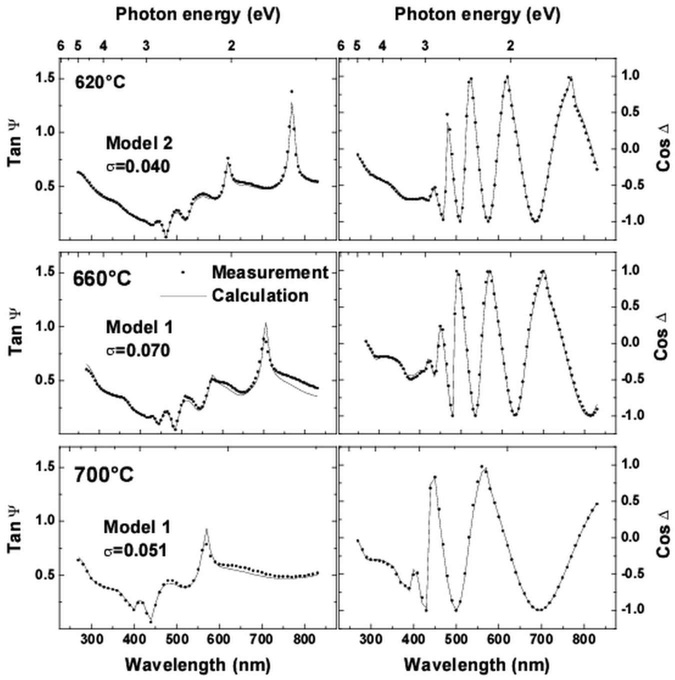

Figure 3.3. Calculated and measured spectra of polysilicon-on-oxide structures with polysilicon layers deposited at 620°C, 660°C, and 700°C. The optical models Model 1 and Model 2 are shown in Fig. 3.4.

shown in Fig. 3.3. The angle of incidence was measured separately, using a SiO_2 sample, and was not used in the fitting procedure. The standard deviation (σ) describing the fit quality of the samples deposited at 620°C, 660°C, and 700°C is 0.040, 0.070, and 0.051, respectively. The optical models for the calculations are shown in Fig. 3.4.

A three-layer optical model is used taking into account the oxide layer on the substrate, the polysilicon on the oxide and the surface roughness layer. The refractive index of polysilicon was calculated combining the refractive indices of c-Si [Asp85], a-Si [Jel93], and voids using the B-EMA (see Section 2). The surface roughness was considered as a density deficient over-layer containing the same components as the polysilicon layer: single-crystalline silicon, amorphous silicon, and voids. A detailed study of different optical models for surface roughness including native oxide has been done in Chapter 2 (page 37). For polysilicon layers deposited at lower temperatures (near 600°C – see Chapter 2) a better description of the layer structure can be obtained by using the reference data of the fine-grained polycrystalline silicon in the optical model (see Model 2). The standard deviation (σ) was calculated for each model as the measure of the fit quality. The thickness of the top layer modeling the surface roughness is 5.3 nm, 11.4 nm, and 7.1 nm for deposition temperatures of 620°C, 660°C, and 700°C, showing very good correlation with the RMS roughness of AFM being 5.3 nm, 11.9 nm, and 6.8 nm, respectively, for the 10×10 μm^2 window.

The roughness measured by AFM and SE are shown in Tables 3.2 and 3.3.

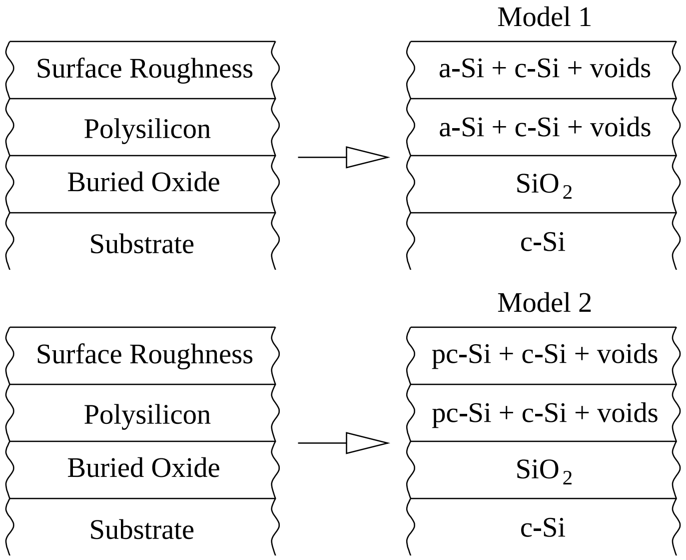

Figure 3.4. Three-layer optical models used in the calculations. The models take into account the oxide layer on the substrate, the polysilicon on the oxide and the surface roughness layer. In Model 2 the use of the reference dielectric function data of the fine-grained polysilicon [Jel93] allows a better description of the structure resulting at lower deposition temperatures (see Sections 2.3 and 2.4).

Table 3.2. Roughness measured by SE and RMS roughness measured by AFM on polysilicon samples deposited at 620°C, 660°C, and 700°C.

T_{dep}	Roughness	RMS roughness (AFM) (nm)		
	(SE)	1×1 μm^2	10×10 μm^2	50×50 μm^2
(°C)	(nm)	window	window	window
620	5.3	7.0	5.3	4.2
660	11.4	12.6	11.9	7.3
700	7.1	7.9	6.8	5.2

3.3 Comparison

Figure 3.5 shows the mean roughness (R_a) and RMS roughness measured by AFM using scan window sizes of 1×1 μm^2, 10×10 μm^2, and 50×50 μm^2 correlated with the thickness of the top layer of SE modeling the surface roughness. It is obvious that independently from the used window size for both R_a and RMS roughness, very good correlation of the roughness determined by SE and AFM were obtained. The R_a and RMS roughness plots show the same characteristics. The linearity is good in both cases for all the window sizes. The 1×1 μm^2 and 10×10 μm^2 window correlation lines run not only almost parallel, but, in the case of RMS roughness, with a slope of 1. The correlation lines of the 50×50 μm^2 window run on a lower level and it has a lower slope. Correlation data of two other as-grown samples deposited in another furnace at 640°C using the same pressure and gas flow are also shown (marked with □ and △). They fit well to the correlation lines. The roughness of a polysilicon layer deposited using the same deposition parameters as these samples but annealed at 1000°C in N_2

Table 3.3. Roughness measured by SE and R_a roughness measured by AFM on polysilicon samples deposited at 620°C, 660°C, and 700°C.

T_{dep} (°C)	Roughness (SE) (nm)	R_a (AFM) (nm) 1×1 μm^2 window	10×10 μm^2 window	50×50 μm^2 window
620	5.3	5.5	4.2	3.2
660	11.4	10.1	9.6	5.9
700	7.1	6.5	5.5	4.1

for 1 hour (marked as +, ×, and $*$) do not fit the lines. The roughness measured by SE is higher, while that measured by AFM is lower for the annealed sample than for the as grown sample. The deviation is attributed to the changed surface. Surfaces having the same RMS roughness, but different shapes of profiles, can yield different roughness values measured by SE. This means that RMS roughness is not enough to describe all surface characteristics, to which SE is sensitive. The requirement of the good correlation is the similarity of the surfaces which is characterized by the similar shapes of the grains and the similar FFT spectra as shown in Fig. 3.2.

The smaller the window, the higher the AFM roughness. The reason is that for smaller windows the resolution of the AFM measurement improves, i. e. the 256 pixel line can sample the structure of the surface in more detail. To choose the best window size, it must be considered that although smaller window sizes result in a better resolution of the profile, surface roughness is an integral value, thus one has to use a window large enough to be representative for the whole sample. Consequently, the lateral homogeneity is an important issue.

The interpretation of the roughness obtained by SE in comparison with AFM results is not unambiguous. In the study made by Liu et al. [Liu94], roughness results from AFM and SE on Si/SiO$_2$ interfaces were compared. It was stated that a parallel change of the roughness values obtained by the two methods gives credence to the ability of the spectroscopic ellipsometry measurement and modeling to follow the roughness change. The results were compared with the statement mentioned in the introduction that RMS roughness being about 50% the peak-to-valley height of the protrusions should give values that are half of the SE results. This ratio shows significant discrepancies depending on the etching and oxidation times, i. e. on the shape of the surface protrusions. As Fang et. al. [Fan96] emphasized, not only RMS roughness, but also FFT spectra determine the SE-AFM correlation.

In contrast to Liu et al. [Liu94], Suzuki et al. [Suz94] comment the roughness measured by AFM and SE having nearly the same value as being in “reasonable agreement” with each other. In this study, average d(SE)/d(RMS-AFM) ratios of 0.89, 1.05, and 1.46, and average d(SE)/d(R_a-AFM) ratios of 1.11, 1.31, and 1.85 were obtained using window sizes of 1×1 μm^2, 10×10 μm^2, and 50×50 μm^2, respectively. The results suggest that the interpretation of the d(SE)/d(RMS-AFM) or d(SE)/d(R_a-AFM) ratio is not obvious. Especially, if one considers that in addition to the window size effect also the tip geometry or the curvature or slope of the surface structures influence the AFM results. SE is also affected by numerous parameters,

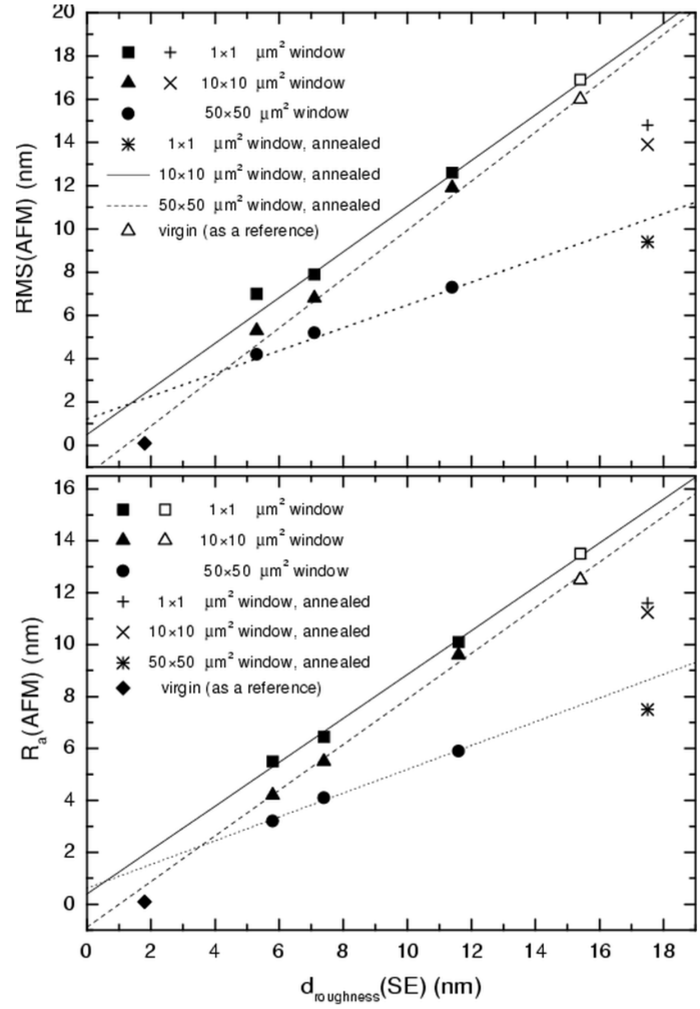

Figure 3.5. Mean roughness (R_a) and RMS roughness measured by AFM correlated with roughness determined by SE.

such as the used optical model, the inhomogeneity or the FFT spectra of the surface profile [Fan96] (i. e. the surface geometry). The surface roughness has several characteristics, such as the height of the protrusions, shape or density of surface features. The AFM and SE results characterize the surface roughness with only one value, which is not enough for the complete surface description. The RMS roughness values were completed with those of fractal analysis [Spa94], or FFT spectra were considered by several authors to obtain more information of the surface. Results presented in this study show that roughness obtained by AFM and SE show a very good correlation, if measurements are performed on polysilicon prepared under the same conditions. This seems to be a prerequisite of the correlations, since samples prepared in another way do not fit the correlation line. The good correlation may be attributed to the similar surface character, which may change when using other preparation. This causes the measured values to get out of the correlation line. The word "character" refer to other surface parameters, too, which are not described by RMS roughness but can change the ellipsometry measurement (such as the FFT spectra shown in Fig. 3.2).

A virgin silicon reference sample having a 2 nm native oxide layer was also measured by SE and the measurement was evaluated using the same model as the one for the surface roughness layer of the polysilicon samples (64% c-Si + 36% void). A layer thickness of 1.8 nm was obtained using this model. This thickness can be considered as a reference value for the case, if there is no roughness, only a native oxide layer. This point is also plotted on Fig. 3.5. The corresponding AFM roughness is 0.09 nm measured also on the surface of a virgin silicon sample [Bir96]. If this point is considered to be the reference for zero roughness with a native oxide layer, then the origin of the plot in Fig. 3.5 has to be shifted to this reference point. The native oxide can be taken into account by means of this method for rough surfaces with a simple surface roughness model.

Chapter 4

Ion-Implantation of Single- and Polycrystalline Silicon

Ion-implantation caused damage formation has been intensively studied, motivated by both fundamental and technological reasons. Widely used measurement techniques are TEM, RBS and optical reflection and transmission spectroscopy. Ellipsometry has been proved to be a very effective tool for the characterization of ion-implanted semiconductors, because it is a non-destructive, non-contact, rapid, and sensitive measurement technique. The depth distribution of the disorder obtained by RBS combined with the channeling effect can be used to construct realistic optical models and to cross-check the ellipsometry results [Loh94a, Loh82, Loh83, Fri85, Fri84, Fri91]. These experiments emphasized the potential of ellipsometry for rapid dose homogeneity checking in industrial applications provided that it is calibrated against channeling data. The applicability of SE for the non-destructive determination of damage depth profiles in ion-implanted semiconductors has been demonstrated by several research groups [Erm83, Ved85, McM86, Van91, Fri97, Loh94c]. Vanhellemont et al. [Van91] state that spectroscopic ellipsometry “can be considered as a nondestructive, cheap poor man’s optical Rutherford backscattering spectrometer and even as a one-dimensional optical high-resolution microscope”.

In this chapter the determination of medium mass (Ar^+) ion-implantation induced damage profiles in single- and polycrystalline silicon using SE and RBS is discussed.

4.1 Experimental details

4.1.1 Short description of backscattering spectrometry

Backscattering spectrometry (BS) is a method for measuring thin surface layers with high precision [Chu78, Gyu85]. It is based on the analysis of backscattered ions from the sample, which can be used for the determination of the composition and layer thickness. Most frequently used ions are the $^4He^+$ or $^1H^+$ with an energy of 1-4 MeV. Thin layers of 1-2 μm can be measured with a resolution of 20-30 nm using 2 MeV $^4He^+$ ions. The resolution can be further enhanced to 3-5 nm by optimizing the scattering geometry [Mez78].

Measuring single-crystalline samples, additional information is provided by taking advantage of the channeling [Fel82].

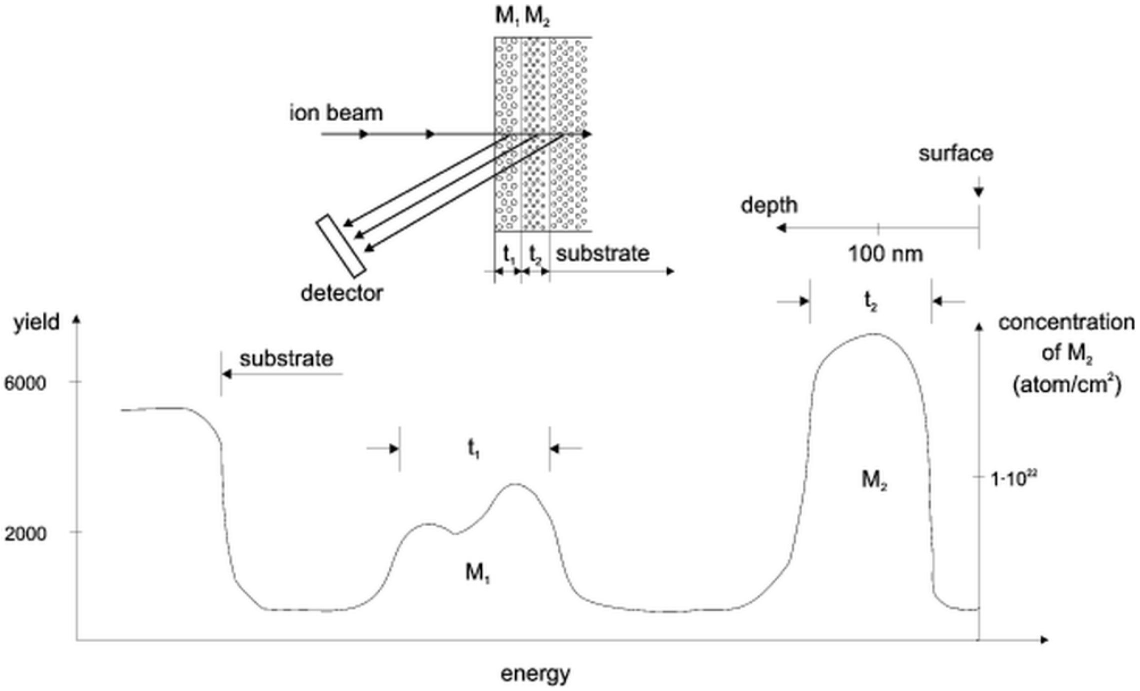

Figure 4.1. A general RBS spectrum.

RBS is based on the elastic scattering on the atoms of the measured sample. The are two mechanisms, in which the monoenergetic ion beam looses its energy: elastic scattering or inelastic scattering. The elastic scattering can be related to the mass of the incident ions and the target atoms. The inelastic scattering depends on the chemical composition of the target.

In the case of an elastic scattering, when an ion of mass M_1 and energy of E_0 scatters on a target atom of mass M_2 at a scattering angle of θ, and the ion has an energy of E_1 after the scattering, the kinematic factor can be described as

$$K = \frac{E_1}{E_0} = \left[\sqrt{1 - \left(\frac{M_1}{M_2}\right)^2 \sin^2\theta} + \frac{\frac{M_1}{M_2}\cos\,\theta}{1 + \frac{M_1}{M_2}} \right]^2 . \tag{4.1}$$

The kinematic factor depends only on the ratio of the projectile to the target masses and on the scattering angle θ. After the collision, the projectile atom has an energy, which depends on the mass of the target atom. Therefore, the target atoms of different masses have a different location on the backscattering spectrum (yield vs. energy). Fig. 4.1 shows an RBS spectrum of a target with two layers of masses M_1 and M_2 and thicknesses of t_1 and t_2 ($M_2 > M_1 > M_{substrate}$). The scattered projectile atoms have different energies depending on the mass and depth of the target atoms. As a result, target atoms of different masses have a different depth scale. The concentration shown on the right axis is proportional to the differential cross-section defined as

$$\frac{d\sigma}{d\Omega} = \left(\frac{Z_1 Z_2 e^2}{2E\sin\theta}\right) \frac{4}{\sin^4\theta} \frac{\left(\sqrt{1 - \left[\frac{M_1}{M_2}\sin\theta\right]^2} + \cos\theta\right)}{\sqrt{\left(1 - \left[\frac{M_1}{M_2}\sin\theta\right]^2\right)}}, \tag{4.2}$$

where σ is the scattering cross section, $d\Omega$ is the differential solid angle (only primary particles that are scattered within the solid angle $d\Omega$ spanned by the detector are counted), E is the ion energy before the collision, θ is the scattering angle, Z_1, Z_2 are the atomic numbers of the projectile atoms with masses of M_1 and M_2, respectively.

There is another way for an incident ion to loose energy. As the particle pushes its way through the target, it slows down and its kinetic energy decreases. This energy loss $\frac{dE}{dx}$ is a function of the energy and mass of the incident particles and of the mass of the target atoms. The task is to relate the energy E_1 of the detected particle to the depth x at which the backscattering event occurs. The problem is that the energy E before scattering is not an experimentally accessible quantity, but E_0 (energy of the incident particle) and E_1 are. One thus desires to find x in terms of E_0 and E_1. There are three ways of doing this:

- use tabulated values of $\frac{dE}{dx}$ and execute the integrations numerically to find corresponding sets of E and x,
- assume that $\frac{dE}{dx}$ is constant over each path,
- assume some functional dependence for $\frac{dE}{dx}$; matching pairs of E and x and of x and E_1 can then be obtained analytically.

If one assumes a constant value for $\frac{dE}{dx}$ along the inward ($\frac{dE}{dx} = S(E_0)$) and outward ($\frac{dE}{dx} = S(KE_0)$) paths, the energy difference ΔE can be written as

$$\Delta E = KE_0 - E_1^{'} = \Big(\frac{K}{\cos\theta_1}S(E_0) + \frac{1}{\cos\theta_2}S(KE_0)\Big)x = \langle S\rangle x, \tag{4.3}$$

where K is the kinematic factor of eqn. 4.1, θ_1 and θ_2 are the angles between the sample normal and the direction of the incident beam and of the scattered particle, respectively. Using the energy loss factor S, one can assign a depth scale to the energy axis (this is called surface approximation and is very good for He^+ in 1-3 MeV region.

The depth resolution can be expressed as

$$\delta x = \frac{\delta E}{\langle S\rangle}, \tag{4.4}$$

where δE is the energy resolution of the detector. $\langle S\rangle$ can be increased by having θ_1 and/or θ_2 near 90°. δx can in this case be decreased by a factor of 10. In our measurement two spectra were taken simultaneously at $\theta = 165°$ and $\theta = 97°$. In the first case the mass resolution is better and the depth to which the sample can be measured is higher. In the second case there is a better depth resolution but the mass separation is worse and only a few hundred nm can be seen.

When the beam is aligned with a low-index axial direction of a single-crystal substrate, the incident particles can be steered or channeled after entering the crystal. The channeling effect arises because rows or planes of atoms can "steer" energetic ions by means of a correlated series of gentle, small-angle collisions. Channeling effect measurements have had three major applications in backscattering analysis [Chu78]:

- amount and depth distribution of lattice disorder,
- location of impurity atoms in the lattice sites,

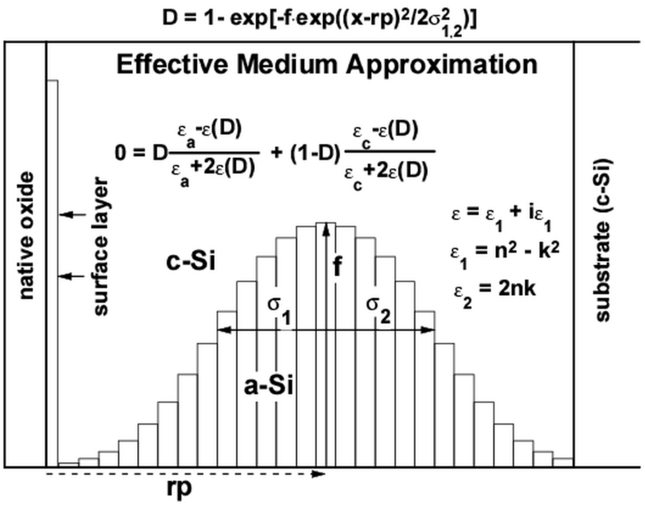

Figure 4.2. Optical model used for the measurement of the ion-implanted single-crystalline silicon samples (after [Fri92b]).

- composition and thickness of amorphous surface layers.

The presence of a thin oxide or hydrocarbon layer or surface disorder can cause an increase in the random component of the aligned beam. Conversely, of course, channeling measurements can be used to evaluate the condition of the surface.

4.1.2 Sample preparation and measurements

100 keV Ar^+ ions were implanted at room temperature into 5.1-6.9 Ωcm, p-type, ⟨100⟩ single-crystalline silicon using current densities of 370 nA/cm^2-400 nA/cm^2. The implanted dose was varied from 0.725×10^{14} cm^{-2} to 4.65×10^{14} cm^{-2}.

The ellipsometry spectra were obtained using a SOPRA ES4G rotating polarizer spectroscopic ellipsometer in the spectral range of 250-750 nm at an angle of incidence of 75.16°.

Rutherford backscattering and channeling techniques with 1.5 MeV He^+ ions were used to determine the buried disorder. The detector was placed to detect ions scattered through 97°, i. e. with a glancing exit angle of 7° to the surface. In this geometry, the depth resolution is better than 5 nm [Mez78]. To evaluate the spectra we used the RBX program written by Kótai [Kót94], which can handle channeled spectra too.

For the analysis of the SE data optical models were used, which consist of a stack of homogeneous layers (see Figure 4.2): a native oxide layer at the surface, a thin amorphous silicon layer under the native oxide layer modeling the anomalous surface amorphization [Loh94b], and 20 layers with fixed and equal thicknesses and damage levels described by a coupled half-Gaussian depth profile function [Fri92a, Fri85]. The half-Gaussian profile is described by four independent parameters: the center (rp), the height (f), and the two standard deviation values (σ_1 and σ_2). Taking into account that the damage level is saturated at the amorphous state, the damage depth profile can be described by the following expression:

$$D(x) = 1 - e^{-fe^{\frac{-(x-rp)^2}{2\sigma^2}}} \tag{4.5}$$

$$\begin{cases} \sigma = \sigma_1, \text{ when } x < rp, \\ \sigma = \sigma_2, \text{ when } x > rp, \end{cases}$$

As shown in Fig. 4.2, D gives the ratio of the amorphous silicon and the single-crystalline silicon used in the B-EMA (see Chapter 1.1.3). The dielectric function of each sub-layer can then be calculated using (see Section 1.1.3)

$$0 = f_a \frac{\overline{\epsilon}_a - \overline{\epsilon}}{\overline{\epsilon}_a + 2\overline{\epsilon}} + f_b \frac{\overline{\epsilon}_b - \overline{\epsilon}}{\overline{\epsilon}_b + 2\overline{\epsilon}}. \qquad (4.6)$$

Then, using this model, there are six unknown model parameters (rp, f, σ_1, σ_2, the thickness of the surface oxide and the surface amorphous layer).

The calculated spectra were fitted to the measured ones varying the model parameters (thickness of the native oxide layer, the thin amorphous silicon layer, and the four parameters describing the Gauss-profile). The evaluation was performed using a software called “CALLIP” written by O. Polgár, which supports the characterization of damage distribution in implanted materials.

The main problem of the fitting procedure is the choice of the initial values of the model parameters. If this initial values are not chosen properly, the program can find a false (or local) minimum.

4.2 Implantation of single-crystalline silicon

The ellipsometric measurement data were first analyzed in the UV spectral region. The penetration depth of the light is not more than 80 nm at the wavelength of 400 nm, even for crystalline silicon (see Table 1.2 on page 25). Thus, a simple optical model can be used taking into account the surface oxide, the surface amorphous layer [Loh94c], and the bulk with the combination of crystalline silicon and fine-grained polycrystalline silicon [Jel93]. Fig. 4.3 shows this optical model together with the measured and fitted curves for different doses.

The calculated data fit well to the measured ones for all doses. Measured data of a virgin silicon sample is also plotted as a reference. The model parameters as a function of implanted dose are shown in Table 4.1. The thickness of the SiO_2 layer slightly increases with increasing dose (from 2.43 nm to 3.11 nm). The thickness of the a-Si layer also increases with increasing dose [Loh94c]. The increase is more rapid above the dose of 2.21×10^{14} cm^{-2}. The pc-Si content of the bulk material increases from 25.4% to 49.3%. The standard deviation (σ) and the 95% confidence limits are acceptable for all doses.

Figure 4.4 shows the measured ellipsometry spectra of crystalline silicon implanted using 100 keV Ar^+ ions in the spectral range over 250-740 nm. The implanted doses are varied between 0.725×10^{14} cm^{-2} to 4.65×10^{14} cm^{-2}. For the higher ion doses (3.2×10^{14} cm^{-2} and 4.65×10^{14} cm^{-2}) the curves change drastically, especially for cosΔ at wavelengths above 500 nm. The insert shows the change of cosΔ in the spectral range over 280-350 nm.

Figure 4.5 shows the measured and fitted spectra for four different doses in the whole spectral range. The optical model consists of a native oxide layer on top of the sample, a thin near-surface damaged layer below the top oxide layer, a layer describing

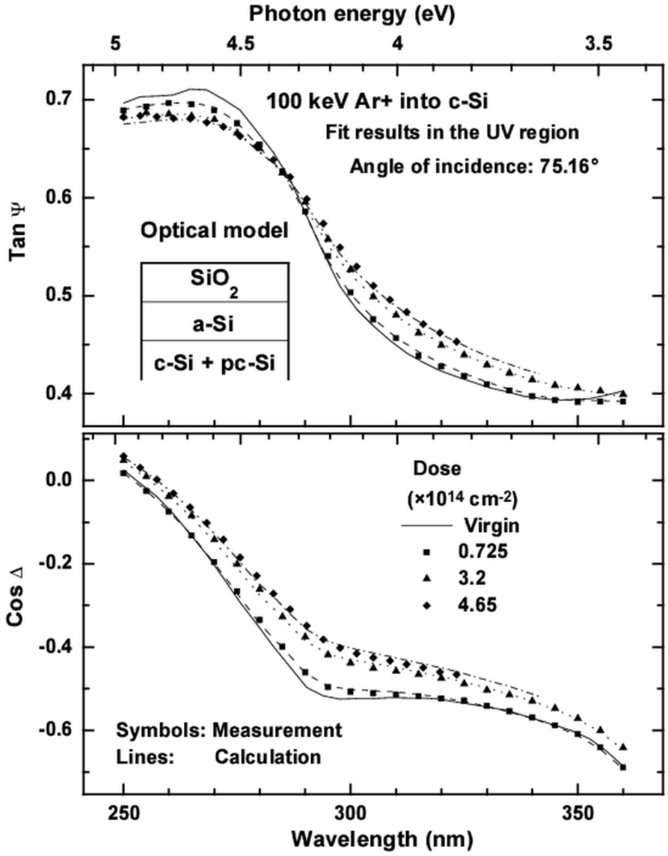

Figure 4.3. Measured and fitted ellipsometry spectra of single-crystalline silicon samples implanted with 100 keV Ar^+ ions for three different doses together with the measured spectrum of a virgin sample. The fit was performed using the spectral range below 360 nm (UV). The optical model used is also shown in the figure.

the damage in vicinity of the projected range, and a single-crystalline silicon bulk (see Fig. 4.6). The layer describing the damage is divided into 20 sub-layers with fixed and equal thicknesses, each having the components of single-crystalline silicon and implanted amorphous silicon. The fraction of the amorphous silicon is described by a coupled half-Gaussian depth profile function [Fri92b].

For cross-checking the SE results, high depth resolution RBS measurements were made with the detector placed at 97° scattering angle for the series of the implanted samples and for a virgin sample used as a reference (Fig. 4.7). The buried disorder is in the depth of approximately 30 nm to 150 nm for the dose of 4.65×10^{14} cm^{-2}. The buried disorder layer is totally amorphous near 100 nm for the dose of 4.65×10^{14} cm^{-2}. The surface amorphous layer is also clearly seen near the surface, which proves the validity of the model used in the UV range investigation.

Figure 4.8 shows the buried depth profiles calculated from SE and RBS measurements using the fit result shown in Figures 4.5 and 4.7. The depth profiles obtained by these two different methods agree well. The peak of the damage profile is at 100 nm, which agree also with the TEM results (Fig. 4.9). The damaged region shown by TEM is also plotted in Fig. 4.8 for the dose of 4.65×10^{14} cm^{-2}. At the dose of 4.65×10^{14} cm^{-2} the damage layer become totally amorphous.

Table 4.1. Fitted model parameters used in the UV range as a function of the implanted dose. The standard deviation (σ) in the last column shows the quality of the fit.

Dose ($\times 10^{14}$ cm^{-2})	D$_{SiO_2}$ (nm)	D$_{a-Si}$ (nm)	C$^{(*)}_{pc-Si}$ (%)	σ
0.725	2.43±0.75	0.25±0.11	25.4±3.9	0.0051
1.050	2.43±0.32	0.32±0.12	26.4±4.3	0.0056
1.520	2.59±0.40	0.40±0.12	32.5±4.2	0.0063
2.210	2.71±0.46	0.46±0.14	40.0±5.0	0.0066
3.200	2.95±0.66	0.66±0.17	45.1±5.8	0.0075
4.650	3.11±0.96	0.94±0.18	49.3±6.2	0.0089

(*) Concentration of pc-Si in the optical model

It has to be noted that many local minima can occur during the regression especially in the case of the low-dose implants. Knowledge of the approximate damage profile from the RBS measurement can help to avoid to get into local minima during regression analysis. Such depth profile estimations can be received by ion-solid interaction simulations such as TRIM code.

4.3 Implantation of polycrystalline silicon

Polysilicon samples prepared as described in Section 4.1.2 were implanted using the same parameters as for the single-crystalline samples. The TEM picture of a polysilicon sample implanted with a dose of 4.65×10^{14} cm^{-2} is shown in Fig. 4.10. The implanted dose is the same, as for Fig. 4.9. In the case of implanted polysilicon there is a continuous damaged region from the surface to the end of the damaged layer, in spite of a buried damage, as in the case of implanted single-crystalline silicon.

Figure 4.11 shows the measured and calculated ellipsometry spectra of ion-implanted polysilicon samples. The implantation conditions were kept identical to that used for the single-crystalline samples. The interference oscillations resulting from the polysilicon-on-oxide structure are clearly seen on the plot.

The comparison of the model for the implanted polycrystalline silicon and for the single-crystalline silicon is shown in Fig. 4.6. In contrast to the model for the single-crystalline silicon, the model for the implanted polysilicon (Fig. 4.6b) consists of the surface roughness layer (described by a B-EMA mixture of pc-Si, implanted amorphous silicon (i-a-Si) and voids), the damaged layer (described similarly as in case of the single-crystalline silicon, but the implanted amorphous silicon reference data was mixed with fine-grained polycrystalline silicon in spite of single-crystalline silicon), the layer describing the non-damaged part of the polysilicon (pc-Si), the buried oxide layer, and a single-crystalline silicon substrate. The complex refractive index denoted by "pc-Si*" was calculated by the B-EMA using a mixture of 84% c-Si and 16% a-Si (a-Si: chemical vapor deposited amorphous silicon [Jel93]). This was the "mixture" giving the best fit to the non-implanted polysilicon sample, which was identical to the implanted ones.

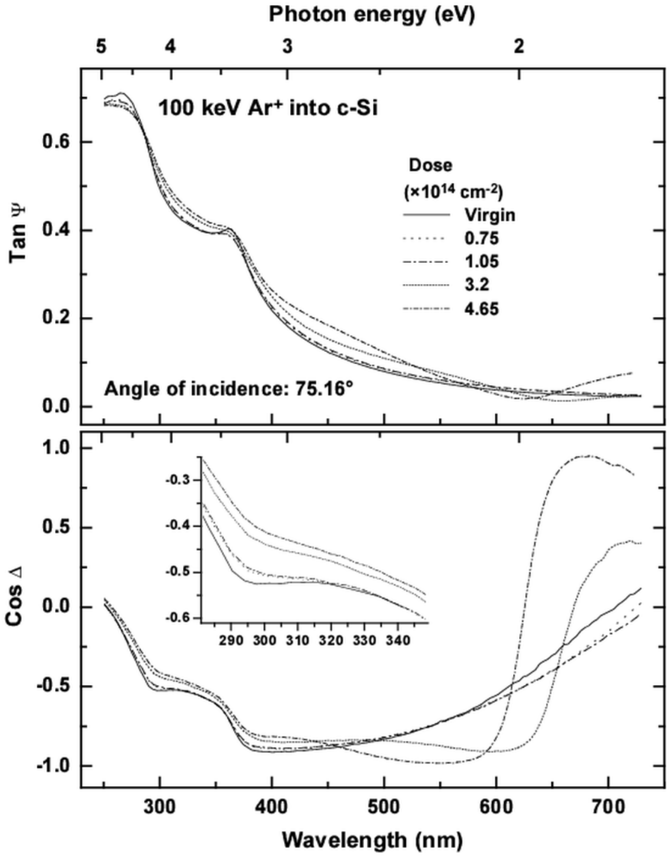

Figure 4.4. Measured ellipsometry spectra of single-crystalline silicon samples implanted with 100 keV Ar^+ ions for four different doses using the entire spectral range of the measurement. The optical model used for the calculations is described in the text.

Figure 4.12 shows damage depth profiles for the implanted polycrystalline silicon samples obtained by spectroscopic ellipsometry. For higher doses the damaged region extends from the surface to a depth of approximately 130 nm. This result agrees well with that of the TEM pictures. The damage of the surface area can be explained by an effect similar to the surface amorphization [Loh94c], which occurs in this case at the grain boundaries, and increases the damage. The damages shown in Figures 4.8 and 4.12 are relative values. This means that the damage is obtained as the content of the amorphous component relative to the single-crystalline (implanted c-Si) or to the polycrystalline (pc-Si) component calculated by the B-EMA. In case of implanted polycrystalline silicon the "background" for the implanted amorphous silicon (a-Si) component is the "pc-Si" reference data in the optical model (see Fig. 4.6b). The "pc-Si" reference data was simulated by combining the single-crystalline and chemically vapor deposited amorphous silicon. This amorphous content has a similar effect on the dielectric function as the implantation, because the dielectric function of the implanted amorphous silicon is close to that of the chemically vapor deposited amorphous silicon. Consequently, the maximum of the relative damage of implanted polysilicon (Fig. 4.12) is at a lower level than for the implanted single-crystalline silicon (Fig. 4.8).

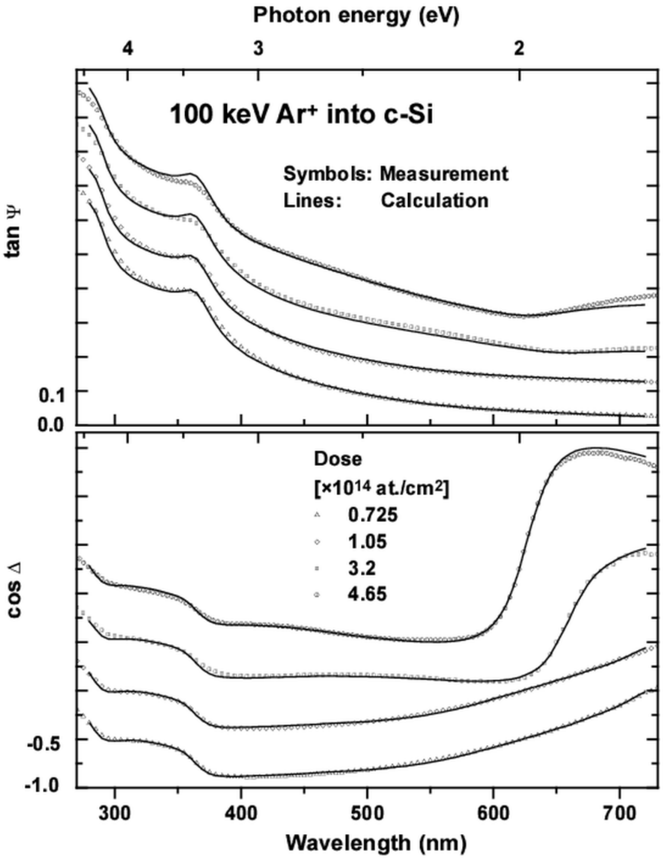

Figure 4.5. Measured and fitted ellipsometry spectra of single-crystalline silicon samples implanted with 100 keV Ar^+ ions for four different doses using the entire spectral range of the measurement. The optical model used for the calculations is described in the text. The curves are shifted with 0.1 and 0.5 with increasing doses for tanΨ and cosΔ, respectively.

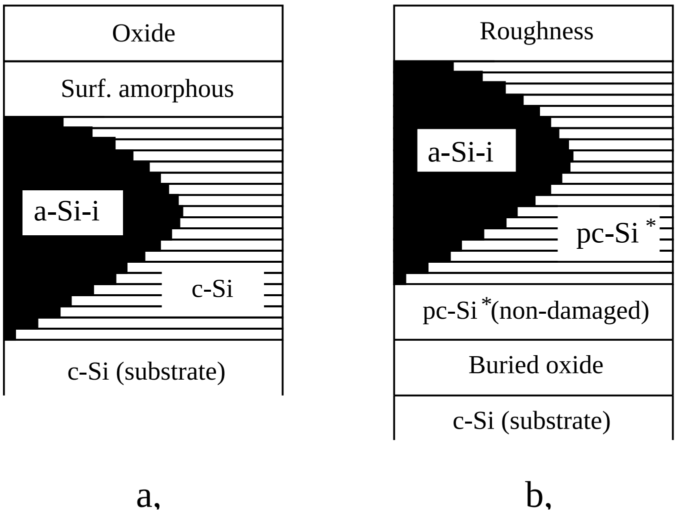

Figure 4.6. Optical models used for the calculations and fits for the ion-implanted single-crystalline (a) and polycrystalline (b) silicon samples. The complex refractive index denoted by "pc-Si*" was calculated by the B-EMA using a mixture of 84% c-Si and 16% a-Si (a-Si: chemical vapor deposited amorphous silicon [Jel93]). This was the "mixture" giving the best fit to the non-implanted polysilicon sample, which was identical to the implanted ones.

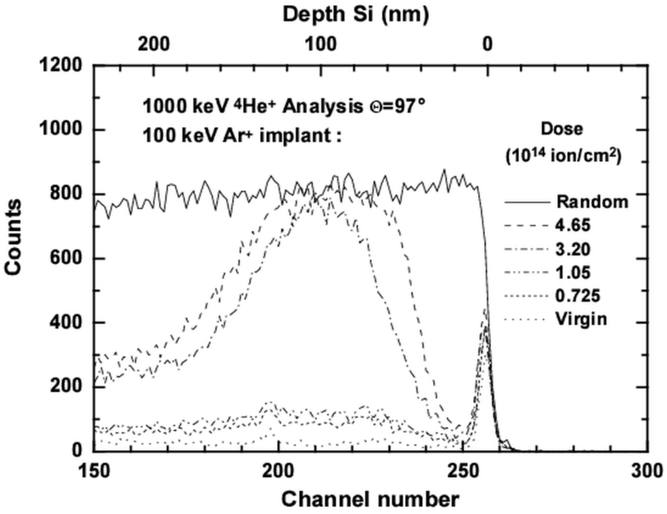

Figure 4.7. Random and aligned high depth resolution RBS spectra of single-crystalline silicon samples implanted with 100 keV Ar^+ ions for four different doses together with the measured spectra of a virgin sample. The measurement was recorded with a detector placed at the scattering angle of 97°.

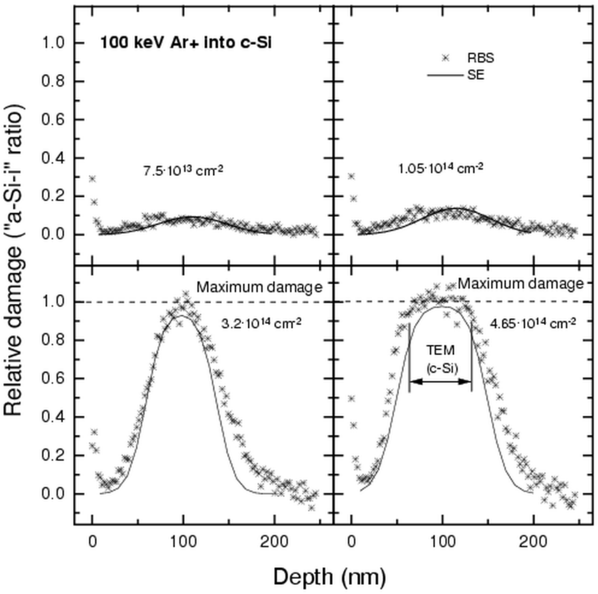

Figure 4.8. Deduced damage depth profiles for single-crystalline silicon samples implanted with 100 keV Ar^+ obtained using SE and RBS. The implanted doses were varied from 0.725×10^{14} cm^{-2} to 4.65×10^{14} cm^{-2}. For the dose of 4.65×10^{14} cm^{-2} the damaged range obtained by TEM is marked in the figure.

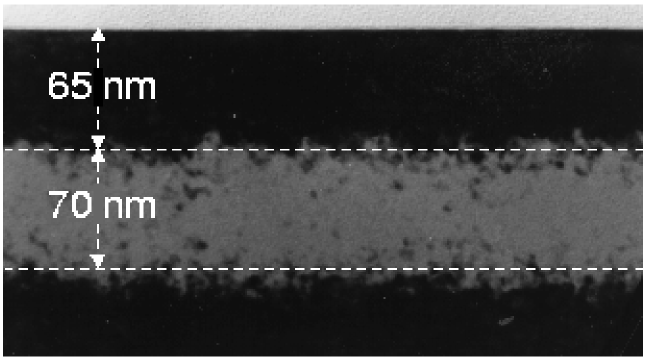

Figure 4.9. TEM micrograph of a single-crystalline silicon sample implanted with 100 keV Ar^+ ions using a dose of 4.65×10^{14} cm^{-2}.

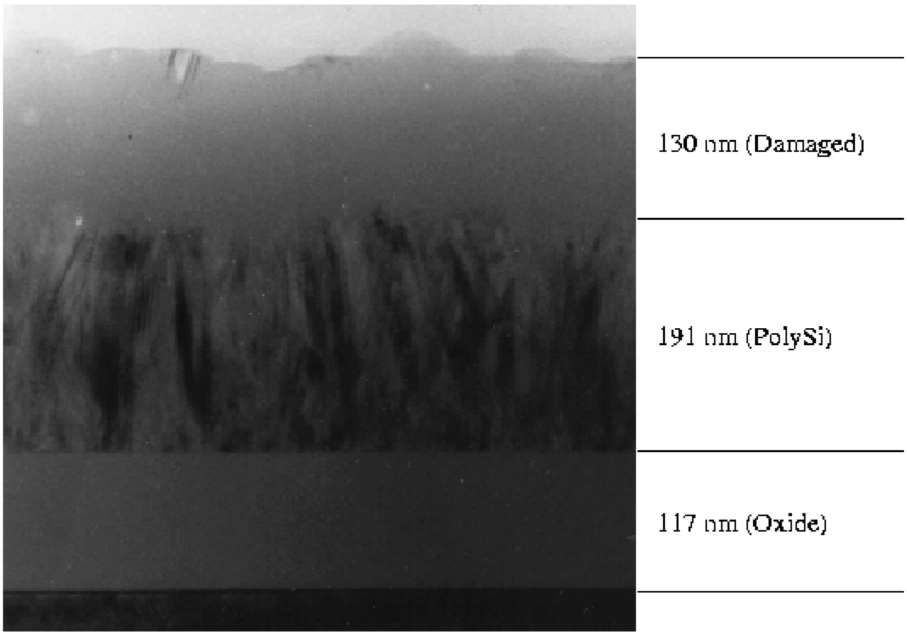

Figure 4.10. TEM micrograph of a polycrystalline silicon sample implanted with 100 keV Ar^+ ions using a dose of 4.65×10^{14} cm^{-2}. The picture shows a totally damaged layer of 130 nm at the surface of the polycrystalline layer, a non-damaged polycrystalline silicon layer of 191 nm thickness, and a buried oxide layer of 117 nm at the bottom of the picture.

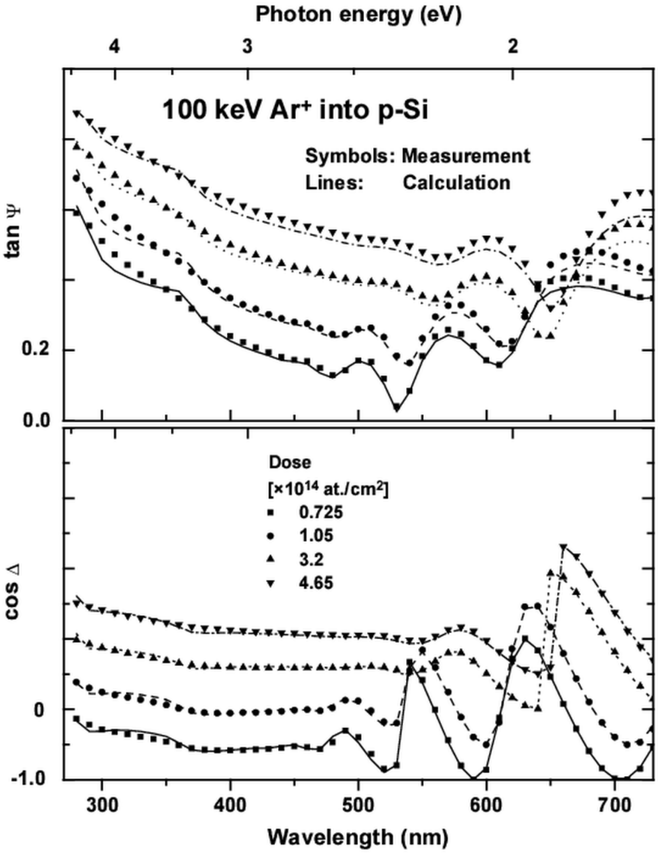

Figure 4.11. Measured and calculated ellipsometry spectra of polycrystalline silicon samples. The implantation conditions were the same as for the single-crystalline samples. The curves are shifted with 0.1 and 0.5 with increasing doses for tanΨ and cosΔ, respectively.

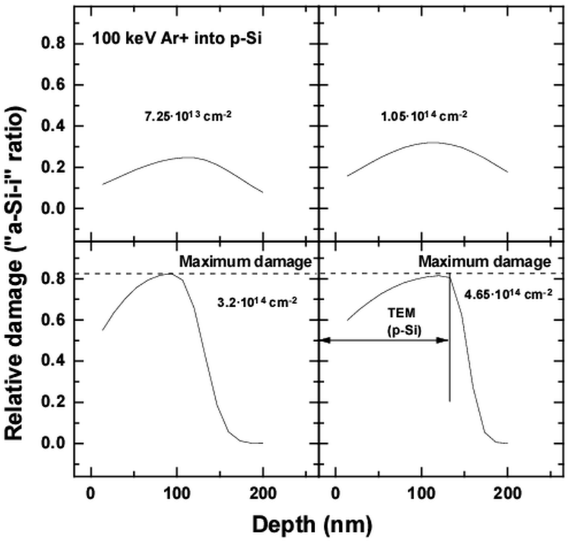

Figure 4.12. Deduced damage depth profiles for polycrystalline silicon samples implanted with 100 keV Ar^+ obtained using SE. The implantation conditions were the same as for the single-crystalline samples. The damaged region obtained by TEM is also marked in the figure.

Chapter 5

In situ ellipsometry in vertical furnace

In situ measurement is regarded as a technique, which will play a key role in the cost-effective manufacturing and – on the research side – in the better understanding of the process [Leh98a, Leh98b]. It helps to shorten the process ramp-up and improve process stability. One of the main advantages is the reduced number of monitor wafers. Especially regarding the processing of 300 mm wafers, the demand for process control without monitor wafers is extremely high.

Single-wavelength ellipsometry [Hau73] and later spectroscopic ellipsometry [An91, Pie93b] have been used for the real time characterization of the nucleation, growth, and optical functions of thin films [Col93, Shi97, Tac94]. Surface processes and surface treatments were analyzed *in situ* in a vapor phase epitaxy chamber equipped with ellipsometry and other analytical tools in Refs. [Hot79, Hot81, Gau85]. Ellipsometry was applied because of its high sensitivity to surface properties.

Real time characterization of hidrogenated amorphous silicon is motivated by the promise of the cheap manufacturing of microelectronic and photovoltaic devices [Col89, An90]. Nucleation and growth of nanocrystalline [Shi97], microcrystalline [Col89, Koh99] and polycrystalline silicon [Tac94] have been investigated in order to have insight into the deposition process and to optimize the process parameters.

In semiconductor technology, the formation of thin films by high temperature processes is one of the key techniques. Thermal oxidation and chemical vapor deposition comprise the most decisive manufacturing steps such as gate oxide formation, deposition of stacked dielectrics, and deposition of conductive layers as polysilicon or amorphous silicon.

Solutions for accessing batch furnace processes by high temperature ellipsometry are key issues in this field [Sch93b, Ber94]. The major requirements for the use of these techniques will be addressed in this chapter. First, integration of ellipsometry in the vertical furnace by adapting the ellipsometer arrangement to the furnace geometry will be discussed. Then correction for the effect of the beam-guiding system on the measurement parameters, determination and use of high-temperature dielectric function data for reference, and *in situ* measurements of crystallization processes will be investigated.

5.1 Instrumentation

The speed of the measurement have to be adjusted to the speed of the actual process. It has to be decided, how much precision is it worth sacrificing for the speed. For *in situ* spectroscopic ellipsometry the measurement is performed parallely for all wavelengths. The reflected beam is dispersed by a diffraction grating. The spatially separated light of different wavelengths is directed to a photodiode array detector. A photo diode array (PDA) is a linear array of individual photodiodes fabricated using integrated circuit technology. PDAs are also referred to as linear image sensors (LIS). The necessary electronic switches needed to access each individual photodiode are built right onto the “chip”.

There are PDAs specifically designed for spectroscopy. Each element is tall and thin to better match the slit geometry used by spectrographs. Several PDAs are available with different numbers of elements from 128 up to 1024. The high saturation levels of the photodiode array and the low readout noise of the amplifier results in a high dynamic range of over 30,000:1 and maximum signal to noise ratio of over 10,000:1. The very low dark current of 0.1 pA/pixel at 25°C means a very low associated dark noise, and with a carefully designed electronic circuit this ensures that the detector heads have minimal dark and signal noise. This makes the system ideal for high precision measurements. The intensity of the incoming light can be adjusted by a slit, so that the diodes doesn’t get saturated.

Since the measurement is performed simultaneously for all wavelength, the intensity cannot be adjusted separately for the individual wavelengths. This means that if there are great differences in the intensity throughout the spectrum, the intensity for the poorly irradiated elements cannot be increased without saturating the elements in the high irradiation range. According to the spectral irradiance of the xenon lamp (used in most cases), the intensity at the UV-end of the spectrum is always weak. For the *ex situ* scanning ellipsometers, which perform individual measurements at the different wavelengths, the integration time can be adjusted for all wavelengths taking into account the actual intensity. Furthermore, *ex situ* scanning ellipsometers can increase the precision by adjusting the analyzer azimuth for each wavelength. *In situ* ellipsometers with diode array use the same analyzer position to all wavelengths because the measurement is made at the same time for all wavelengths.

A crucial problem of the *in situ* measurements is the synchronization of the sampling to the rotation of the analyzer or polarizer. The array is an integrating detector. According to the Hadamard-transformation (see equations 1.52, 1.53, 1.54, and 1.55) four successive readouts are performed over a single optical period (with identical exposure times $\frac{\pi}{4\omega}$) in order to deduce α' and β' (see equations 1.56 and 1.57). Additionally, a consistency check is made using the equation

$$0 = S_{1k} - S_{2k} + S_{3k} - S_{4k}. \tag{5.1}$$

The consistency check is non-zero in the presence of alignment errors. The greatest error sources are (i) the integration error, (ii) the non-linearity, (iii) the image persistence, and (iv) the stray light [An91]. Equations 1.52, 1.53, 1.54, and 1.55 were derived assuming that for S_j integration of I(t) (eqn. 1.51) is performed over a full optical quadrant. In fact, the pixel is insensitive to photons arriving during its own read time. This generates errors in the experimental spectra of the order of $\frac{\omega t}{\frac{\pi}{4}}$, where

t_r is the pixel group read time. For an ellipsometer having $t_r = 35\ \mu$s the estimated integration error is 0.0035. The error caused by image persistence rise form the incomplete readout of charge accumulated during the previous exposure. Image persistence and non-linearity corrections improve the precision by 0.005 and 0.002, respectively.

The speed of the measurement can be increased by grouping the pixels of the photodiode array. Grouping by 2, 4, 8, or 16 means that the number of the pixels to be read out is 512, 256, 128, or 64, respectively, in spite of 1024. The polarizer or analyzer rotation frequencies are increased accordingly. By grouping the pixels a speed of up to 12 ms per measurement can be achieved. For an *in situ* measurement on a complicated structure (for example polysilicon-on-oxide) the bottleneck of the measurement speed is not the data acquisition but rather the data evaluation. The evaluation time is a function of

- the complexity of the measured structure,
- the spectral range,
- the number of data points,
- the optical model,
- and last but not least, the speed of the used computer.

5.2 Measurements using the beam-guiding system

At the Fraunhofer Institute for Integrated Circuits (FhG-IIS-B), Germany, a SOPRA MOSS-OMA (Multilayer Optical Scanning Spectrometer – Optical Multi-channel Analyzer) spectroscopic ellipsometer was integrated in a vertical furnace for the characterization of chemical vapor deposition and thermal oxidation. *In situ* ellipsometry studies have been made at the institute for several years. Real time feedback control of oxidation furnaces using *in situ* ellipsometry is a very important and successful research field [Sch93b, Sch93a]. The major goal of the recent *in situ* spectro-ellipsometric activity was to adapt the ellipsometer arrangement to the furnace geometry with a minimum impact on the furnace process performance. Modifications in the furnace geometry were restricted as far as possible, to show that a fast integration in an existing industrial equipment with minor costs can be done. This aim led to a novel beam-guiding system shown in Fig. 5.1.

The ellipsometer arms (the analyzer and polarizer units) are mounted to the base plate of the furnace. The beam is guided through four prisms from the polarizer unit to the wafer and back to the analyzer. There are two 90° prisms at the bottom and two 70° or 75° prisms at the top. The wafer carrier and the base plate with the ellipsometer arms form a stable mechanical unit, which moves vertically with the boat loader. Since the ellipsometer is firmly coupled to the base plate and the boat, the calibration and adjustment can be carried out outside the furnace. The alignment remains constant during loading and unloading. Using this setup no modification of the process tube and the heating cassette is required.

As shown in Fig. 5.1, the light beam is reflected four times. At total internal reflection r_p and r_s are equal to 1, and $\delta_{r,p}$ and $\delta_{r,s}$ (see eqn. 1.7) are functions of the

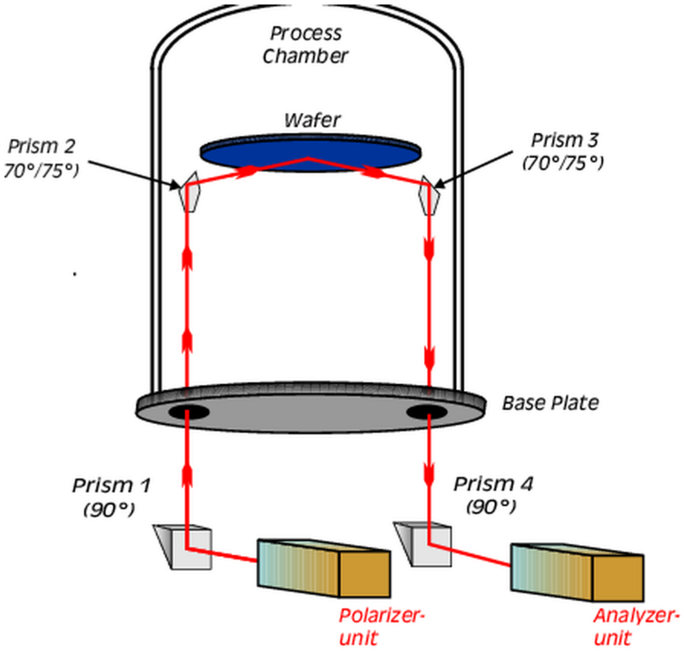

Figure 5.1. Beam path of the ellipsometer in the vertical furnace.

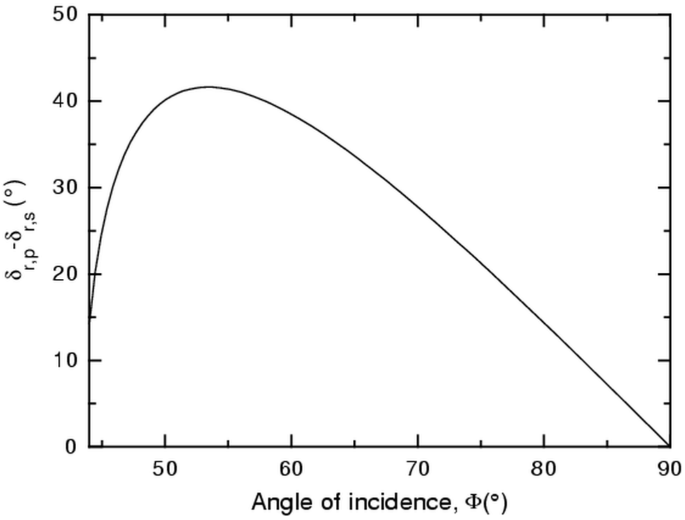

Figure 5.2. Phase shift $\delta_{r,p} - \delta_{r,s}$ (eqn. 5.2) caused by the internal reflection at the prisms (λ=546.1 nm, n_{glas}=1.45).

angle of incident. This means that the use of the prisms will not change tanΨ (see eqn. 1.5) but cosΔ. The change in cosΔ at the prisms will be a function of the angle of incidence. Consequently, the alignment will affect the phase shift caused by the prism. The phase shift

$$\delta_{r,p} - \delta_{r,s} = 2\left[\arctan\frac{\sqrt{\sin^2\Phi - (\frac{n_0}{n_p})^2}}{\cos\Phi(\frac{n_0}{n_p})^2} - \arctan\frac{\sqrt{\sin^2\Phi - (\frac{n_0}{n_p})^2}}{\cos\Phi}\right] \tag{5.2}$$

is shown in Fig. 5.2. The angle of incidence for the 90° and the 70° prisms are $\Phi = 45°$ and $\Phi = 55°$, respectively. Figure 5.2 shows that for the 90° prism ($\Phi = 45°$) the

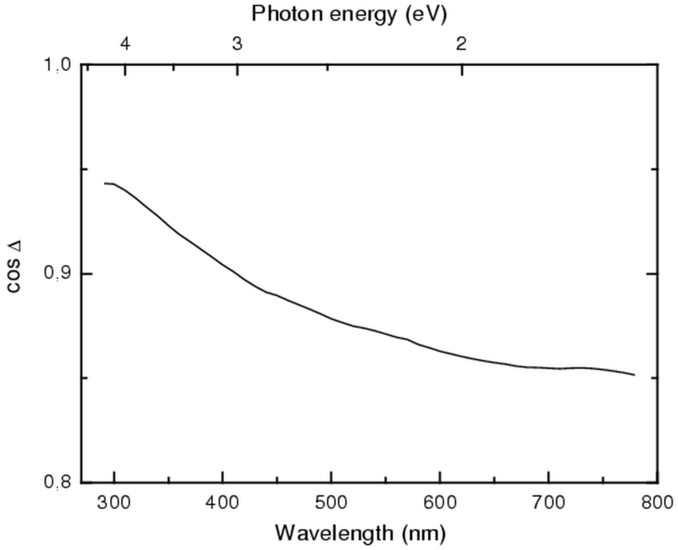

Figure 5.3. cosΔ spectrum measured on a glass using the beam guiding system. The phase shift is strongly dependent on the wavelength.

phase shift is strongly dependent on Φ having a value of ≈23°. At the 70° prisms (Φ = 55°) the phase shift is higher (≈40°), but the dependence on Φ is lower. The phase shift depends not only on the angle of incidence, but also on the temperature and the wavelength.

The phase shift caused by the prisms can be determined by making a measurement on a glass with the beam-guiding system. Then the total phase shift (Δ_Σ) can be written as the sum of the phase shift of the glass (Δ_{glas}), the 90° prisms ($\Delta_{90^\circ,a}$ and $\Delta_{90^\circ,b}$) and the 70° prisms ($\Delta_{70^\circ,a}$ and $\Delta_{70^\circ,b}$):

$$\Delta_\Sigma = \Delta_{glas} + \Delta_{90^\circ,a} + \Delta_{90^\circ,b} + \Delta_{70^\circ,a} + \Delta_{70^\circ,b}. \tag{5.3}$$

$\Delta_{glas} = 0^\circ$ above the Brewster angle (56.3° for glass). In our case the angle of incidence at the sample is 75° or 70° using the 75° or the 70° prisms, i. e. it is above the Brewster angle. Consequently, we can write

$$\Delta_\Sigma = 0^\circ + \Delta_p, \tag{5.4}$$

where

$$\Delta_p = \Delta_{90^\circ,a} + \Delta_{90^\circ,b} + \Delta_{70^\circ,a} + \Delta_{70^\circ,b}. \tag{5.5}$$

Taking into account that we can only measure the cosine of the phase shift, we can write

$$\cos\Delta_\Sigma = \cos\Delta_p. \tag{5.6}$$

This means that measuring cosΔ_Σ, the cosine of the phase shift of the prisms can be measured directly. The cosΔ_Σ spectrum measured on a glass is used later for the phase correction. Fig. 5.3 shows an example for the cosΔ spectrum measured on a glass. It is evident from the figure that the phase shift caused by the prisms has a strong dependence on the wavelength.

When measuring on a real sample,

$$\Delta_m = \Delta_s + \Delta_p, \tag{5.7}$$

where Δ_m is the measured value and Δ_s belongs to the sample. Our aim is to measure cosΔ_s. First we can express Δ_s as

$$\Delta_s = \Delta_m - \Delta_p. \tag{5.8}$$

The available values for the determination are cosΔ_m (the measurement on the sample) and cosΔ_p (calibration measurement on the glass). Using these spectra cosΔ_s can be expressed as

$$\begin{aligned} \cos\Delta_s &= \cos(\Delta_m - \Delta_p) \\ &= \cos(\arccos[\cos(\Delta_m)] - \arccos[\cos(\Delta_p)]) \\ &= \cos(|\Delta_m| + |\Delta_p|). \end{aligned} \tag{5.9}$$

CosΔ_s is the same for Δ_m and $-\Delta_m$ or Δ_p and $-\Delta_p$. Although, using eqn. 5.8, different result should be obtained. The basic problem about the correction is that the sign of the measured Δ value is unknown when using ellipsometry with rotating polarizer or rotating analyzer. The reason will be clear if we consider eqn. 1.60 on page 15. The terms $|r_p|^2 \cos 2A \cos 2P$ and $|r_s|^2 \sin 2A \sin 2P$ give no information about Δ. The third term can be written as

$$\overline{r}_p\overline{r}_s^* + \overline{r}_p^*\overline{r}_s = 2|\overline{r}_p||\overline{r}_s| \cos\Delta. \tag{5.10}$$

This is the point where cosΔ is obtained directly leaving no information about the sign of Δ. This “sign problem” is not critical when measuring on a sample for which the approximate value of cosΔ is known, and its sign doesn't change in the used spectrum. This assumption holds for thin layers in the most cases. Fig. 5.4 shows the measured and corrected spectra with the fitted curve for a thin silicon oxide layer on a single-crystalline silicon bulk. For thin layers like this, no oscillation of the cosΔ curve can be observed. Furthermore, Δ doesn't change its sign. The correction causes a parallel shift of the measured curve. The fit to the corrected curve is very good in the whole spectrum.

For thick layers, the interference in the layer causes an oscillation of cosΔ, and Δ may change the sign for many times. If the sing changes, the correction $\Delta_s = \Delta_m - \Delta_p$ have to be changed to $\Delta_s = \Delta_p - \Delta_m$. It is enough to know the sign at only one point in the spectrum, and the points, where the sign changes. Δ changes the sign at that points, where the spectrum reaches 1 or -1. Unfortunately, the precision of the measurement is the worst just at these points. As a result, the automatic detection of these places is very complicated. CosΔ may get close to 1 or -1, but in spite of this, doesn't change the sign. It is not obvious, how close should cosΔ be to 1 or -1 to regard this point as the place where the sign changes.

A possible method to determine the sign of Δ is the use of the Kramers-Kroenig relation [Pie93a]. In the general case of a complex function, if this function is analytic, we can deduce the imaginary part from the real part or the real part from the imaginary part. The complex reflectance ratio can be written as

$$\overline{\rho} = \tan\Psi e^{i\Delta} = \tan\Psi\cos\Delta + i\tan\Psi\sin\Delta. \tag{5.11}$$

Knowing $\tan\Psi\cos\Delta$, $\tan\Psi\sin\Delta$ can be calculated, and the sign of Δ can be determined. The precision of the method is limited by the fact that the values outside the measured range have to be approximated. So precise determination of the

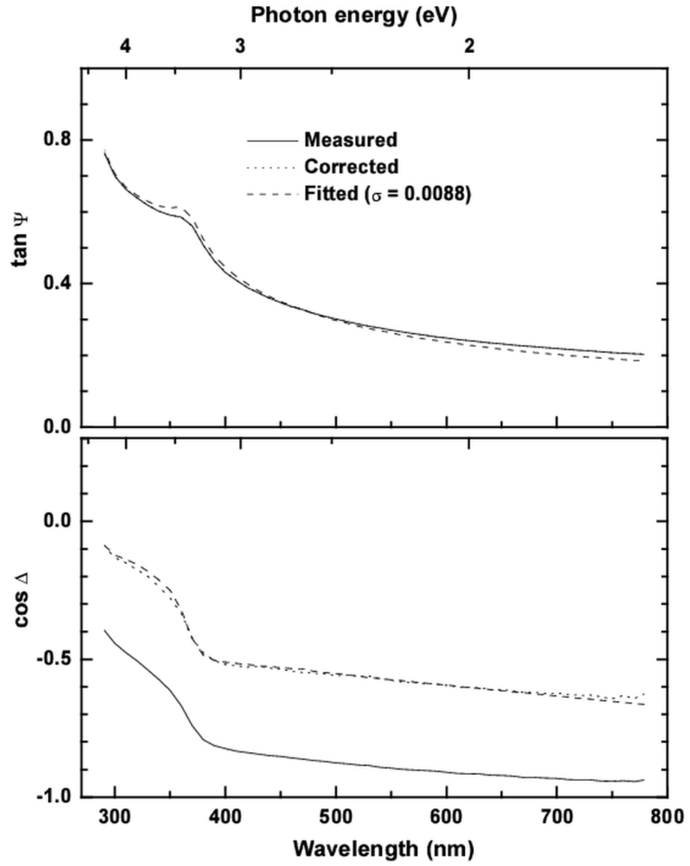

Figure 5.4. Measurement on a sample having a silicon oxide layer on a single-crystalline silicon substrate. The corrected spectra are also shown together with the fitted curve. The measured oxide thickness was 22.62±0.084 nm.

imaginary part is not possible, but the sign of Δ can be calculated if the wavelengths are determined where the sign changes. It means that neither this method gives a solution for the problem of the determination of the points where the sign changes.

Accurate determination of the sign can be performed by using a compensator. The sign of Δ can be determined by two subsequent measurements at different compensator positions. A significant disadvantage of this method is that it reduces the measurement speed and makes the hardware more complicated. Another possibility is to use a rotating compensator [Hau80, Lee98].

5.3 Measurements at high temperature

At the FhG-IIS-B the measurement software was modified to take into account the phase shift of the prisms. The program uses the stored $\cos\Delta_p$ spectrum taken on a glass sample to automatically correct the measured values (eqn. 5.9). Using a special program, the $\cos\Delta$ spectrum is converted to a calibration file, which can be easily used by the measurement software. For test and development, another software was written, which corrects the spectra measured by the *in situ* ellipsometer using the $\cos\Delta_p$ spectrum taken for the calibration. This software was written in C++ code and operates in command mode. As an input it requires the $\tan\Psi$–$\cos\Delta$ spectrum measured on the sample and the glass, furthermore, the wavelengths where the sign changes and the sign at the beginning of the spectrum.

The correction was tested by comparing the results with that of the ex situ scanning ellipsometer. Table 5.1 shows the layer thicknesses measured by the *in situ* ellipsometer with the beam guiding system and by the *ex situ* scanning ellipsometer without the beam guiding system. The difference between the results of the two ellipsometers is typically between 0.2 nm and 0.4 nm except for the thickest layers. The low confidence limits obtained also by the *in situ* ellipsometer shows that the agreement between the measured and fitted curves is very good for the corrected curves as well.

Table 5.1. Comparison of the layer thicknesses values of silicon dioxide and silicon nitride thin films measured by the *in situ* ellipsometer with the beam guiding system and by the *ex situ* scanning ellipsometer.

Sample	*ex situ* ellipsometer		*in situ* ellipsometer	
	Thickness (nm)	σ (10^{-2})	Thickness (nm)	σ (10^{-2})
NBS calibration standard 22 nm silicon dioxide	22.16±0.06	0.46	22.62±0.08	0.89
NBS calibration standard 57 nm silicon dioxide	57.83±0.06	0.90	57.63±0.03	0.41
Native oxide	1.32±0.06	0.40	1.13±0.07	0.29
44 nm silicon nitride	44.49±0.06	1.94	44.79±0.05	3.20
84 nm silicon nitride	84.20±0.08	6.89	83.80±0.12	1.87
368 nm silicon nitride	368.33±0.49	9.84	365.66±0.19	6.20

The most important information for *in situ* measurements is the refractive index of the silicon substrate at process temperature. Therefore, measurements have been made, in order to determine the dielectric function of the single-crystalline silicon at high temperature. The wafers were directly introduced from the manufacturer's package to the vertical furnace. They were measured first at room temperature in order to determine the thickness of the native oxide layer and the angle of incidence. To avoid a measurement error caused by a possible oxide growth at high temperatures, the wafers were heated to the highest temperatures, and the temperature was decreased step by step for the subsequent measurements. The calibration files ($\cos\Delta_p$) for the phase shift of the prisms were taken at all used temperatures. The thickness of the native oxide was measured also after the high temperature measurements. The refractive index of the substrate was calculated taking into account the thickness of the native oxide layer. Since the temperature dependence of the refractive index of the single-crystalline silicon ($\Delta n \approx 0.15$ between 20°C and 450°C) is much higher than that of the native oxide layer ($\Delta n \approx 0.003$ between 20°C and 450°C), the temperature dependence of the latter was neglected.

Temperature dependence of the dielectric function of silicon have been studied by several authors [Lau87, Vuy93, Jel94]. A detailed study was made by Vuye et al. [Vuy93] in the range from 20°C to 450°C. We completed this results with measure-

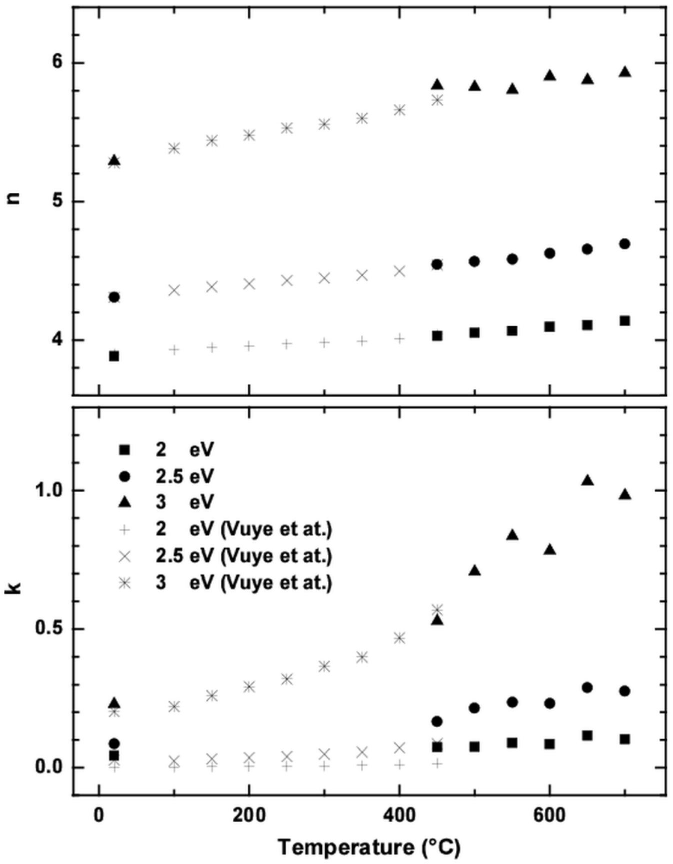

Figure 5.5. Real (n) and imaginary (k) part of the refractive index of single-crystalline silicon at 2, 2.5, and 3 eV as a function of temperature. For comparison the data measured by Vuye et al. [Vuy93] are also plotted.

ments over 450°C - 700°C in 50°C steps. (To be able to compare our results with that of Vuye et al., we measured also at the temperature of 450°C.) Fig. 5.5 shows the real (n) and imaginary (k) parts of the refractive index of single-crystalline silicon at 2, 2.5, and 3 eV as a function of temperature measured by the *in situ* ellipsometer. For comparison the data measured by Vuye et al. [Vuy93] are also plotted. There is a very good agreement for the real part of the refractive index at all energies.

At 450°C, the difference in n between our measurement and that of Vuye et al. is less than 0.011 and 0.003 at 2 eV and 2.5 eV, respectively. In the low energy region (below 3 eV), the imaginary part of the refractive index is very small. The value k is calculated mainly from cosΔ that is near -1 in this case, where the accuracy of the measurement is very low. This is the reason for the significant difference in k at 2 eV and 2.5 eV between our measurements and that of Vuye et al.

5.4 Annealing of amorphous silicon samples

Monitoring of the crystallization of amorphous silicon was carried out during annealing of amorphous silicon-on-oxide samples in the vertical furnace with the beam guiding system. The structure of the samples is shown in Fig. 5.6. The samples were prepared by thermal oxidization of single-crystal, (100) oriented, 7-21 Ωcm, p-type

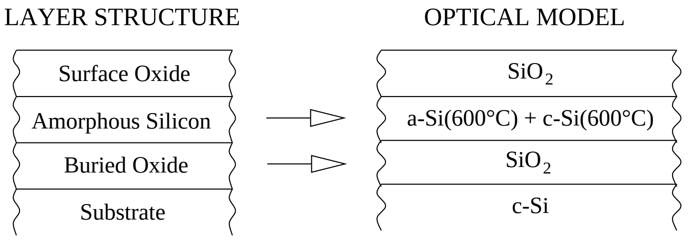

Figure 5.6. Layer structure and optical model used for *in situ* measurements.

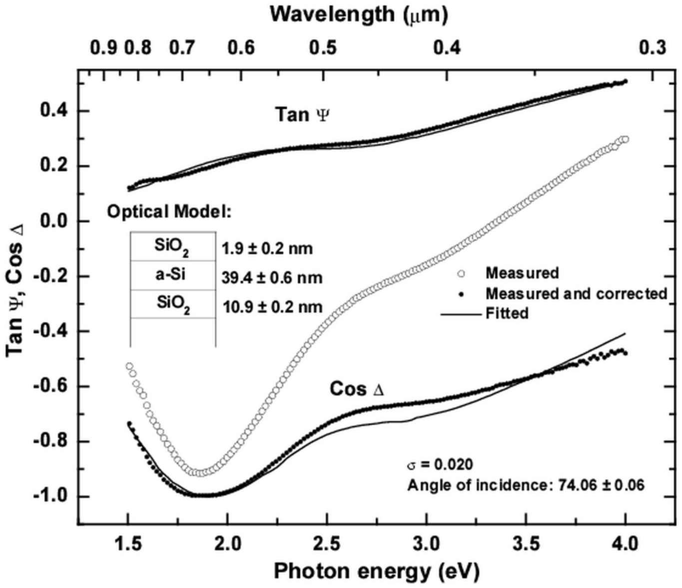

Figure 5.7. Measured, corrected (eqn. 5.4), and fitted ellipsometry spectra on a thin amorphous silicon-on-oxide sample together with the optical model and the best fit parameters. The measurement was taken at room temperature inside the vertical furnace before annealing.

silicon samples, to have an approximately 10 nm silicon dioxide layer, followed by LPCVD deposition of amorphous silicon layers at a pressure of 0.33 mbar, gas flow of 50 sccm, and deposition temperature of 560°C.

The batch furnace used in the measurements is not designed for rapid heating. The max. ramp-rate is 20°C/min. Therefore, the insertion of the samples in the process chamber with a pure nitrogen atmosphere was performed at 530°C. Test measurements showed that no structural change at this temperature occurs. From this temperature, the furnace was ramped to 600°C. The measurement was started at the beginning of the ramp up and the spectra were taken continuously for 71 minutes in 16 second steps. The precision of the temperature measurement was 0.1°C.

Fig. 5.7 shows the spectra measured using the beam guiding system at room temperature before loading the wafers in the vertical furnace. The corrected (eqn. 5.9) and fitted spectra are also plotted showing that the correction works well: σ, which represents the fit quality, is low. Generally, a sigma value below 0.05 represents a good fit quality. In our case σ=0.02 (see Fig. 5.7). No correction is needed for tanΨ, so the measured and corrected spectra coincide for tanΨ. The optical model used for the fit is shown in the insert of the figure. The model consists of a surface oxide layer,

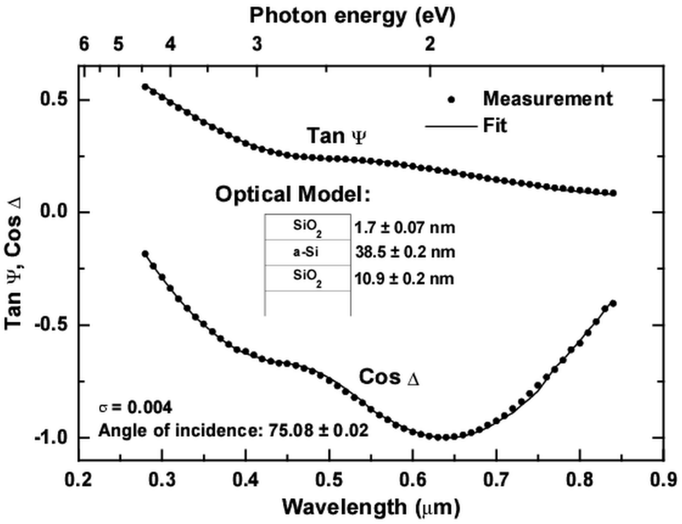

Figure 5.8. Measured and fitted ellipsometry spectra taken at the reference ellipsometer (SOPRA ES4G) on the same sample as in Fig. 5.7. The optical model parameters are shown in the insert for comparison with that of Fig. 5.7.

a thin amorphous silicon layer and a buried oxide layer. The reference data for the amorphous silicon (a-Si) was taken from Ref. [Jel93]. The thickness of the surface oxide, the amorphous layer and the buried oxide layer can be determined with an uncertainty of 0.2, 0.6, and 0.2 nm, respectively, which also shows the reliability of the optical model. The angle of incidence could also be obtained from the fit with a low uncertainty. For the measurements during annealing this value was used as a reference and was not fitted.

For comparison, the same sample was measured on a reference ellipsometer as well (SOPRA ES4G). The measured curves and the fit result are shown in Fig. 5.8. The differences of the layer thicknesses determined by the *in situ* and the *ex situ* ellipsometers (see the model parameters shown in Figures 5.7 and 5.8) are within 1 nm. The difference is only 0.2 nm for the surface oxide.

Figure 5.9 shows the measured spectra during annealing at 600°. There is a systematic shift of tanΨ and cosΔ to lower values, which is greater for cosΔ.

The measured spectra were fitted using the optical model shown in Fig. 5.6. The high-temperature reference data for single-crystalline silicon (denoted as c-Si(600°C) in Fig. 5.6) were taken from [Leh98a]. The dielectric function data for amorphous silicon at 600°C (denoted as a-Si(600°C) in Fig. 5.6) was measured in the vertical furnace using an “amorphous silicon-on-oxide” sample with an amorphous silicon layer thickness of ≈500 nm. The determination of the dielectric function was performed in the spectral range from 2 to 3.5 eV. In this range, the optical penetration depth of the light in amorphous silicon is less than 500 nm (see Fig. 1.9), so the layer can be regarded as a bulk. The error caused by the surface oxide was corrected using [Asp82]

$$\overline{\epsilon} = \epsilon_s + \frac{4\pi i d n_a}{\lambda} \frac{\epsilon_s(\epsilon_s - \epsilon_\circ)(\epsilon_\circ - \epsilon_a)}{\epsilon_\circ(\epsilon_s - \epsilon_a)} \left(\frac{\epsilon_s}{\epsilon_a} - \sin^2 \Phi \right)^{\frac{1}{2}}, \tag{5.12}$$

where $\overline{\epsilon}$ is the effective dielectric function, $\epsilon_\circ$ and d are the dielectric function and the thickness of the over-layer, respectively, ϵ_s and ϵ_a pertain to substrate and ambient,

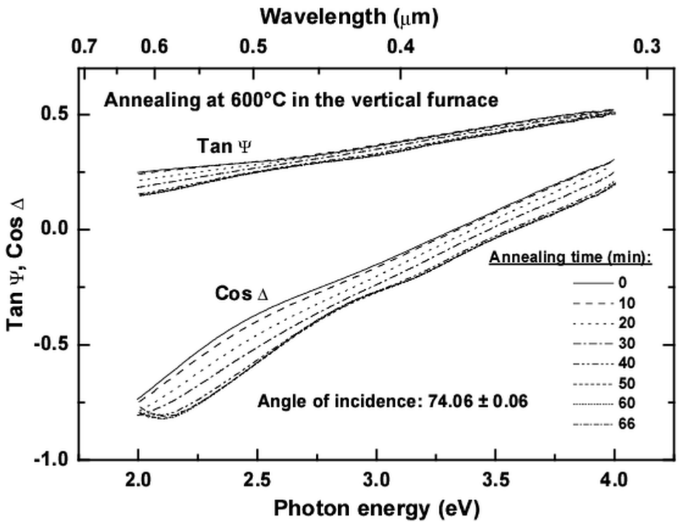

Figure 5.9. Measured spectra of thin amorphous silicon-on-oxide sample during annealing in the vertical furnace at 600°C.

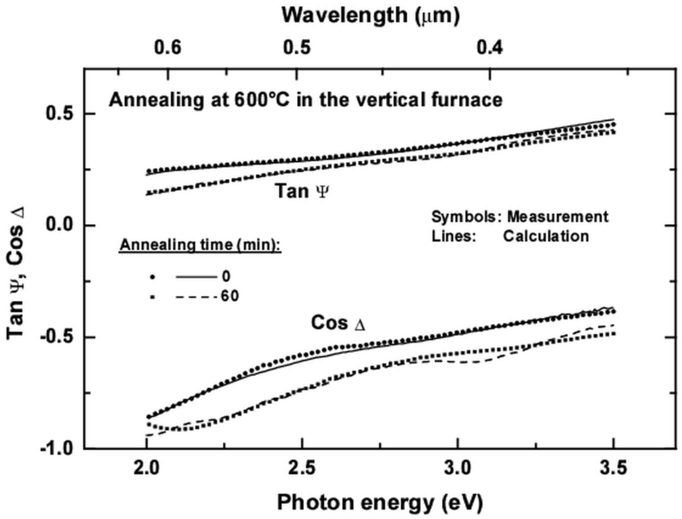

Figure 5.10. Fit results for the annealed samples at the beginning and at the end of the annealing.

respectively, λ is the wavelength of the light, and Φ is the angle of incidence. The only unknown value, which we are looking for, is the true dielectric function of the substrate: ϵ_s. The thickness of the silicon dioxide over-layer can be measured independently on the reference ellipsometer (SOPRA ES4G) or before heating up in the vertical furnace.

The effective dielectric function was calculated using the B-EMA (see Section 1.1.3), which is used extensively for the investigation of crystallization processes [Shi97, Kuo97]. Fig. 5.10 shows the fit results for the annealed samples at the beginning and at the end of the annealing. The fit was made in a limited spectral range, because the a-Si reference spectra for 600°C was available only in this range. The increased difference between the measured and fitted curves for cosΔ at the end of annealing (t = 60 min) near the E_1 inter-band transition (≈3.4 eV, see Fig. 2.2) shows that the model using a combination of the reference dielectric function of single-crystalline

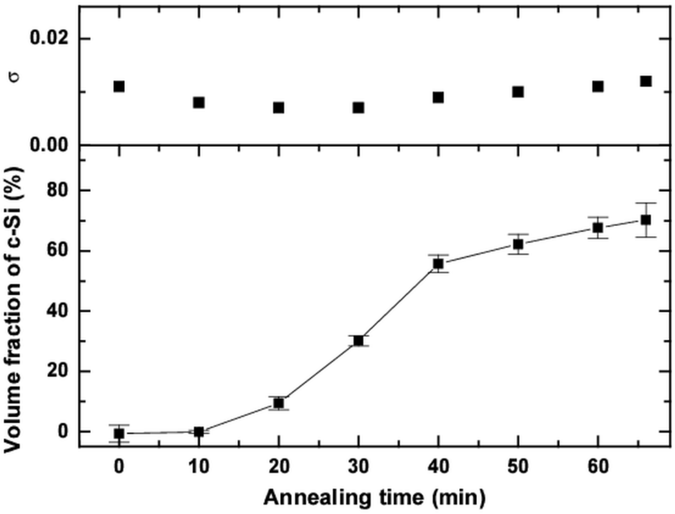

Figure 5.11. Volume fraction of the crystalline silicon in the optical model as a result of fit on the measurements during annealing shown in Fig. 5.9.

and amorphous silicon doesn't apply well for the resulting polycrystalline structure (as discussed in Section 2.2).

Fig. 5.11 shows the volume fraction of the crystalline silicon and the σ values as a function of the annealing time. The crystallization ends up with a c-Si fraction of 71% after 66 minutes of annealing. It is fastest in the range between 20 and 40 minutes.

For thick layers, the interference in the layer causes an oscillation of cosΔ, and Δ may change the sign for many times. The difficulty of the determination of the position where the sign changes decreases the precision of the measurement (see Section 5.2). On the other hand, measurement of thick samples allows the determination of high temperature dielectric function in a spectral range, where the optical penetration depth is smaller than the layer thickness. In this spectral range the layer can be regarded as a bulk sample. After determination of the dielectric function for bulk, only the error caused by the thin surface oxide layer has to be eliminated using equation 5.12.

Raw ellipsometry spectra of a thick ($\approx$500 nm) amorphous silicon sample annealed at 600°C in the vertical furnace are shown in Fig. 5.12 together with reference measurements taken at the SOPRA ES4G ellipsometer before and after annealing. In the spectral range above $\approx$2.4 eV the spectra are smooth. For these photon energies the layer can be regarded as a bulk. In this part of the spectra, a systematic decrease with annealing time for both tanΨ and cosΔ can be observed. The intensity of the signal measured by the *in situ* ellipsometer (MOSS-OMA) is very weak above $\approx$3.5 eV. There is a significant noise in this range especially for cosΔ. The part of the spectra below 2.4 eV is oscillating making the correction difficult (Section 5.2). As a result, the spectral range between 2.5 and 3.5 eV is used for fitting the spectra. As for these photon energies the penetration depth of the light is less than the layer thickness, this method allows the use of a simple optical model.

Figure 5.13 shows measured and fitted ellipsometry spectra for selected annealing times using two different optical models. The models have only one layer, because for the used photon energies the amorphous silicon layer can be regarded as a bulk sample.

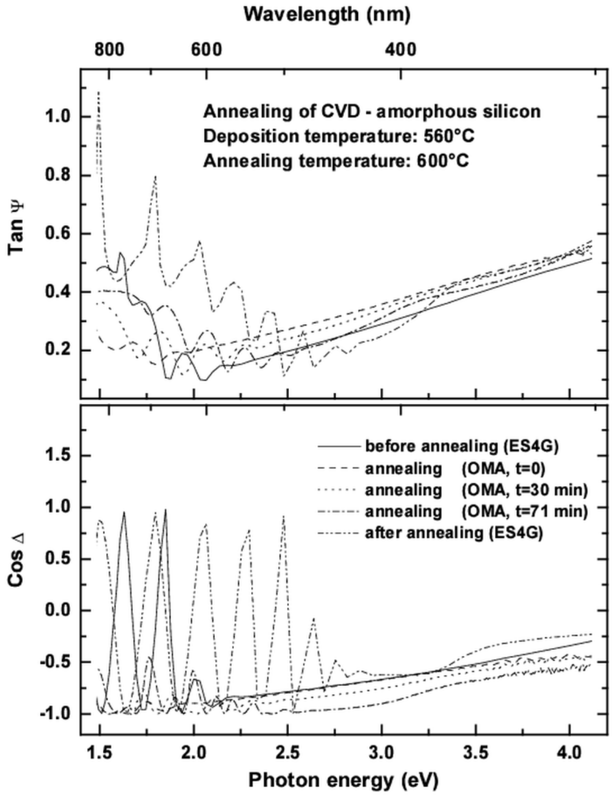

Figure 5.12. Ellipsometry spectra of thick (≈500 nm) amorphous silicon sample annealed at 600°C in the vertical furnace together with reference measurements (before annealing and after annealing) taken at the SOPRA ES4G ellipsometer.

In Model 1 (see the insert in Fig. 5.13), the crystallizing polysilicon layer is represented by a combination of the high-temperature reference data for c-Si and a-Si as used above. For Model 2, the high-temperature reference data for a-Si (denoted as a-Si(600°C) in the insert for Model 2) and pc-Si (denoted as pc-Si(600°C)) are calculated from the measurements made just at the beginning and at the end of the annealing, respectively. In the used spectral range, the dielectric function data can be calculated by regarding the sample as bulk, followed by a correction for the error, caused by the thin surface oxide over-layer, using the same procedure as described above (eqn. 5.12). Fig. 5.14 shows the dielectric function data calculated this way, used as references for Model 2 (a-Si-600c, pc-Si-600c), together with the room temperature reference data for single-crystalline silicon (c-Si, [Asp85]), fine-grained polycrystalline silicon (pc-Si, [Jel93]), amorphous silicon (a-Si, [Jel93]), and high-temperature reference data for single-crystalline silicon (c-Si-600, [Leh98a, Leh98b]). The change caused by the correction for the error from the oxide over-layer (a-Si-600 ⇒ a-Si-600c, pc-Si-600 ⇒ pc-Si-600c) is significant for both a-Si-600 and pc-Si-600, especially for tanΨ in the higher photon energy range. Compared with the room temperature data (pc-Si-600c ⇔ pc-Si), pc-Si-600c is shifted towards lower energies with respect to pc-Si. The effect is similar as for the single-crystalline data (c-Si-600 ⇔ c-Si): the spectrum is shifted to lower energies with increasing temperature, but the hight of the peak is decreased in this case, while it remains the same in case of pc-Si ⇒ pc-Si-600.

Fitted model parameters using Model 2 of Fig. 5.13 are shown in Table 5.2 as a

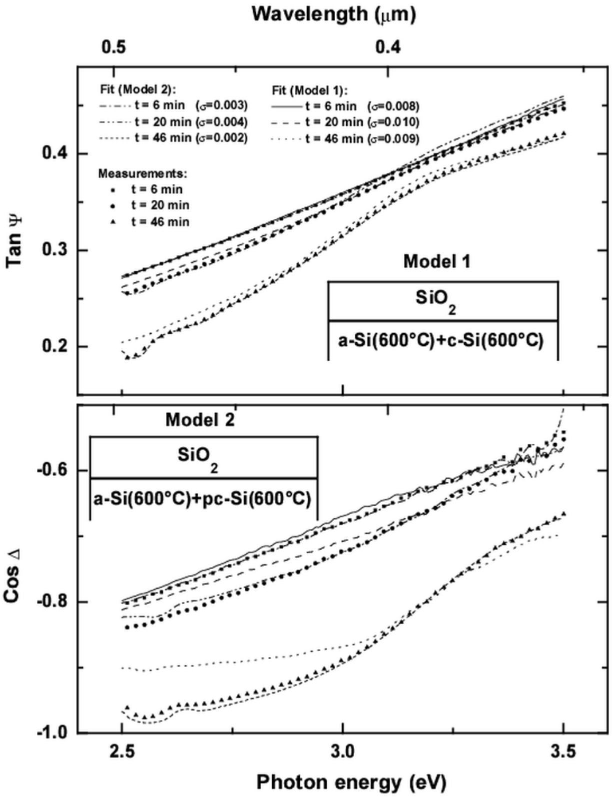

Figure 5.13. Ellipsometry spectra of thick (≈500 nm) amorphous silicon samples annealed at 600°C in the vertical furnace together with fitted spectra using two different optical models shown in the insert.

function of the annealing time. The crystallization process can be monitored by the change of the a-Si and pc-Si components in the optical model. The σ values are 0.004 or below for all annealing times, while using Model 1 it has values between 0.008 and 0.010 as shown in Fig. 5.13. The fitted curves show also a big deviation from the measured ones when using Model 1, while much better fit results are obtained in case of Model 2. To check the reliability of the fitting procedure, the thickness of the surface oxide was also fitted, showing similar values for all annealing times (Table 5.2).

Table 5.2. Fitted model parameters as functions of annealing time.

Annealing time (min)	a-Si (%)	pc-Si (%)	Oxide thickness (nm)	σ
0	98.2±1.8	1.8	1.3±0.1	0.003
6	97.4±1.7	2.6	1.2±0.1	0.003
13	96.1±2.1	3.9	1.4±0.2	0.004
20	80.1±2.3	19.9	1.5±0.2	0.004
26	54.5±2.4	45.5	1.8±0.1	0.004
33	29.8±2.4	70.2	1.8±0.1	0.003
39	12.6±2.0	87.4	1.7±0.1	0.003
46	2.4±1.0	97.6	1.6±0.1	0.002
52	0.2±0.2	99.8	1.5±0.1	0.001
59	0.1±0.1	99.9	1.3±0.1	0.001

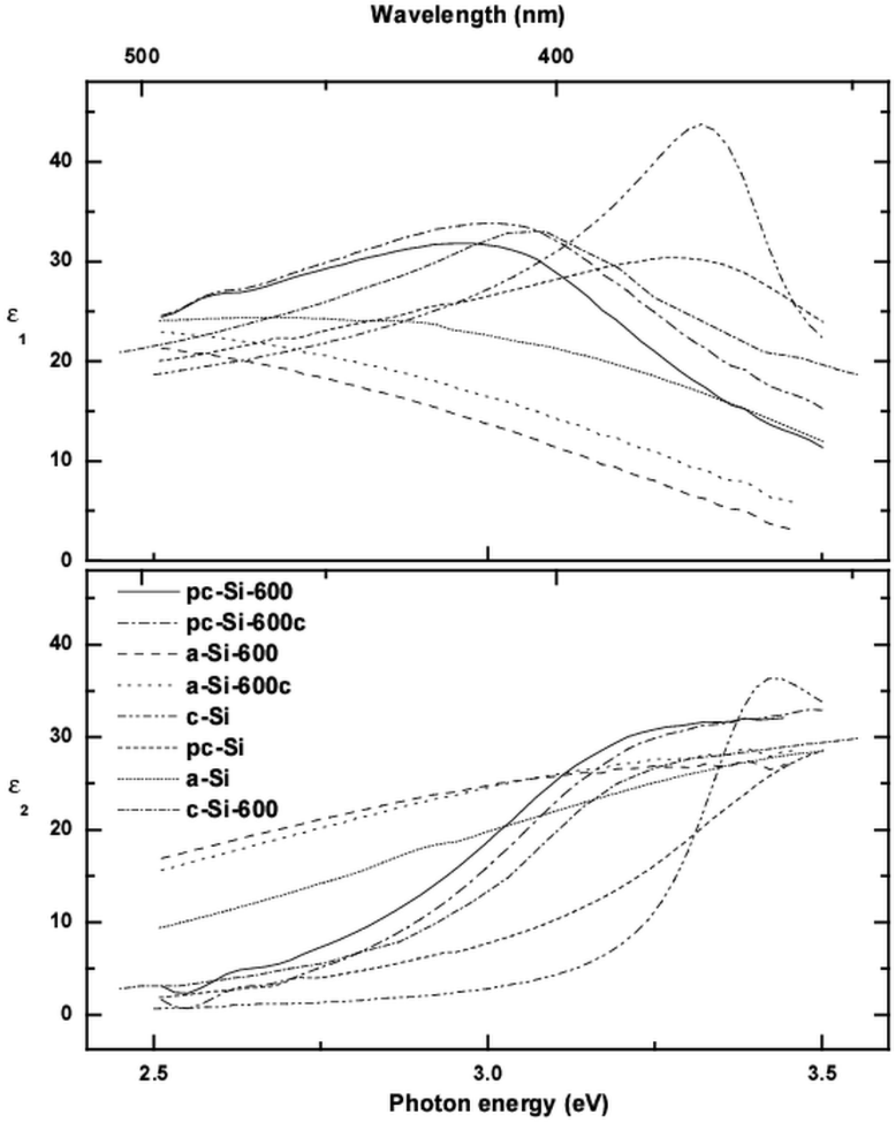

Figure 5.14. Dielectric function reference data used for the calculations. a-Si-600 and pc-Si-600 were measured at 600°C before and after the annealing, respectively. a-Si-600c and pc-Si-600c are the corrected data, taking into account a thin surface oxide layer. The reference data of single-crystalline silicon (c-Si, [Asp85]), amorphous silicon (a-Si, [Jel93]), fine-grained polycrystalline silicon (pc-Si, [Jel93]), and high-temperature reference data for single-crystalline silicon (c-Si-600, [Leh98a, Leh98b]) are also plotted for comparison.

Bibliography

[An90] An I., Nguyen H. V., Collins R. W.: *Microstructural Evolution of Ultrathin Amorphous Silicon Films by Real-Time Spectroscopic Ellipsometry. Phys. Rev. Lett.*, **65**, 2274 (1990).

[An91] An I., Cong Y., Nguyen N. V., Pudliner B. S., Collins R. W.: *Instrumentation Considerations in Multichannel Ellipsometry for Real-Time Spectroscopy. Thin Solid Films*, **206**, 300 (1991).

[Asi93] Asinovsky L. M.: *Optimization of the Polycrystalline Silicon-On-Silicon Dioxide Characterization Using Spectroscopic ellipsometry. Thin Solid Films*, **233**, 210 (1993).

[Asp74] Aspnes D. E.: *Effects of Component Optical Activity in Data Reduction and Calibration of Rotating-Analyzer Ellipsometers. J. Opt. Soc. Am.*, **64**, 812 (1974).

[Asp79] Aspnes D. E., Theeten J. B., Hottier F.: *Investigation of Effective-Medium Models of Microscopic Surface Roughness by Spectroscopic Ellipsometry. Phys. Rev. B*, **20**, 3292 (1979).

[Asp81] Aspnes D. E.: *Microstructural Information from Optical Properties in Semiconductor Technology. SPIE Proc.*, **276**, 312 (1981).

[Asp82] Aspnes D. E.: *Optical Properties of Thin Films. Thin Solid Films*, **89**, 249 (1982).

[Asp84] Aspnes D. E., Studna A. A., Kinsbron E.: *Dielectric Properties of Heavily Doped Crystalline and Amorphous Silicon from 1.5 to 6.0 eV. Phys. Rev. B*, **29**, 768 (1984).

[Asp85] Aspnes D. E.: *The Accurate Determination of Optical Properties by Ellipsometry.* In Palik E. D., editor, *Handbook of Optical Constants of Solids*, Academic Press, New York, 1985.

[Azz87] Azzam R. M. A., Bashara N. M.: *Ellipsometry and Polarized Light.* Elsevier, 1987.

[Bag81] Bagley B. G., Aspnes D. E., Adams A. C., Mogab C. J.: *Optical Properties of Low-Pressure Chemically Vapor Deposited Silicon Over the Energy Range 3.0-6.0 eV. Appl. Phys. Lett.*, **38**, 56 (1981).

[Bau96] Bauer G., Richter W.: *Optical Characterization of Epitaxial Semiconductor Layers.* Springer Verlag, Berlin, 1996.

[Ber94] Berger R., Petrik P., Schneider C., Neumann W., Stehlé J.-L.: *In situ Monitoring of Layer Growth in Conventional Vertical Furnaces by Spectroscopic Ellipsometry. Workshop International on Spectroscopic Ellipsometry, Erlangen* (1994).

[Bir96] Biró L. P., Gyulai J., Havancsák K., Didyk A. Y., Bogen S., Frey L.: *Use of Atomic-Force Microscopy and a Parallel Irradiation Geometry for In-Depth Characterization of Damage Produced by Swift Kr Ions in Silicon. Phys. Rev. B*, **54**, 11853 (1996).

[Bor68] Born M., Wolf E.: *Principles of optics.* Pergamon Press, London, 1968.

[Bou92] Boultadakis S., Logothetidis S., Ves S.: *Comparative Study of Thin Poly-Si Films Grown by Ion Implantation and Annealing with Spectroscopic Ellipsometry, Raman Spectroscopy, and Electron Microscopy. J. Appl. Phys.*, **72**, 364 (1992).

[Bár94] Bársony I., Klappe J. G. E., Vázsonyi É., Lohner T., Fried M.: *Rapid Thermal Oxidation for Passivation of Porous Silicon. Mat. Res. Soc. Symp. Proc.*, **342**, 91 (1994).

[Bru35] Bruggeman D. A. G.: *Berechnung verschiedener physikalischer Konstanten von heterogenen Substanzen I. Dielektrizitätskonstanten und Leitfähigkeiten der Mischkörper aus isotropen Substanzen. Ann. Phys. (Lepzig)*, **24**, 636 (1935).

[Bru72] Brusic V., Genshaw M. A., Bockris J. O.: *On the Possible Influence of Surface Roughening on Ellipsometric Data in Electrochemical Studies. Surf. Sci.*, **29**, 653 (1972).

[Chu78] Chu W.-K., Mayer J. W., Nicolet M.-A.: *Backscattering Spectrometry.* Academic Press, 1978.

[Cof98] Coffa S., Meyyappan M., Nishi H.: *Materials and Technology challenges in Semiconductor Processing. Materials Science in Semiconductor Processing*, **1**, 1 (1998).

[Col89] Collins R. W., Yang B. Y.: *In Situ Ellipsometry of Thin-Film Deposition: Implications for Amorphous and Microcrystalline Si Growth. J. Vac. Sci. Technol.*, **B7**, 1155 (1989).

[Col93] Collins R. W., An I., Nguyen H. V., Lu Y.: *Real Time Spectroscopic Ellipsometry for Characterization of Nucleation, Growth, and Optical Functions of Thin Films. Thin Solid Films*, **233**, 244 (1993).

[Coo63] Cook N. H., Rabinowicz E.: *Physical Measurement and Analysis.* Addison-Wesley, 1963.

[dN89] de Nijs J.: *Ellipsometry and the Ti/c-Si Solid State Reaction.* PhD Thesis, 1989.

[Dru89a] Drude P.: *Oberflächenschichten. Ann. Phys. Chem.*, **36**, 532 (1889).

[Dru89b] Drude P.: *Oberflächenschichten. Ann. Phys. Chem.*, **36**, 865 (1889).

[Dru90] Drude P.: *Bestimmung der optischen Constanten der Metalle. Ann. Phys. Chem.*, **39**, 481 (1890).

[Erm83] Erman M., Theeten J. B.: *Analysis of Ion-Implanted GaAs by Spectroscopic Ellipsometry. Surface Science*, **135**, 353 (1983).

[Fan96] Fang S. J., Chen W., Yamanaka T., Helms C. R.: *Comparison of Si Surface Roughness Measured by Atomic Force Microscopy and Ellipsometry. Appl. Phys. Lett.*, **68**, 2837 (1996).

[Fel82] Feldman L. C., Mayer J. W., Picraux S. T.: *Materials Analysis by Ion Channeling.* Academic Press, NY, 1982.

[Fen69] Fenstermaker C., McCrackin L.: *Errors Arising from Surface Roughness in Ellipsometric Measurement of the Refractive Index of a Surface. Surf. Sci.*, **16**, 85 (1969).

[Flu96a] Flueraru C., Gartner M., Dascalu D., Rotaru C.: *Spectroellipsometric Investigation of LPCVD Polysilicon: As Deposited and After Hydrogenation. J. Phys. III France*, **6**, 225 (1996).

[Flu96b] Flueraru C., Gartner M., Rotaru C., Dascalu D., Andriescu G., Cosmin P.: *Spectro-Ellipsometric Investigations of Polycrystalline Silicon Surface Roughness. Microelectronic Engineering*, **31**, 309 (1996).

[Fri84] Fried M., Lohner T., Jároli E., Mezey G. V. G., Gyulai J.: *Investigation of Ion-Implanted Semiconductors by Ellipsometry and Backscattering Spectrometry. Thin Solid Films*, **116**, 191 (1984).

[Fri85] Fried M.: *Ion implantáció hatásának vizsgálata Si-on és GaP-on ellipszometriával és ion-visszaszórásos spektrometriával.* PhD thesis, KFKI, 1985.

[Fri89] Fried M., Lohner T., de Nijs J. M. M., van Silfhout A., Hanekamp L. J., Laczik Z., Khánh N. Q., Gyulai J.: *Non-destructive Characterization of Nitrogen-Implanted Silicon-on-Insulator Structures by Spectroscopic Ellipsometry. J. Appl. Phys.*, **66**, 5052 (1989).

[Fri91] Fried M., Lohner T., Jároli E., Hajdu C., Gyulai J.: *Non-Destructive Determination of Damage Depth Profiles in Ion-Implanted Semiconductors by Multiple-Angle-of-Incidence Single-Wavelength Ellipsometry. Nucl. Instr. Meth. B*, **55**, 257 (1991).

[Fri92a] Fried M., Lohner T., Aarnink W. A. M., Hanekamp L. J., van Silfhout A.: *Determination of Complex Dielectric Functions of Ion-Implanted and Implanted-Annealed Silicon by Spectroscopic Ellipsometry. J. Appl. Phys.*, **71**, 5260 (1992).

[Fri92b] Fried M., Lohner T., Aarnink W. A. M., Hanekamp L. J., van Silfhout A.: *Nondestructive Determination of Damage Depth Profiles in Ion-Implanted Semiconductors by Spectroscopic Ellipsometry using Different Optical Models. J. Appl. Phys.*, **71**, 2835 (1992).

[Fri97] Fried M., Lohner T., Gyulai J.: *Ellipsometric Analysis.* In Cristofides C., Ghibaudo G., editors, *Effect of Disorder and Defects in Ion-Implanted Semiconductors: Optical and Photothermal Characterization*, Semiconductors and Semimetals, Academic Press, New York, 1997.

[Fri98] Fried M., Wormeester H., Zoethout E., Lohner T., Polgár O., Bársony I.: *In Situ Spectroscopic Ellipsometric Investigation of Vacuum Annealed and Oxidized Porous Silicon Layers. Thin Solid Films*, **313-314**, 459 (1998).

[Fuj97] Fujiwara H., Koh J., Wronski C. R., Collins R. W.: *Application of Real Time Spectroscopic Ellipsometry for High Resolution Depth Profiling of Compositionally Graded Amorphous Silicom Alloy Thin Films. Appl. Phys. Lett*, **70**, 2150 (1997).

[Gau85] Gautard D., Laporte J. L., Cadoret M., Pariset C.: *Ellipsometric Study of Surface Treatments Carried out on {100} InP Inside a VPE Reactor. J. Cryst Growth*, **71**, 125 (1985).

[Ger71] Gergely G.: *Ellipsometric Tables of the Si-SiO$_2$ System for Mercury and He-Ne Laser Spectral Lines.* Akadémiai Kiadó, Budapest, 1971.

[Ger88] Gergely G., Bodó Z.: *Determination of the Optical Constants of Metals and Semiconductors by Combining Ellipsometry With Electron Spectroscopy Microscopy and X-ray Specular Reflection analysis. Surface Science*, **200**, 527-535 (1988).

[Gyu85] Gyulai J., Mezey G.: *Felületek és vékonyrétegek vizsgálata MeV energiájú ionokkal.* In Siklós T., editor, *A szilárdtestkutatás újabb eredményei*, vol. 14, Akadémiai Kiadó, Budapest, 1985.

[Ham90] Hammond M. L.: *Poly-Si – a Most Important Material. Mat. Res. Soc. Symp. Proc.*, **182**, 3 (1990).

[Hau73] Hauge P. S., Dill F. H.: *Design and Operation of ETA, an Automated Ellipsometer. IBM Journal of Research and Development*, **17**, 472 (1973).

[Hau80] Hauge P. S.: *Recent Developments in Instrumentation in Ellipsometry. Surface Science*, **96**, 108 (1980).

[Hol86] Holtslag T.: *Noble-Gas Ion Bombardment on Clean Silicon Surfaces Studied Using Ellipsometry and Desorption.* WEKA Enschede, 1986.

[Hot79] Hottier F., Theeten J. B.: *Surface Analysis During Vapour Phase Growth. J. Cryst. Growth*, **48**, 644 (1979).

[Hot81] Hottier F., Cadoret R.: *Surface Processes in Low Pressure Chemical Vapour Deposition. J. Cryst. Growth*, **52**, 199 (1981).

[Ibo93] Ibok E., Garg S.: *A Characterization of the Effect of Deposition Temperature on Polysilicon Properties. J. Electrochem. Soc.*, **140**, 2927 (1993).

[Ire93] Irene E. A.: *Applications of Spectroscopic Ellipsometry to Microelectronics. Thin Solid Films*, **233**, 96 (1993).

[Jel93] Jellison G. E., Jr. , Chisholm M. F., Gorbatkin S. M.: *Optical Functions of Chemical Vapor Deposited Thin-Film Silicon Determined by Spectroscopic Ellipsometry. Appl. Phys. Lett.*, **62**, 348 (1993).

[Jel94] Jellison G. E., Jr. , Modine F. A.: *Optical Functions of Silicon at Elevated Temperatures. J. Appl. Phys.*, **76**, 3758 (1994).

[Kam78] Kamins T. I., Mandurah M. M., Saraswat K. C.: *Structure and Stability of Low Pressure Chemically Vapor-Deposited Silicon Films. J. Electrochem. Soc.*, **125**, 927 (1978).

[Kam80] Kamins T. I.: *Structure and Properties of LPCVD Silicon Films. J. Electrochem. Soc.*, **127**, 686 (1980).

[Khá88] Khánh N. Q., Fried M., Battistig G., Laczik Z., Lohner T., Jároli E., Schiller V., Gyulai J.. *Physica Status Solidi (a)*, **108**, K35 (1988).

[Koh99] Koh J., Fujiwara H., Koval R. J., Wronski C. R., Collins R. W.: *Real Time Spectroscopic Ellipsometry Studies of the Nucleation and Growth of p-Type Microcrystalline Silicon Films on Amorphous Silicon using B_2H_6, $B(CH_3)_3$ and BF_3 Dopant Source Gases. J. Appl. Phys.*, **85**, 4141 (1999).

[Kót94] Kótai E.: *Computer Methods for Analysis and Simulation of RBS and ERDA Spectra. Nucl. Instr. and Meth.*, **B85**, 588 (1994).

[Kuo97] Kuo C.-H., Hsieh I.-C., Schroeder D. K.: *Ex Situ Ellipsometry Characterization of Eximer Laser Annealed Amorphous Silicon Thin Films Grown by Low Pressure Chemical Vapor Deposition. Appl. Phys. Lett.*, **71**, 359 (1997).

[Lac85] Laczkó B.: *Kémiai gőzfázisú rétegleválasztás.* In Laczkó B., editor, *Alapvető eljárások*, Mikroelektronikai technológiai füzetek, Országos Műzsaki Információs Központ és Könyvtár, Budapest, 1985.

[Lau87] Lautenschlager P., Garriga M., Viña L., Cardona M.: *Temperature Dependence of the Dielectric Function and Interband Critical Points in Silicon. Phys. Rev. B*, **36**, 4821 (1987).

[Lee98] Lee J., Rovira P. I., An I., Collins R. W.: *Rotating-Compensator Multichannel Ellipsometry for Characterization of the Evolution of Nonuniformities in diamond thin-film growth. Appl. Phys. Lett.*, **72**, 900 (1998).

[Leh98a] Lehnert W., Berger R., Schneider C., Pfitzner L., Ryssel H., Stehle J. L., Piel J.-P., Neumann W.: *In situ Spectroscopic Ellipsometry for Advanced Process Control in Vertical Furnaces. Thin Solid Films*, **313-314**, 442 (1998).

[Leh98b] Lehnert W., Petrik P., Schneider C., Pfitzner L., Ryssel H.: *In situ Layer Characterization by Spectroscopic Ellipsometry at High Temperatures. ULSI Conference at NIST*, Accepted for publication (1998).

[Liu94] Liu Q., Wall J. F., Irene E. A.: *Interface Studies by Spectroscopic Immersion Ellipsometry and Atomic Force Microscopy. J. Vac. Sci. Technol. A*, **A12**, 2625 (1994).

[Liu95] Liu Q., Spanos L., Zhao C., Irene E. A.: *A Morphology Study of the Thermal Oxidation of Rough Silicon Surfaces. J. Vac. Sci. Technol. A*, **A13**, 1977 (1995).

[Log88] Logothetidis S., Polatoglou H. M., Ves S.: *Study of the Optical Transition in Poly- and Micro-Crystalline Si by Spectroscopic Ellipsometry. Solid State Commun.*, **68**, 1075 (1988).

[Log89] Logothetidis S.: *Surface-Roughness and Grain-Boundary Effects on the Optical Properties of Low-Pressure Chemical-Vapor-Deposited Silicon Thin Films by Spectroscopic Ellisometry. J. Appl. Phys.*, **65**, 2416 (1989).

[Loh82] Lohner T., Mezey G., Kótai E., Manuaba A., Pászti F., Dévényi A., Gyulai J.: *An Investigation of Ion-Bombarded Silicon by Ellipsometry and Channeling Effect. Nucl. Instr. and Meth.*, **199**, 405 (1982).

[Loh83] Lohner T., Mezey G., Kótai E., Pászti F., Manuaba A., Gyulai J.: *An Investigation of Ion-Bombarded Silicon by Ellipsometry and Channeling Effect. Nucl. Instr. and Meth.*, **209**, 615 (1983).

[Loh92] Lohner T., Skorupa W., Fried M., Vedam K., Nguyen N., Groetzschel R., Bartsch H., Gyulai J.: *Comparative study of the effect of annealing of nitrogen-implanted silicon-on-insulator structures by spectroscopic ellipsometry, cross-sectional transmission electron microscopy and rutherford backscattering spectroscopy. Mat. Sci. Eng.*, **B12**, 177 (1992).

[Loh93] Lohner T., Fried M., Gyulai J., Vedam K., Nguyen N. V., Hanekamp L. J., van Silfhout A.: *Ion-Implantation-Caused Special Damage Profiles Determined by Spectroscopic Ellipsometry in Crystalline and in Relaxed (annealed) Amorphous Silicon. Thin Solid Films*, **233**, 117 (1993).

[Loh94a] Lohner T.: *Félvezetők optikai és szerkezeti tulajdonságainak módosulása ionimplantáció és hőkezelés hatására: Az ellipszometria alkalmassá tétele ilyen jellegű vizsgálatokra.* PhD thesis, KFKI, 1994.

[Loh94b] Lohner T., Kótai E., Khánh N. Q., Tóth Z., Fried M., Vedam K., Nguyen N. V., Hanekamp L. J., van Silfhout A.: *Ion-implantation induced anomalous surface amorphization in silicon. Nucl. Instr. and Meth.*, **B85**, 335 (1994).

[Loh94c] Lohner T., Tóth Z., Fried M., Khánh N. Q., Yang G. Q., Lu L. C., Zou S., Hanekamp L. J., van Silfhout A., Gyulai J.: *Comparative Investigation of Damage Induced by Diatomic and Monoatomic Ion Implantation in Silicon. Nucl. Instr. and Meth.*, **B85**, 524 (1994).

[Loh98] Lohner T., Khánh N. Q., Zolnai Z.: *Spectroellipsometric Characterization of Ion Implanted Semiconductors and Porous Silicon. Acta Physica Slovaca*, **48(4)**, 441 (1998).

[Lor80] Lorenz L.. *Ann. Phys. Chem.*, **11**, 70 (1880).

[Lor16] Lorentz H. A.: *Theory of Electrons.* Teubner, Leipzig, 1916.

[McM86] McMarr P. J., Vedam K., Narayan J.: *Spectroscopic Ellipsometry: a New Tool for Nondestructive Depth Profiling and Characterization of Interfaces. J. Appl. Phys.*, **59**, 694 (1986).

[Mea87] Meakin D., Stoemenos J., Migliorato P., Economou N. A.: *Structural Studies of Low-Temperature Low-Pressure Chemical Deposited Polycrystalline Silicon. J. Appl. Phys*, **61**, 5031 (1987).

[Mez78] Mezey G., Kótai E., Lohner T., Nagy T., Gyulai J., Manuaba A.: *Improved Depth Resolution of Channeling Measurements in Rutherford Backscattering by a Detector Tilt. Nucl. Instr. and Meth.*, **149**, 235 (1978).

[MG04] Maxwell-Garnett J.. *Phil. Trans. R. Soc. Lond.*, **203**, 385 (1904).

[nan] *NanoScope Command Reference Manual.*

[Neu95] Neumann W., Gardawsky J.: *Spektroskopische Ellipsometrie; Grundlagen, Stand der Technik und Anwendungen.* In *Jahrbuch für Optik und Feinmechanik*, Fachverlag Schiele & Schön GmbH, Berlin, 1995.

[Pet98a] Petrik P., Biró L. P., Fried M., Lohner T., Berger R., Schneider C., Gyulai J., Ryssel H.: *Surface Roughness Measurement on Polysilicon Produced by Low Pressure Chemical Vapor Deposition Using Spectroscopic Ellipsometry and Atomic Force Microscopy. Thin Solid Films*, **315**, 186 (1998).

[Pet98b] Petrik P., Fried M., Lohner T., Berger R., Biró L. P., Schneider C., Gyulai J., Ryssel H.: *Comparative Study of Polysilicon-On-Oxide Using Spectroscopic Ellipsometry, Atomic Force Microscopy, and Transmission Electron Microscopy. Thin Solid Films*, **313-314**, 259 (1998).

[Pet98c] Petrik P., Polgár O., Lohner T., Fried M., Khánh N. Q., Gyulai J.: *Ion Implantation-Caused Damage Depth Profiles in Single-Crystalline Silicon Studied by Spectroscopic Ellipsometry and Rutherford Backscattering Spectrometry. Vacuum*, **50**, 293 (1998).

[Pet99a] Petrik P., Lehnert W., Schneider C., Fried M., Lohner T., Gyulai J., Ryssel H.: *In Situ Spectroscopic Ellipsometry for the Characterization of Polysilicon Formation Inside a Vertical Furnace. Submitted for publication in Thin Solid Films* (1999).

[Pet99b] Petrik P., Lohner T., Fried M., Khánh N. Q., Polgár O., Gyulai J.: *Comparative Study of Ion Implantation Caused Damage Depth Profiles in Polycrystalline and Single Crystalline Silicon Studied by Spectroscopic Ellipsometry and Rutherford Backscattering Spectrometry. Nucl. Inst. Meth.*, **B147**, 84 (1999).

[Pie93a] Piel J.-P.: *Determination of the Sign of Δ in Spectroscopic Ellipsometry without a Quarter-Wave Plate: Calculation and Applications. Thin Solid Films*, **234**, 447 (1993).

[Pie93b] Piel J.-P., Stehle J.-L., Thomas O.: *The Fastest Real Time Spectroscopic Ellipsometry: Applications and Limitations for In Situ and Quality Control. Thin Solid Films*, **233**, 301 (1993).

[Rie87] Riedling K.: *Ellipsometry for Industrial Applications.* Springer Verlag, Wien and New York, 1987.

[Sch86] Schuegraf K. K.: *Handbook of Thin-Film Deposition Processes and Techniques.* Noyes Publications, 1986.

[Sch93a] Schneider C.: *Entwicklung eines in situ-Meß- und Regelsystems für Halbleiterfertigungsprozesse am Beispiel der thermischen Oxidation von Silicium.* Verlag Shaker, 1993.

[Sch93b] Schneider C., Berger R., Pfitzner L., Ryssel H.: *In situ Ellipsometry for Real-Time Feedback Control of Oxidation Furnaces. Appl. Surf. Sci.*, **63**, 135 (1993).

[Shi97] Shirai H., Arai T., Nakamura T.: *Control of the Initial Stage of Nanocrystalline Growth Monitored by In Situ Spectroscopic Ellipsometry. Applied Surface Science*, **113**, 111 (1997).

[Siv95] Sivaram S.: *Chemical Vapor Deposition.* International Thompson Publishing Inc., 1995.

[Sny92] Snyder P. G., Xiong Y.-M., Woollam J. A.: *Characterization of Polycrystalline Silicon Thin-film Multilayers by Variable Angle Spectroscopic Ellipsometry. Surface and Interface Analysis*, **18**, 113 (1992).

[sop] *SOPRA ES4G Reference Manual.*

[Spa94] Spanos L., Liu Q., Irene E. A.: *Investigation of Roughened Silicon Surfaces Using Fractal Analysis. II. Chemical Etching, Rapid Thermal Chemical Vapor Deposition, and Thermal Oxidation. J. Vac. Sci. Technol. A*, **A12**, 2653 (1994).

[Suz94] Suzuki T., Adachi S.: *Chemical Treatment Effect of Si(111) Surfaces in NH_4F Solution Studied by Spectroscopic Ellipsometry. Jpn. J. Appl. Phys.*, **33**, 5600 (1994).

[Tac94] Tachibana K., Shirafuji T., Hayashi Y., Maekawa S.: *In Situ Ellipsometric Monitoring of the Growth of Polycrystalline Silicon Thin Films by RF Plasma Chemical Vapor Deposition. Jpn. J. Appl. Phys.*, **33**, 4191 (1994).

[Van89] Vanhellemont J., Maes H. E., de Veirman A.: *Spectroscopic Ellipsometry and Transmission Electron Microscopy Study of Annealed High-Dose Oxygen Implanted Silicon. J. Appl. Phys.*, **65**, 4454 (1989).

[Van91] Vanhellemont J., Roussel P., Maes H. E.: *Spectroscopic Ellipsometry for Depth Profiling of Ion Implanted Materials. Nucl. Instr. Meth.*, **55**, 183 (1991).

[Van92] Vanhellemont J., Roussel P.: *Characterization by Spectroscopic Ellipsometry of Buried Layer Structures in Silicon Formed by Ion Beam Synthesis. Mat. Sci. Eng.*, **B12**, 165 (1992).

[Ved85] Vedam K., McMarr P. J., Narayan J.: *Nondestructive Depth Profiling by Spectroscopic Ellipsometry. Appl. Phys. Lett.*, **47**, 339 (1985).

[Vuy93] Vuye G., Fisson S., Van V. N., Wang Y., Rivory J., Abelès F.: *Temperature Dependence of the Dielectric Function of Silicon Using in situ Spectroscopic Ellipsometry. Thin Solid Films*, **233**, 166 (1993).

[Xio90] Xiong Y. M., Snyder P. G., Woollam J. A., Krosche E. R., Strausser Y.: *Characterization of Polysilicon Thin Films by Variable Angle Spectroscopic Ellipsometry. Mater. Res. Soc. Symp. Proc.*, **182**, 219 (1990).

List of used acronyms

- a-Si – low pressure chemical vapor deposited amorphous silicon
- APCVD – atmospheric pressure chemical vapor deposition
- AFM – atomic force microscopy
- B-EMA – Bruggeman effective-medium approximation
- BS – backscattering spectrometry
- c-Si – single-crystalline silicon
- CVD – chemical vapor deposition
- EFM – electric force microscopy
- FFT – fast Fourier transformed
- i-a-Si – ion-implanted amorphous silicon
- LIS – linear image sensor
- LL – Lorentz-Lorenz approximation
- LPCVD – low pressure chemical vapor deposition
- LPLTO – low pressure low temperature oxidation
- LRA – linear regression analysis
- MG – Maxwell-Garnett approximation
- MOSS-OMA – Multilayer Optical Scanning Spectrometer – Optical Multi-channel Analyzer
- OPD – optical penetration depth
- pc-Si – fine-grained polycrystalline silicon
- PCSA ellipsometer – polarizer-compensator-sample-analyzer ellipsometer
- PDA – photo diode array
- PVD – physical vapor deposition

- RAE – rotating-analyzer ellipsometer
- RMS roughness – root mean square roughness
- RPE – rotating-polarizer ellipsometer
- RBS – Rutherford backscattering spectrometry
- SPM – scanning probe microscope
- STM – scanning tunneling microscope
- SE – spectroscopic ellipsometry

Summary

In the present work characterization of polysilicon thin films was performed using spectroscopic ellipsometry (SE).

In Chapter 2 the capability of multilayer optical models using the Bruggeman effective-medium approximation (B-EMA) for describing polysilicon layers deposited at different temperatures was investigated. Good agreement between SE and transmission electron microscopy (TEM) results were obtained. Using a four layer optical model, a transition layer between the buried oxide and the polysilicon layer was found. The conventionally used optical model was improved using the reference data of fine-grained polycrystalline silicon in the B-EMA method. The dependence of the optical model parameters on the layer thickness shows the different stages of the layer growth process. Comparison of the void fraction in the polysilicon layer measured by SE and Rutherford backscattering spectrometry (RBS) showed good agreement. The good fit results, the reasonably low confidence limits, and the good agreement with other measurement techniques proved the reliability of the optical models.

In Chapter 3 microscopic surface roughness of polysilicon layers deposited at different temperatures on oxidized single-crystalline silicon substrate was measured by SE and atomic force microscopy (AFM). The surface roughness measured by SE was compared with R_a and root mean square (RMS) roughness values measured by AFM using different window sizes. The results obtained by the two different technique show good correlation for both R_a and RMS roughness, but the slope of the correlation lines are different for different window sizes. It was shown that in spite of the good correlation, the interpretation of the ratio of the roughness measured by SE and AFM is not obvious, since both methods are influenced by many parameters, such as the correlation length, tip shape, or scan window size of AFM, and the used optical model or inhomogeneity in the case of SE. Results of other authors showed that there is little agreement in the interpretation of the roughness value measured by SE. In spite of all these facts, the results of the present work show that, taking into account the mentioned restrictions, SE calibrated against AFM data can be used for quantitative surface roughness determination.

In Chapter 4 ion-implantation-caused damage depth profiles in single- and polycrystalline silicon were studied by SE and RBS. The high depth resolution RBS technique was used as a cross-checking method. The depth of the damaged region was also measured by TEM. The agreement of the measurement results made by the two different techniques was good, although the RBS method could not be applied for implanted polycrystalline silicon, because the grains of the chemically vapor deposited (CVD) polysilicon samples were not quasi-oriented. In this case the SE results were verified by TEM. The damage depth measured by SE and TEM show a good agree-

ment.

In Chapter 5 the process of integrating a spectroscopic ellipsometer into a vertical furnace is presented. At the Fraunhofer Institut für Integrierte Schaltungen in Erlangen, Germany, a method was developed, by the use of which an optical access to the samples under process can be achieved with minimal modification of the chamber itself. The method takes advantage of using prisms in total reflection mode. Therefore, the phase shift caused by them have to be corrected. A part of this work was the realization of a method of calibration for the phase shift caused by the prisms. The system was used to determine the high temperature dielectric function of single-crystalline silicon up to 700°C. At lower temperatures, where literature data were present, a good agreement was found between them and our results. The high temperature dielectric function data were used as references for the evaluation of measurements during crystallization of amorphous silicon.

In the present work I have obtained the following new results, which was my own contribution to the above mentioned works:

1. I have developed new optical models for the interpretation of ellipsometric measurements of polysilicon layers deposited on oxidized single-crystalline silicon. Using these optical models the physical properties of the layers and their dependence on the deposition conditions can be determined with a high precision. The native surface oxide layer was taken into consideration. Using a top oxide layer of 3.2 nm σ (i. e. the fit quality) decreased by 0.0001, which is negligible. Therefore, I neglected the the top native oxide layer in the optical models. I have performed a systematic study to determine the dependence of the fitted parameters of the optical models (such as layer thickness, surface roughness, or density) on the parameters of the sample preparation (deposition temperature, layer thickness). The results give information on the different phases of layer growth, or the change of the grain structure or surface roughness. I have cross-checked the density determined by SE with the density measured by RBS obtaining a good correlation of the two techniques. I have proved the reliability and precision of the ellipsometric measurements by using results of independent methods like TEM (layer thickness), AFM (surface roughness), or RBS (density) measured by my colleagues. [Pet98b]

2. I have used the optical models that I have developed for polysilicon structures for the quantitative determination of polysilicon surface roughness. I have determined the RMS and R_a surface roughnesses together with other informations on the surface (such as Fast Fourier Transformation spectra or cross-sectional surface profiles) by two independent methods: SE and AFM. I compared the surface roughness determined by SE and AFM (measured by my colleague) finding a good correlation. I showed that the correlation depends on numerous parameters like the sample preparation conditions. I showed that SE, calibrated by AFM, can be used for quantitative surface roughness determination [Pet98a].

3. I have created optical models for SE measurements of ion-implantation-caused damage depth profiles in single- and polycrystalline silicon. I have shown that the damage created by ion-implantation in polycrystalline silicon can be determined with a high confidence also in cases, where – as a result of the lack of

quasi-orientation of the grains – the RBS method cannot be applied. I have compared the ion-implantation induced damage depth profiles in single- and polycrystalline silicon under identical implantation conditions. I found that for the higher doses the damaged region of ion-implanted polycrystalline silicon extends from the surface in contrast to the single-crystalline silicon having a buried damaged layer. Precision and reliability of the ellipsometric measurements were justified by TEM (single- and polycrystalline samples) and RBS (single-crystalline samples) measured by my colleagues . Based on these results I showed that SE is a fast, non-destructive, and precise method for measuring ion-implantation caused disorder even in polycrystalline silicon, if a proper optical model is used [Pet98c, Pet99b].

4. I demonstrated the application of SE for *in situ* measurement in a vertical furnace taking the measurement of the high temperature dielectric function of the single-crystalline silicon and the crystallization of the amorphous silicon as an example. I realized a method for the correction of the phase shift caused by the beam-guiding prisms. I cross-checked the precision and accuracy of the *in situ* ellipsometer using a reference ellipsometer. I determined the high-temperature dielectric function of single-crystalline silicon up to a temperature of 700°C. At lower temperatures, where literature data were present, I found a good agreement between them and my results. Using the high-temperature dielectric function of single-crystalline silicon determined in the vertical furnace I realized *in situ* measurements of the crystallization of amorphous silicon [Pet99a, Ber94, Leh98b].

List of relevant publications

1. Petrik P., Biró L. P., Fried M., Lohner T., Berger R., Schneider C., Gyulai J., and Ryssel H.: *Surface Roughness Measurement on Polysilicon Produced by Low Pressure Chemical Vapor Deposition Using Spectroscopic Ellipsometry and Atomic Force Microscopy*, Thin Solid Films **315**, 186 (1998).
2. Petrik P., Fried M., Lohner T., Berger R., Biró L. P., Schneider C., Gyulai J., Ryssel H.: *Comparative Study of Polysilicon-On-Oxide Using Spectroscopic Ellipsometry, Atomic Force Microscopy, and Transmission Electron Microscopy*, Thin Solid Films **313-314**, 259 (1998).
3. Petrik P., Polgár O., Lohner T., Fried M., Khánh N. Q., Gyulai J.: *Ion implantation-caused damage depth profiles in single-crystalline silicon studied by Spectroscopic Ellipsometry and Rutherford Backscattering Spectrometry*, Vacuum **50**, 293 (1998).
4. Petrik P., Lohner T., Fried M., Khánh N. Q., Polgár O., Gyulai J.: *Comparative Study of Ion Implantation Caused Damage Depth Profiles in Polycrystalline and Single Crystalline Silicon Studied by Spectroscopic Ellipsometry and Rutherford Backscattering Spectrometry*, Nucl. Instr. Meth. **B147**, 84 (1998).
5. Lehnert W., Petrik P., Schneider C., Pfitzner L., Ryssel H.: *In situ Layer Characterization by Spectroscopic Ellipsometry at High Temperatures*, ULSI Conference in Gaithersburg NIST, American Institute of Physics, Conference Proceedings **449**, 326 (1998).
6. Berger R., Petrik P., Schneider C., Neumann W., Stehlé J.-L.: *In situ Monitoring of Layer Growth in Conventional Vertical Furnaces by Spectroscopic Ellipsometry*, Workshop International on Spectroscopic Ellipsometry, Erlangen, 1994.
7. Petrik P., Lohner T., Fried M., Biró L. P., Khánh N. Q., Gyulai J., Lehnert W., Schneider C., Ryssel H.: *Ellipsometric Study of Polycrystalline Silicon Films Prepared by Low Pressure Chemical Vapor Deposition*, J. Appl. Phys. **87(4)**, 1734 (2000).
8. Petrik P., Lehnert W., Schneider C., Fried M., Lohner T., Gyulai J., Ryssel H.: *In Situ Spectroscopic Ellipsometry for the Characterization of Polysilicon Formation Inside a Vertical Furnace*, accepted for oral presentation to E-MRS'99 conference, Thin Solid Films **359**, (2000).